2014

Specialty Fiber Lasers and Novel Fiber Devices

Clemence Jollivet
University of Central Florida

SPECIALTY FIBER LASERS AND NOVEL FIBER DEVICES

by

CLÉMENCE JOLLIVET
Diplôme de Licence, Université Bordeaux 1, France, 2007
Diplôme de Master, Université Bordeaux 1, France, 2009
M.S., University of Central Florida, USA, 2012

A dissertation submitted in partial fulfillment of the requirements
for the degree of Doctor of Philosophy
in the College of Optics and Photonics
at the University of Central Florida
Orlando, Florida

Summer Term
2014

Research advisor:
Axel Schülzgen

ABSTRACT

At the Dawn of the 21st century, the field of specialty optical fibers experienced a scientific revolution with the introduction of the stack-and-draw technique, a multi-steps and advanced fiber fabrication method, which enabled the creation of well-controlled micro-structured designs. Since then, an extremely wide variety of finely tuned fiber structures have been demonstrated including novel materials and novel designs.

As the complexity of the fiber design increased, highly-controlled fabrication processes became critical. To determine the ability of a novel fiber design to deliver light with properties tailored according to a specific application, several mode analysis techniques were reported, addressing the recurring needs for in-depth fiber characterization.

The first part of this dissertation details a novel experiment that was demonstrated to achieve modal decomposition with extended capabilities, reaching beyond the limits set by the existing mode analysis techniques. As a result, individual transverse modes carrying between ~0.01% and ~30% of the total light were resolved with unmatched accuracy. Furthermore, this approach was employed to decompose the light guided in Large-Mode Area (LMA) fiber, Photonic Crystal Fiber (PCF) and Leakage Channel Fiber (LCF). The single-mode performances were evaluated and compared. As a result, the suitability of each specialty fiber design to be implemented for power-scaling applications of fiber laser systems was experimentally determined.

The second part of this dissertation is dedicated to novel specialty fiber laser systems. First, challenges related to the monolithic integration of novel and complex specialty fiber designs in all-fiber systems were addressed. The poor design and size compatibility between specialty fibers and conventional fiber-based components limits their monolithic integration due to high coupling loss and unstable performances. Here, novel all-fiber Mode-Field Adapter (MFA) devices made

of selected segments of Graded Index Multimode Fiber (GIMF) were implemented to mitigate the coupling losses between a LMA PCF and a conventional Single-Mode Fiber (SMF), presenting an initial 18-fold mode-field area mismatch. It was experimentally demonstrated that the overall transmission in the mode-matched fiber chain was increased by more than 11 dB (the MFA was a 250 μm piece of 50 μm core diameter GIMF). This approach was further employed to assemble monolithic fiber laser cavities combining an active LMA PCF and fiber Bragg gratings (FBG) in conventional SMF. It was demonstrated that intra-cavity mode-matching results in an efficient (60%) and narrow-linewidth (200 pm) laser emission at the FBG wavelength.

In the last section of this dissertation, monolithic Multi-Core Fiber (MCF) laser cavities were reported for the first time. Compared to existing MCF lasers, renown for high-brightness beam delivery after selection of the in-phase supermode, the present new generation of 7-coupled-cores Yb-doped fiber laser uses the gain from several supermodes simultaneously. In order to uncover mode competition mechanisms during amplification and the complex dynamics of multi-supermode lasing, novel diagnostic approaches were demonstrated. After characterizing the laser behavior, the first observations of self-mode-locking in linear MCF laser cavities were discovered.

To my family

ACKNOWLEDGMENTS

Graduating with a Ph.D. degree is a professional achievement, opening promising opportunities towards a successful scientific career. But it is also a personal achievement, the product of several years of entire dedication, extreme rigor and sometimes sacrifices, where curiosity and excitement are shared with disappointment and frustration on a daily basis. Accomplishing this degree is the result of scientific collaborations, fruitful discussions, research partnerships and friendships between researchers sharing the same interest in science. In this section, I would like to acknowledge the many people who contributed, in one way or the other, to my research and to this dissertation.

Starting with my Ph.D. advisor, Dr. Axel Schülzgen, to whom I would like to express all my gratitude and appreciation. Axel has played a major role during the completion of my degree, not only by being extremely available, by offering his expert guidance and always “on-the-spot” advices, but also by being very supportive and trustful of my initiatives, feeding my scientific interest, sometimes addressing my doubts and encouraging my patience. I particularly enjoyed sharing the same scientific enthusiasm with my advisor, trying to understand novel physical concepts and exploring new horizons using specialty fibers.

Then, I would like to sincerely acknowledge my committee member, Dr. Martin Richardson, first of all, for being the first CREOL faculty who has welcomed me in his research group and for actively participating in motivating my scientific interest in fiber systems and laser sources. Over the years, Martin has offered me his help and support at strategic times of my education, playing a major role in the decision to pursue my Ph.D. His vision has always inspired me.

My sincere thank you goes to Dr. Jim Moharam, my second committee member, who has introduced me to the fundamentals of light propagation in optical waveguides and to the concept of optical fibers and transverse modes. I believe that some of my interest in specialty fibers, which are the center pieces of my Ph.D. research, was born in the particularly well designed classes Jim gave during my first year in CREOL.

I would also like to recognize the special contribution of Dr. Arash Mafi, my external committee member, for his time dedication and for the helpful discussions related to the Multi-Core Fiber (MCF) project. His expertise and his theoretical knowledge of coupled-core theory have greatly contributed to uncover some of the principles governing light propagation in these complex structures.

I would like to thank my colleagues, present and past members of the Fiber Optics Lab (FOL). Particularly Amy Van Newkirk for the time we shared together, trying to understand and solve numerous fiber-related challenges, organizing a convenient and well-to-be-in lab space and also for the she time spent proof-read all my papers, including this dissertation, using her native English skills. Many thanks to Khawlah Al Yahyaei, Aniket Patil, Burdley Colas and Dr. Peter Hofmann.

A significant part of the mode analysis work presented in this dissertation and published in scientific journals was the result of a fruitful scientific collaboration with Dr. Daniel Flamm and his Ph.D. advisor, Dr. Michael Duparré, from the Institute of Optics in the Friedrich Schiller University (Jena, Germany). I would like to sincerely acknowledge these two experts of the correlation filter method. Besides being an extremely knowledgeable scientist, Daniel has also been a very good friend. After all, what would be a better way than sealing a friendship around endless mode-analysis discussions and time spent on the complex combined experiment?

Along the way, I had the opportunity to work with 2 μm fiber laser sources and to gain knowledge in the development and the applications of these sources. For that I would like to express my gratitude to Dr. Lawrence Shah, Dr. Pankaj Kadwani and Dr. Andrew Sims from the Laser and Plasma Laboratory in CREOL.

Also, I would like to thank Dr. Bryce Samson from Nufern Inc. for collaborating, with FOL, sharing interest in our research and giving us samples of the Leakage Channel Fiber. The interesting results from the modal decomposition I performed on this prototype fiber have led to contributed journal papers and conference presentations.

The credit for designing and fabricating the MCF used in this dissertation has to go to Dr. Kay Schuster and Stephan Grimm from the Institute of Photonic Technologies (Jena, Germany), who I would like to deeply acknowledge for offering our research group several samples of different MCF designs.

Many thanks to Dr. Lasse Leick from NKT photonics A/S, who offered passive and active samples of Large-Mode Area (LMA) Photonic Crystal Fiber (PCF) to FOL, sharing our interest on measuring the guided mode content in these specialty fibers.

I also would like to acknowledge Dr. Marc SeGall, Dr. Ivan Divliansky and Dr. Leonid Glebov, pioneers in the development of holographic phase masks in photo-thermo refractive glass who suggested to implement this approach in optical fibers. The successful results have opened the route towards future promising research topics.

During the early days of the drawing tower in CREOL, Dr. Rodrigo Amezcua Correa introduced me to the stack-and-draw fabrication technique for micro-structured fibers. I would like to especially thank Rodrigo for sharing some of his expertise with me.

During the past few years, the contribution of several exchange scientists and students with our research group should also be recognized. It was a great pleasure to share some lab work with Dr. Seung Kwan Kim, Dr. Hageo desirena, Tobias Tieß, and Heidar Bendaci. Special thanks to Charles Loussert and Julie Guer for joining me full-time on some of my experiments and obtaining excellent results recently published.

I would like to acknowledge members of the CREOL administration and staff: Richard Zotti, Rachel Franzetta, Amy Perry, Denise Whiteside, Deon Frank, Matthew Petrone for their constant help and support and for contributing to make the time spent in CREOL enjoyable.

All my gratitude goes to our Dean, Dr. Bahaa Saleh, who has not only been a faithful supporter of my recent initiative to create an organization for Women in Lasers and Optics (WiLO) in CREOL, but who is also suggesting excellent ideas to further develop WiLO.

On a more personal note, I would like to thank my friends and colleagues that I didn't mention yet and who were part of my past and present CREOL experience: Nathan, Rob, Soroush, Mark, Christina, Dan, Brian, Julien, Clarisse and all the other…

A few very special words have to go to Dr. Laurent Sarger, who has been the first one to offer me a few-months internship in CREOL in 2008, when I was pursuing my M.S. degree in Bordeaux. Without his support and his trust, I would have never become a member of the CREOL family. Merci Laurent pour cette opportunité en or!

In parallel of my complete dedication and involvement in my Ph.D. degree, I have been entirely emotionally bounded to my Flamenco dance partners and friends, in particular to Denise, Tammy and Ivan. Sharing this exceptional art form with them has been essential to balance my life during the past years. OLÉ!

But the main form of life balance during these years has been my outstanding family: my mum Evelyne, my dad Bernard, my brother Ted, my dear Gillou, all my grandparents, my amazing boyfriend Andi, my closest friend Bérénice and her family and my very special god-mother Martine and Daniel. Some of them being so far in space but all of them being so close to me, always supporting me, following my progress, listening to my complains and sharing my success. I love you!

TABLE OF CONTENTS

LIST OF FIGURES

LIST OF TABLES

LIST OF ACRONYMS/ABBREVIATIONS

BS	beam splitter
CCC	chirally-coupled core
CFM:	correlation filter method
CGH:	computer generated hologram
DGD:	differential group delay
DF:	delivery fiber
FM:	fundamental mode
FUT:	fiber under test
GIMF:	graded-index multi-mode fiber
HCF:	hollow-core fiber
HOM:	higher-order mode
HPM:	holographic phase mask
LCF:	leakage channel fiber
LMA:	large-mode area
MCF:	multi-core fiber
MFA:	mode-field adapter
MFD:	mode-field diameter
MMF:	multi-mode fiber
MMI:	multi-mode interference
MMLD:	multi-mode laser diode
MP:	mode power
MPI:	multi-path interference
NF:	near-field
OD:	output diameter
OSA:	optical spectrum analyzer
PCF:	photonic crystal fiber
PF:	probe fiber
PTR:	photo-thermo refractive
QSM:	quasi-single-mode
RMC:	resonant mode coupling
RP:	radially polarized
SIF:	step-index fiber
SIMF:	step-index multi-mode fiber
SLM:	spatial light modulator
SM:	supermode
SMF:	single-mode fiber
SML:	self-mode locking
SNR:	signal-to-noise ratio
SRL:	self-reproduction length
SRW:	self-reproduction wavelength
TIR:	total-internal reflection

CHAPTER 1: INTRODUCTION

At the dawn of the 21st century, new-technologies are one of the prime factors participating in the evolution of our society. Indeed, the daily development of novel-technologies directly contributes to increase the speed of communications, the accessibility to transportation, and the development of novel types of entertainment. On the other hand, they also contribute to facilitate the life of individuals as an ever-increasing number of smaller, faster, more efficient, convenient and easy-to-use devices are released, providing the user with higher connectivity and enabling to increase the volume of tasks achieved each day. A close look at the "top-10" charts of technological innovations published in the past years (e.g. CNN ranking of the best innovations in 2013 [1]) shows that more than 80% of the top-inventions involved Optics, Photonics and/or Laser technologies. Nowadays, Optic and Laser technologies are the center piece of an extremely wide range of applications and represent a multi-billion dollars market industry. Applications include information technology for optical storage devices (CD and DVD players), telecommunications and internet, medicine (for micro-surgeries, non-invasive ablations, eye surgeries, tattoo removal, etc.), manufacturing for high precision cutting and welding, measurement and analysis (military long range detection, chemical analysis, etc.), stress and temperature sensors, research applications in the field of Nuclear physics and Astrophysics and much more. The major role played by Optics and Laser technologies in the development of our current society is the result of decades of fundamental and experimental research studies. In this context, one of the most recent technological breakthrough has occurred a few decades ago with the discovery of fast

telecommunications and internet. The enabling technology was a micro-sized rod made from Fused Silica glass which was demonstrated to transport optical signals along kilometer lengths with extremely low attenuation. This technology, called optical fibers, is the center piece of the work detailed in this dissertation.

1.1 Historical milestones in the development of optical fibers

In this paragraph, the context of the present study is presented in a chronological approach retracing the important historical milestones which have contributed to the development of high-performances optical fibers. These events are illustrated on a time arrow presented in Figure 1-1. Events, from the Antiquity (~ 3500 BC) until nowadays, which contributed to the evolution of the field of specialty fibers, were sorted in three categories: laser development (blue), telecommunication burst (orange) and fiber fabrication techniques and designs (green).

The foundation of optical fibers relies on knowledge in optical science including glass fabrication and purification. The glass work started centuries ago during the Antiquity where glass material was mainly used for arts and crafts, before transitioning to industrial production in the 1900's. The real "revolution" occurred during the 1960's when Schawlow, Townes and Maiman invented the laser [2], [3]. While the impact of the laser discovery on the society had been recognized a few years later with a Nobel prize, Kao and Hockham, who predicted that Fused Silica optical fibers could transmit optical frequencies with low-attenuation, out-performing the copper wires used back then [4] where acknowledged about thirty years later in 1999. The critical attenuation value of 20 dB/km has been achieved a few years later in 1970 by researchers from Corning [5].

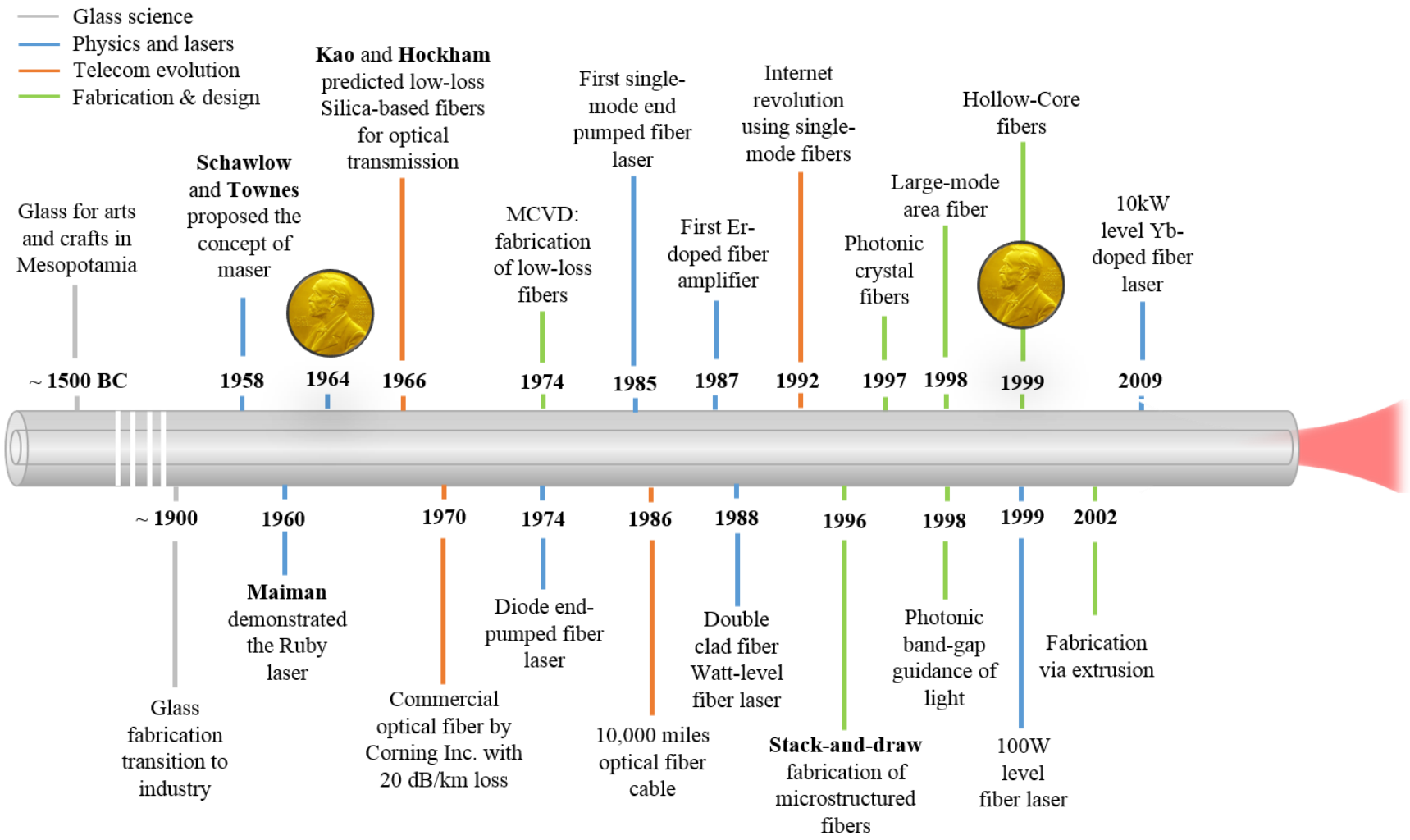

Figure 1-1: Historical evolution of selected optical fiber discoveries including fabrication, laser and telecom applications.

While the first fiber lasers using diode pumping and later end pumping schemes were demonstrated between 1970 and 1980, telecommunication companies successfully implemented optical fibers to transmit phone conversations along a 6 miles cable first, followed by a full 10,000 miles network across USA. Further improving the fabrication process, such as the modified chemical vapor deposition (MCVD) demonstrated the first time in 1974 by MacChesnay *et al.* [6], and the purity of the Fused Silica glass considerably improved the performances of optical fibers, able to achieve low-attenuation, high bandwidths, good dimension control and strong mechanical properties. New applications emerged including the first Erbium doped fiber laser in 1987 [7] followed by the demonstration of the first double-clad fiber laser by Snitzer *et al.* in 1988 [8]. Low-attenuation and single-mode properties of Fused Silica enabled to achieve transmission of Tera-bite amounts of information in 1992, leading to what is called nowadays the internet.

One of the most important milestone in the development of specialty fibers occurred at the beginning of the 21st century with the invention of a novel fabrication technique called "stack-and-draw". This multi-step, high-precision process allowed to control the fabrication of micro-elements on the order of (or smaller than) the optical wavelength inside the optical fiber [9]. This fabrication technique has been widely employed since then, opening the route towards the development of novel fiber designs e.g. single-mode Photonic Crystal Fiber (PCF) [10], Photonic Band-Gap (PBG) fibers [11] and Hollow Core Fibers (HCF) [12] and more. Meanwhile, another fabrication technique using the concept of extrusion (forcing a soft glass medium through a well-engineered casted proeform) was demonstrated around the year 2002 to fabricate soft micro-structured glass [13] preferred for supercontinuum generation and nonlinear effects-based applications. Finally, within the past couple of years, fiber lasers have benefitted from the improvements in glass purity,

fabrication techniques and high-precision micro-structured fiber designs, able to deliver scaled output performances as multi-kW output power levels were reported in 2009 [14].

1.2 Specialty optical fibers

So-called conventional fibers are made of a core and a cladding layer arranged in a step-index profile. They generally use high purity Fused Silica glass which is transparent for the optical wavelengths comprised between ~0.2 μm to ~2.2 μm. In particular, light wavelengths propagating at $\lambda \approx 1.33$ μm experience no second order dispersion in Fused Silica which is one of the main reason for using Fused Silica single-mode optical fibers in telecommunication applications. An image of the facet of a conventional step-index fiber is shown in Figure 1-2(a).

So-called specialty fibers can be defined as cylindrical waveguides made of different material and different design compared to the conventional fibers.

Specialty fibers using novel glass material such as Tellurite or Chalcogenide glass have been investigated for their extended transparency window (up to 10 μm wavelength) and high non-linear optical coefficient [15] suitable for supercontinuum generation. Phosphate glass fibers have been studied in the literature for their ability to sustain high doping concentrations making it a good candidate for single-frequency fiber lasers [16]. More recently, a novel type of fibers made from Photo-Thermo Refractive (PTR) glass, renowned for its high photosensitivity properties, were successfully fabricated [17]. Expected applications include all-fiber integration of optical systems.

On the other hand, independently from the choice of the constituent material, a multitude of specialty fiber designs have been reported and it would be difficult to provide an extensive list

including all the cases (in particular since this field of research remains in constant evolution). Instead, microscope images of a few specialty fiber designs are represented in Figure 1-2(b) along with a brief description of their performances and (or) applications.

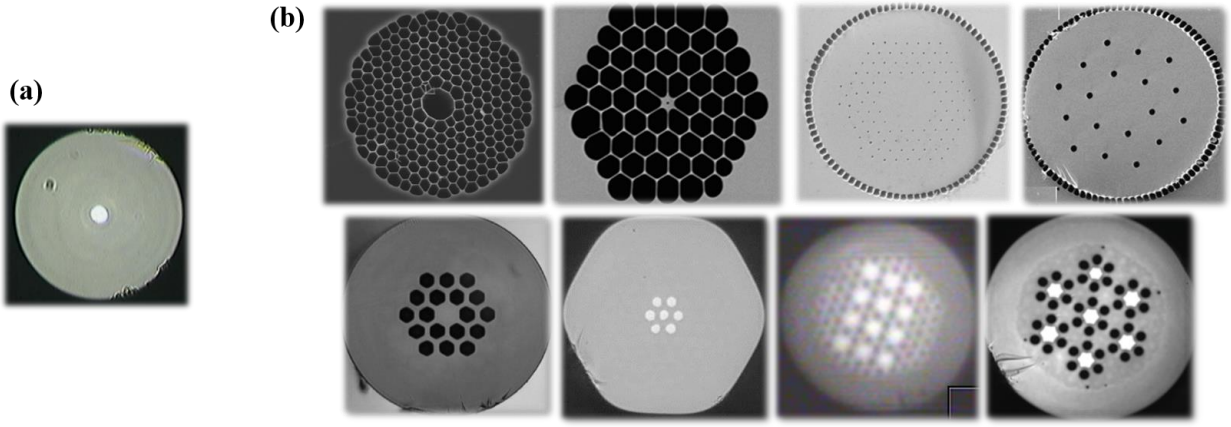

Figure 1-2: Images of different fiber designs showing (a) a step-index profile and (b) examples of specialty fiber designs with (from left to right, top to bottom): a Hollow Core Fiber (HCF) [13], a small core Photonic Crystal Fiber (PCF) [14], a Large-Mode Area (LMA) PCF [15], a Large Pitch Fiber (LPF) [16], a Leakage Channel Fiber (LCF) [17], a 7-coupled-core fiber [18], a 12-cores array fiber [19] and a hole-assisted Multi-Core Fiber (MCF) [20].

From left to right, the first image shows a Hollow-Core Fiber (HCF) where light is guided via photonic band-gap effect [18], followed by a small core Photonic Crystal Fiber (PCF) (name arise from the periodicity of the cladding material), well suited for supercontinuum light generation [19]. The following fiber is a different type of PCF made with a Large-Mode Area (LMA) core [20] designed to scale the output power of fiber lasers. So is the Large-Pitch Fiber design [21] as well as the Leakage Channel Fiber (LCF) design [22]. Finally, Multi-Core Fiber (MCF) designs are shown starting with a 7-cores fiber [23] and a 12-cores fiber [24] designed for high-brightness laser applications. The last image shows a hole-assisted MCF [25] ensuring low-cross talk during light propagation and demonstrated for telecom applications.

1.3 Towards the development of novel fiber designs

The increasing demand for novel specialty fiber can be related to the wish to integrate free-space-based optical and laser devices in compact and cost-effective all-integrated systems delivering light with high performances. This section introduces the general steps of creating, designing and fabricating novel specialty fibers. The steps are illustrated with the concrete example of a specialty fiber designed and fabricated in CREOL to deliver a single-radially polarized (RP) mode.

1.3.1 Fiber conception

The process to create novel specialty fibers is initiated once potential applications are identified. Target applications must significantly benefit from the use of novel fiber designs, either to stabilize, amplify or improve the current performances. In this chapter, the example of RP beams, renowned for their unique focusing power particularly suitable in optical tweezers applications [26], [27], is used to illustrate each step. Since the material and design of a specialty fiber are tailored to influence the properties of the guided light, one can hope to achieve single-mode RP beam delivery using a well-designed and fabricated specialty fiber.

Once the requirements of the target application are identified, a compatible fiber concept in terms of size, material and structure is determined. In the case of RP beams, the specialty fiber must (a) be single-mode at the wavelength of operation and (b) deliver a ring-shaped beam with radial polarization orientation.

1.3.2 Fiber design

In standard optical fibers, the first higher-order mode (LP_{11}) is a linear superposition of three degenerated modes, labeled TE_{01}, TM_{01} and HE_{21} (2 orthogonal polarizations), and called azimuthally polarized mode, radially polarized mode and hybrid mode respectively. These modes are the solutions of the wave equation solved outside the paraxial approximation (see Chapter 2 for more details). Thus, to achieve single RP mode delivery, the degeneracy between TE_{01}, TM_{01} and HE_{21} must be lifted by the fiber design. To do so, the index contrast between the core and cladding regions must be large (>10^{-2}). In practice, this can be achieved in a photonic crystal cladding structure with a high air-filling ratio. Then, in order to force the TM_{01} mode to be the first and only guided mode, the core symmetry of the specialty fiber must be "broken" into a ring geometry in order to optimize the core overlap with the RP mode. The corresponding specialty fiber designed for single-mode, RP beam delivery is a ring-shaped core embedded in a photonic crystal cladding with high air-filling ratio. This specialty fiber has been named ring-PCF and is schematically presented in Figure 1-3(a).

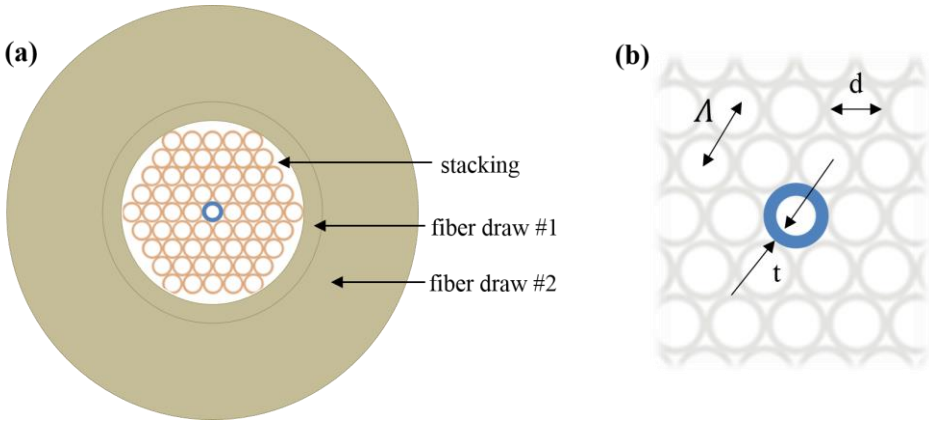

Figure 1-3: (a) Schematic of the specialty fiber designed for single-mode RP beam delivery. The steps used in the fiber fabrication process are indicted with arrows and further detailed in Section 1.3.3. (b) Definition of the parameter in the ring-PCF design used in the numerical model.

In order to determine the appropriate dimensions of the ring-PCF, the structure is simulated in a numerical mode solver using vectorial finite element method. The guided mode content is calculated while varying the parameters of the ring-PCF indicated in Figure 1-3(b) with Λ, the pitch of the photonic crystal cladding, the cladding ring inner diameter labeled d and the thickness of the ring-shaped core t. In order to anticipate its future integration with existing fiber devices, index values of Fused Silica glass were used in the numerical model and the modes guided in the center core were solved at λ = 1.55 μm. A range of fiber dimensions ensuring single radially polarized light emission was found from the mode-solver results and values are summarized in Table 1.

Table 1: Calculated dimensions of the ring-PCF to deliver single RP mode

Parameter	**Value**
Cladding pitch Λ	10 μm
d/Λ	0.8
Core thickness *t*	2.3 μm

The simulation results corresponding to the ring-PCF with the dimensions listed in Table 1 are presented in Figure 1-4(a) and (b) showing the intensity profile and the corresponding vector plot respectively of the lowest order guided mode. These results are compared with the theoretical intensity profile of the TM_{01} mode.

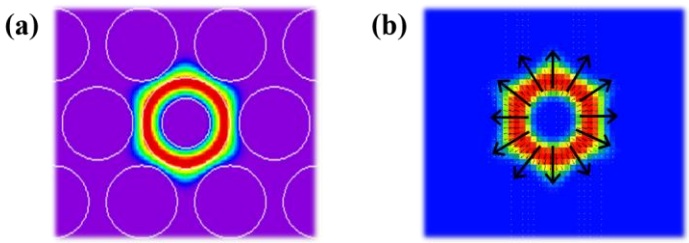

Figure 1-4: (a) Calculated intensity profile of the lowest order mode guided in the ring-PCF core and (b) corresponding vector plot showing the radial orientation of the polarization.

1.3.3 Fiber fabrication

Three main techniques are currently used to fabricate optical fibers. The common method for step-index and graded index fibers is called Modified Chemical Vapor Deposition (MCVD) [28]. This method allows a high control of the chemical constituents of a glass material and thus of the refractive indices and doping levels of each glass layer. However, it is restricted to fabricate all-solid, circularly symmetric fiber designs. Soft glass specialty fibers designed with sub-wavelength features, are generally fabricated using extrusion techniques through carefully-engineered preforms [29]. In order to fabricate highly-controlled micro-structured Fused Silica glass specialty fibers, the most widely used technique is called stack-and-draw [30].

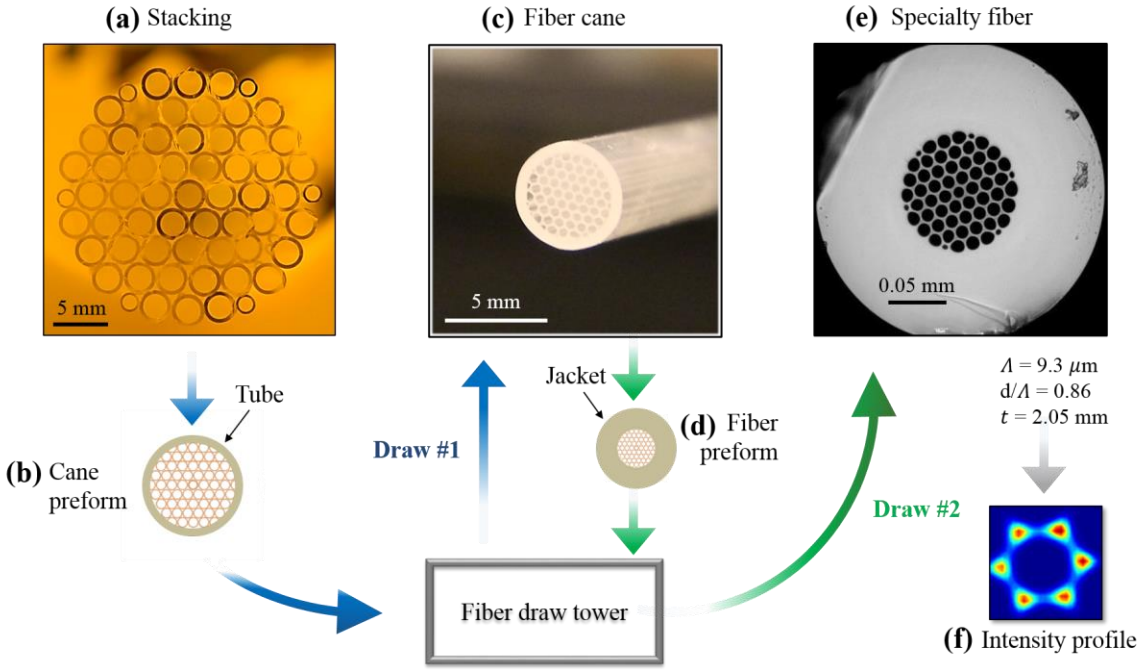

Figure 1-5: Stack-and-draw fabrication technique illustrated with the example of the ring-PCF. After stacking the ring-PCF (a), it is inserted in a glass tube to form the cane preform (b). Using a fiber drawing tower, the fiber can is obtained (c). A thick jacket tube is then used to form the fiber cladding and the second preform is drawn down to the final specialty fiber while finely tuning the drawing parameters (e). Measured fiber dimensions are indicated. Light at 1.55 μm wavelength delivered by the ring-PCF after propagating several meters is measured with a CCD in (f).

The steps of the stack-and-draw process are illustrated in Figure 1-5 using the example of the ring-PCF. The procedure is initiated by assembling a macroscopic iteration of the fiber design respecting the size ratio between each structural element as previously determined with the numerical calculations (Figure 1-5(a)). This stack is assembled in a clean room environment and, as illustrated in Figure 1-5 (b), is inserted in a Fused Silica tube (generally 1 inch in diameter) to form the cane preform. This first preform is mounted on a fiber drawing tower which is a complex piece of equipment allowing to control the furnace temperature, the speed of the preform feed in the furnace, the speed of the fiber pulling and the gas pressure. The fiber parameters are adjusted according to the values in Table 1 during the fiber drawing and requires several operators. The result is called a fiber cane (Figure 1-5 (c)) with an outer diameter varying between 0.5 mm and 1 mm. The cane is fitted into a thicker jacket tube that will be later forming the fiber cladding layer (Figure 1-5 (d)). The cane and jacket are then drawn down into the final fiber product. During this step, the drawing parameters must be highly controlled to accurately reproduce the targeted fiber parameters. A microscope image of the final ring-PCF is shown in Figure 1-5(e). The fiber dimensions, extracted after imaging the fiber facet with a microscope, are indicated showing a agreement with the target values from Table 1. The ring-PCF outer diameter was 230 μm. The light at λ = 1.55 μm delivered by the ring-PCF after propagating several meters was recorded with a CCD and is shown in Figure 1-5(f). Even though the measured intensity exhibits a ring-shaped profile, profile distortions were measured. This might be explained by the fact that the ring-PCF core was not sing-mode. In order to refine the specialty fiber design, an in-depth characterization must be performed on the ring-PCF. In most cases, several iterations of numerical designs and fiber draw are required before obtaining a final specialty fiber devices matching the targeted specifications.

1.4 Dissertation outline

In this dissertation, the focus was set towards the development and the characterization of novel specialty fibers made from Fused Silica glass and their monolithic integration.

The theoretical basis are set in Chapter 2 where the fundamental principles of light propagation in optical fibers are briefly introduced, including the phenomenon of Multi-Mode Interference (MMI) and the effect of fiber perturbations on the guided light.

The body of this dissertation is divided into two main sections. The first topic covered in Chapter 3 and Chapter 4 is centered on the performances of mode analysis techniques which are powerful characterization tools for novel specialty fibers. In Chapter 3, after presenting a state-of-the-art review of the existing mode analysis techniques, a first-of-a-kind experiment combining S^2 imaging and the correlation filter method, is introduced. Results including extended capabilities beyond the actual limits of modal decomposition are detailed.

These findings are then used in Chapter 4 to demonstrate the first in-depth characterization of several prototypes specialty fibers. Measured performances include low-loss, broadband single-mode operation in a specialty LCF followed by a comparison of the single-mode performances between different LMA specialty fibers in the 2 μm wavelength range.

The second part of this dissertation, detailed in Chapter 5 and Chapter 6, has been dedicated to assembling and characterizing novel monolithic fiber lasers employing specialty fibers. A novel approach to integrate "oversized" LMA gain specialty fibers in monolithic fiber laser cavities is presented in Chapter 5 using all-fiber Mode-Field Adapter (MFA) devices. Cavity improvements and performances are detailed.

Furthermore, lasing dynamics and temporal effects in novel monolithic fiber lasers employing a specialty gain MCF are investigated. Competition mechanisms between amplified supermodes have been extracted from the first supermode-resolved gain analysis experiment. In addition, the first self-mode-locking effects in a linear MCF fiber laser cavity are presented.

Finally, Chapter 7 summarizes the highlights of this dissertation and gives a research outlook for the prospects of specialty optical fibers.

CHAPTER 2: PRINCIPLES OF LIGHT PROPAGATION IN SPECIALTY FIBERS

This chapter provides the background knowledge and fundamental principles which are necessary to understand the body of the dissertation. The fundamental concepts of light propagation in dielectric waveguides are derived in Section 2.1 followed by a general presentation of single-mode and multi-mode fibers in Section 0. The concept of Multi-Mode Interference, widely used in the present research, is numerically introduced in Section 2.3. Finally, external methods to control the transverse mode content, i.e. excitation, suppression and conversion, are presented in Section 2.4.

2.1 Theory of light propagation in optical fibers

In this paragraph, the equations describing the properties of monochromatic light propagating in a given medium are derived. For simplicity, the simple case of a step-index fiber (SIF) made of a core surrounded by a cladding layer is considered. The transverse distribution of the refractive index $n(r)$ is defined by

$$n(r) = n_1 \text{ for } 0 \leq r \leq a \quad (1)$$

$$n(r) = n_2 \text{ for } r > a \quad (2)$$

where a is the SIF core radius. In SIF, light is confined by internal reflection (TIR) which is achieved at the core/cladding boundary when $n_1 > n_2$.

2.1.1 The wave equation

Optical fibers are a particular case of dielectric waveguide characterized with a cylindrical geometry. In the following, the equations introduced were directly inspired from the fundamental books by Saleh *et al.* [31], Marcuse [32], and Ghatak *et al.* [33]. The propagation of electromagnetic waves in a given medium is governed by the well-known Maxwell's equations

$$\nabla \times \boldsymbol{E} = -i\omega\mu_0 \boldsymbol{H} \quad (3)$$

$$\nabla \times \boldsymbol{H} = i\omega\varepsilon_0 n^2 \boldsymbol{E} \quad (4)$$

with $\boldsymbol{E}$ and $\boldsymbol{H}$ the electric and magnetic components of the field respectively. In conventional SIF, the wave equation satisfies the paraxial approximation, when the refractive index difference between the core and cladding glasses in small on the order of $\sim 10^{-3}$. Under this assumption, each component of the electric and magnetic field must satisfy the paraxial approximation of the wave equation, well-known as the Helmholtz equation

$$\nabla^2 \Psi + n(r)^2 k_0^2 \Psi = 0, \quad (5)$$

where ∇ is the Laplacian operator and k_0 the wavevector defined by

$$k_0 = \frac{2\pi}{\lambda_0} \quad (6)$$

with λ_0 the light wavelength. This equation is verified at any point in space in the core and in the cladding regions of the SIF. Since optical fibers are cylindrical waveguides, the Helmholtz equation can be expressed in cylindrical coordinates, according to

$$\frac{\partial^2 \Psi}{\partial r^2} + \frac{1}{r}\frac{\partial \Psi}{\partial r} + \frac{1}{r^2}\frac{\partial^2 \Psi}{\partial \phi^2} + \frac{\partial^2 \Psi}{\partial z^2} + n^2 {k_0}^2 \Psi = 0 \quad (7)$$

with $\Psi = \Psi(r, \phi, z)$. Due to the radial dependence of the refractive index $n(r)$, under the paraxial approximation, for homogeneous and isotropic materials, solutions of Equation (7) can be written under the form

$$\Psi(r, \phi, z) = \psi(r, \phi) e^{-j\beta z} \quad (8)$$

with β the propagation constant of the propagating wave defined by

$$\beta(r) = \frac{2\pi}{\lambda_0} n(r) = \frac{\omega}{c} n(r). \quad (9)$$

The scalar wave equation is obtained from substituting solutions (8) into Equation(7) resulting in

$$\left(\nabla_t^2 + n(r, \phi)^2 {k_0}^2 - \beta^2\right)\psi(r, \phi) = 0 \quad (10)$$

with $\nabla_t^2 = \nabla^2 - \partial^2/\partial z^2$. Solving this equation is an eigenvalue problem where only a finite number of solutions exist. These eigenfunctions $\psi(r, \varphi)$ are also called transverse modes with eigenvalues β, the propagation constant of each transverse mode. Eigenfunctions solutions of equation (10), must satisfy (a) continuity at the interfaces and (b) infinity boundary conditions. Thus, each fiber region (core or cladding) carries a specific set of transverse modes.

2.1.2 Introduction to transverse modes

According to the boundary condition for which Equation (10) is solved, different types of eigenfunctions, i.e. transvers emodes, will be found. In the fiber core, i.e. the confinement region, eigenfunctions are oscillatory functions and Equation (10) satisfies the condition

$$\left\{n(r, \phi)^2 {k_0}^2 - \beta^2\right\} > 0. \quad (11)$$

In addition, the confined field must decay exponentially outside the core and at infinity. This condition on Equation (10) translates into

$$\{n(r=\infty,\phi)^2 {k_0}^2 - \beta^2\} < 0. \quad (12)$$

As a result, different types of transverse modes propagating in optical fibers;

- Guided modes are eigenfunctions characterized by an intensity distribution confined close to the center of the core which decays exponentially in the cladding region. Losses associated with light propagation are generally low.
- Leaky modes are also concentrated around the core but with evanescent tails penetrating deeper in the cladding region resulting in less confinement and higher propagation losses.
- Cladding modes are filling the cladding region of the optical fiber. They generally extend in the fiber core and outside the outer surface and suffer from significant propagation losses.

Since the fiber boundaries are defined by a change in the refractive index and that the refractive index only depends on the radial coordinate, the transverse mode structure can be factorized using

$$\psi_{lm}(r,\phi) = \varphi_{lm}(r).\Phi(l\phi) \quad (13)$$

with l an integer, $\Phi(l\phi)$ an oscillatory function defined by

$$\Phi(l\phi) = \begin{cases} cos(l\phi)\ for\ "even"\ modes \\ sin(l\phi)\ for\ "odd"\ modes \end{cases} \quad (14)$$

and $\varphi_{lm}(r)$ solution of the second-order differential equation

$$\frac{d^2\varphi_{lm}}{dr^2} + \frac{1}{r}\frac{d\varphi_{lm}}{dr} + \left(n(r)^2 {k_0}^2 - \beta_{lm}^2 - \frac{l^2}{r^2}\right)\varphi_{lm} = 0. \quad (15)$$

Solutions of the Equation (15) are the well- known Bessel functions and the solutions are of the form

$$\varphi_{lm}(r) = C \times \begin{cases} \dfrac{J_l(Ur/a)}{J_l(U)} & r \leq a \\ \dfrac{K_l(Wr/a)}{K_l(W)} & r > a \end{cases} \quad (16)$$

with J_l the Bessel function of the first kind and l^{th} order, K_l the modified Bessel function of the second kind and l^{th} order and C a normalization factor. The values for U and W are calculated from the characteristic equations

$$U\frac{J_{l+1}(U)}{J_l(U)} = W\frac{K_{l+1}(W)}{K_l(W)} \quad (17)$$

and

$$U^2 + W^2 = V^2. \quad (18)$$

The variable V is the well-known fiber V-parameter defined by

$$V = \frac{2\pi}{\lambda} a\sqrt{n_1^2 - n_2^2}. \quad (19)$$

This equation can be simplified by introducing the numerical aperture (NA) of a SIF defined by

$$NA = \sqrt{n_1^2 - n_2^2}. \quad (20)$$

The values of U and W are then expressed as

$$U = a\sqrt{k_0^2 n_1^2 - \beta^2} \quad (21)$$

$$W = a\sqrt{\beta^2 - k_0^2 n_2^2}. \quad (22)$$

In order to be guided in the fiber core, the propagation constant of each transverse mode must fulfill the condition $n_2^2 k_0^2 < \beta^2 < n_1^2 k_0^2$ and the values of U and W must be real. The radial distribution of the transverse modes $\varphi_{lm}(r)$ in the fiber core depends on the order l of the Bessel functions. The transverse modes cut-off correspond to the zeros of the Bessel functions of order l

and, for a given value of l, there is a finite number of transverse modes guided in the fiber core. Each solution is indexed with an integer m ($m \geq 1$) and is called a linearly polarized (LP_{lm}) mode. For $l = 0$, modes are ϕ independent and two-fold polarization degenerated. If $l \geq 1$, modes are four-fold polarization degenerated.

The guided modes cut-off values are summarized in Table 2. One can determine the number of guided modes in a fiber core using the fiber V-parameter defined in Equation (19). For example, the V-parameter of the standard telecommunication SIF labeled SMF28 with ~ 9 μm core diameter and NA ~ 0.12 at λ_0 = 1.55 μm light wavelength is V = 2.19. According to Table 2, only one mode is guided in the core of this fiber. The corresponding mode is labelled LP_{01} and referred to as the fundamental mode (FM). The FM is always guided in optical fibers.

Table 2: Cut-off values of the first guided LP_{lm} modes

V-parameter	**$LP_{0,m}$**	**$LP_{1,m}$**	**$LP_{2,m}$**	**$LP_{3,m}$**
m = 1	0	2.4048	3.8317	5.1356
m = 2	3.8317	5.5201	7.0156	8.4172
m = 3	7.0156	8.6537	-	-

The calculated intensities of the first $LP_{l,m}$ modes are shown in Figure 2-1. Above the single-mode cut-off, defined with $V >$2.405, additional LP_{lm} modes (called higher-order modes or HOMs) are guided in the fiber core. The n^{th} guided modes propagates with a propagation constant β_n (defined in Equation (9)), corresponding to an effective index labeled $n_{eff,n}$. Two modes propagating with the same propagation constant are degenerated. During light propagation, the FM has the highest $n_{eff,n}$ value while transverse modes for which $n_{eff,n} < n_2$ propagate in the cladding.

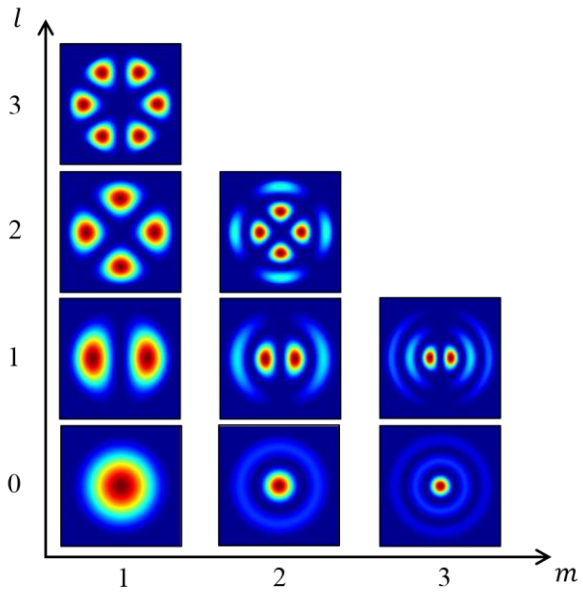

Figure 2-1: Calculated intensity profiles of the first LP_{lm} modes. Whereas LP_{0m} modes exhibit circularly symmetric profiles, other LP_{lm} modes have one or multiple radial phase singularities.

Since the propagation constant β_n is a function of the light frequency ω, it can be decomposed in a Taylor expansion around the center frequency ω_0 such as

$$\beta_n(\omega_0 + \omega) \approx \frac{\beta_n(\omega_0)}{\omega} + \left.\frac{d\beta_n}{d\omega}\right|_{\omega_0} + \frac{\omega}{2}.\left.\frac{d^2\beta_n}{d\omega^2}\right|_{\omega_0} + \cdots. \quad (23)$$

Each term of the Taylor expansion can be identified as a physical quantity, characteristic of the propagation of the n^{th} transverse mode;

- The phase velocity v_P, corresponds to the speed at which the phase of each frequency component travels:

$$v_P = \frac{\omega}{\beta_n}. \quad (24)$$

- The group velocity v_G defines the speed at which the envelope of a pulse propagates in a medium:

$$v_G = \left(\frac{\partial \beta}{\partial \omega}\right)^{-1}. \quad (25)$$

- The group velocity dispersion GVD describes the frequency (or wavelength) dependence of the group delay when the electromagnetic wave travels in a transparent medium:

$$\mathrm{GVD} = \frac{\partial}{\partial \omega}\frac{1}{\mathrm{v_G}} = \frac{\partial^2 \beta}{\partial \omega^2}. \quad (26)$$

The group delay of the n^{th} guided mode, labeled τ_n, is defined as the time the mode takes to propagate along the fiber length L, and can be expressed as:

$$\tau_n = \frac{L}{v_P} = \frac{\beta_n}{\omega} L = \frac{1}{c} n_{eff,n} L. \quad (27)$$

As a result, two non-degenerated modes will propagate along the fiber with a Differential Group Delay (DGD) defined by $DGD = \tau_1 - \tau_2$ (for two modes labeled 1 and 2 respectively) corresponding to:

$$DGD = \frac{L}{c}\left(n_{eff,1} - n_{eff,2}\right). \quad (28)$$

2.2 Single-mode and multi-mode fibers

Two SIF categories are distinguished according to the number of transverse modes guided in the core: Single-Mode Fibers and Multi-Mode Fibers.

2.2.1 Single-mode fibers

Single-mode fibers (SMF) are designed to fulfill the single mode cut-off condition corresponding to a V-parameter value < 2.405. This condition is reached at a particular light

wavelength by adjusting the core diameter and the relative core-cladding index difference. When the single-mode condition is satisfied, only the fundamental mode LP_{01} is guided. SMFs are extremely popular for delivering beams with Gaussian-like intensity distribution with diffraction-limited beam quality.

The most common SMF (SMF28 fabricated and commercialized by Corning Inc.) is a cost-effective device widely used in telecommunications applications and in fiber-integrated optical devices. However, the small value of its core diameter (~ 9 μm), chosen to achieve single-mode beam delivery, limits the number its applications in particular in the development of fiber lasers delivering high performances beam [34].

According to the definition of the V-parameter in Equation (19), further increasing the core diameter leads to the apparition of multiple guided LP_{lm} modes. It is possible to limit the number of guided HOMs by reducing the fiber NA. This concept has been applied to fabricate so-called Large-Mode Area fibers. For example, single-mode operation can be obtained in step-index LMA fiber designs with core diameters up to 25 μm in diameter and NA as low as ~ 0.06, to be used in fiber laser and amplifier systems [35]. However, there is a fundamental limitation in the smallest NA achievable in SIF designs. This is due to the smallest core-cladding refractive index difference that can be experimentally realized. This effect compromises the single-mode delivery when further scaling the fiber dimensions [36].

In order to address this limitation, a promising alternative has been proposed using novel fiber designs with a micro-structured cladding to achieve single-mode guidance [37]. To date, Photonic Crystal Fibers (PCF) are the preferred designs to achieve single-mode from scaled core sizes. Endlessy single-mode operation in PCF was reported for the first time by Knights *et al.* [5], [6]. Since then, this field has drastically evolved, and PCF designs made with active cores as large

as 135 μm in diameter were reported in fiber lasers emitting record power levels and good beam quality [38]. Other fiber designs have been proposed such as Photonic Band-Gap (PBG) fibers [12], ribbon fiber [23], and Chirally-Coupled Cores (CCC) fibers [24] (more details can be found in Chapter 4 and Chapter 5).

A different approach to deliver single-mode beams in active LMA fibers is based on the technique of gain filtering which consists in a controlled engineering of the gain profile across the fiber core in order to ensure single-mode emission [41].

2.2.2 Multi-mode fibers

On the other hand, Multi-Mode Fibers (MMF) correspond to any fiber design guiding more than the one transverse mode. The most common MMF designs are all-solid structures with step-index profiles and graded index profiles [32]. This second type of MMF will be presented in details in Section 5.2.1. In this paragraph, rather than elaborating a list of all MMFs applications, the equations describing light propagation in MMFs are be provided.

The total beam emerging a MMF supporting n transverse modes, labeled E, is made of a linear superposition of the n^{th} guided transverse modes $\varphi_n(r)$ and it can be expressed as

$$E(r) = \sum_{n=1}^{n_{max}} c_n \varphi_n(r) \qquad (29)$$

where c_n is the modal coefficients. The LP modes, eigensolutions of the wave equation (Equation (10)), are orthornormal and satisfy

$$\langle \varphi_n, \varphi_p \rangle = \iint \varphi_n^*(r) \varphi_p(r) d^2r = \delta_{np}. \qquad (30)$$

In addition, the modal coefficients c_n can be expressed by

$$c_n = \rho_n \, exp(i\phi_n) = \langle \varphi_n, E \rangle = \iint \varphi_n^*(r) E(r) d^2 r, \quad (31)$$

and satisfy the relation

$$\sum |c_n|^2 = \sum \rho_n^2 = 1 \quad (32)$$

with ρ_n^2 introduced as the Mode Power (MP) carried by the n^{th} mode.

2.3 The phenomenon of multi-mode interference and self-imaging

In MMFs, several modes simultaneously propagate, each one at a specific propagation constants β_n. As a result, a characteristic phenomenon, called Multi-Mode Interference (MMI), occurs during light propagation. In this section, the simple case of two guided modes is chosen to describe MMI. The total field $E(r, z)$ emerging the two-modes optical fiber can be written as

$$E(r, z) = e^{i\beta_1 z}\{c_1 \varphi_1(r) + c_2 \varphi_2(r) e^{i(\beta_2 - \beta_2)z}\}, \quad (33)$$

the linear sum of the two guided modes, labeled 1 and 2. In practice, the measurable quantity is the intensity of the light delivered by the fiber. The intensity is defined by $I(r, z) = |E(r, z)|^2$ and, according to Equation (33), the argument of the second exponential exhibits an oscillatory behavior as function of the light wavelength λ and of the propagation distance z along the fiber length. Calculation details can be found in Appendix A. This oscillatory effect is called MMI. In the case of a two-modes fiber, the result is a periodic behavior characterized with a period $\Delta\phi$ defined by

$$\Delta\phi(\lambda) = \frac{2\pi}{\lambda}\left(n_{eff,2} - n_{eff,1}\right)L. \quad (34)$$

A specific property of MMI, called self-imaging, correspond to fiber locations at which the incident field is reconstructed [42]. After travelling a certain length along the fiber, called self-

reproduction length (SRL), the initial phase relation between the transverse modes is reproduce and the initial field is retrieved. Self-imaging is achieved when the condition

$$|E(r,z)| = |E(r,0)| \quad (35)$$

is satisfied which imposes a condition on the argument of the exponent in (33) resulting in the equation defining the SRL, labeled z_m, to be

$$z_m(\lambda) = \frac{m/2}{\beta_1(\lambda) - \beta_2(\lambda)} \quad (36)$$

with m an integer. As a result, self-imaging occurs in MMF either at periodic length intervals (for a fixed fiber length) or periodic length intervals (for a fixed light wavelength). Several applications have been demonstrated using MMI and self-imaging in MMF including displacement sensors [43], temperature sensor [44], tunable spectral filters [45], bandpass filter [46], optical switches [47], all-fiber MFAs (details can be found in Chapter 4) [48] and more.

2.4 External methods to control the guided mode content

In practice, an optical fiber undergoes perturbations depending on their environment which might affect the propagating light, i.e. the guided mode content. Here, three approaches to externally control the guided mode content in optical fibers are presented starting with the incident mode-overlap and then followed by the influence of the fiber coiling. Finally, a recently demonstrated method control the guided mode content using holographic phase masks is briefly introduced.

2.4.1 Choice of the mode excitation

Even though an optical fiber is designed to guide a certain number of LP modes, the combination of modes excited and propagating in the fiber depends on the overlap between the incident beam and the fiber core. An input SMF delivering a Gaussian beam E_{in} of the form

$$E_{in}(r,z) = e^{-\left(\frac{r}{\omega_0}\right)^2} e^{-i\beta Z} \quad (37)$$

is considered. For such beams, the value of the waist ω_0 can be empirically determined [49] using the relation

$$\omega_0 = \frac{2a}{\sqrt{2ln2}}(0.65 + 1.619V^{-1.5} + 2.879V^6). \quad (38)$$

When using the SMF to couple light in a second fiber with different core size, the coupling loss at the fiber interface are proportional to the waist mismatch between the two fibers [49]. This issue is addressed employing all-fiber mode-field adapters in Chapter 5 of this dissertation.

Most interestingly, the coupling coefficient between the incident SMF and the n^{th} mode ($E_n(r,z)$) guided in a Few-Modes Fiber (FMF) is determined using the overlap integral

$$c_n = \frac{\left|\int_0^\infty E_{in}(r)E_n(r)rdr\right|^2}{\int_0^\infty |E_{in}(r)|^2 rdr \int_0^\infty |E_n(r)|^2 rdr}. \quad (39)$$

In other words, the relative alignment between the SMF and the FMF influences the combination of modes excited in the FMF. This phenomenon has been experimentally measured after recording the beam emerging a FMF with a CCD while changing the coupling alignment. This situation is illustrated in Figure 2-2 (a). When the SMF and FMF cores overlap, the power transfer from the incident LP_{01} mode only into the circularly symmetric modes labeled $LP_{0,m}$. This is represented by the yellow dot in Figure 2-2(b). As the input SMF was misaligned from the FMF core center,

(red dots in Figure 2-2(b)), some fraction of the power was coupled in other overlapping HOM. These experimental observations can be completed by citing the work of Flamm *et al.* who quantified the impact of fiber-to-fiber coupling using an advanced mode analysis technique [50].

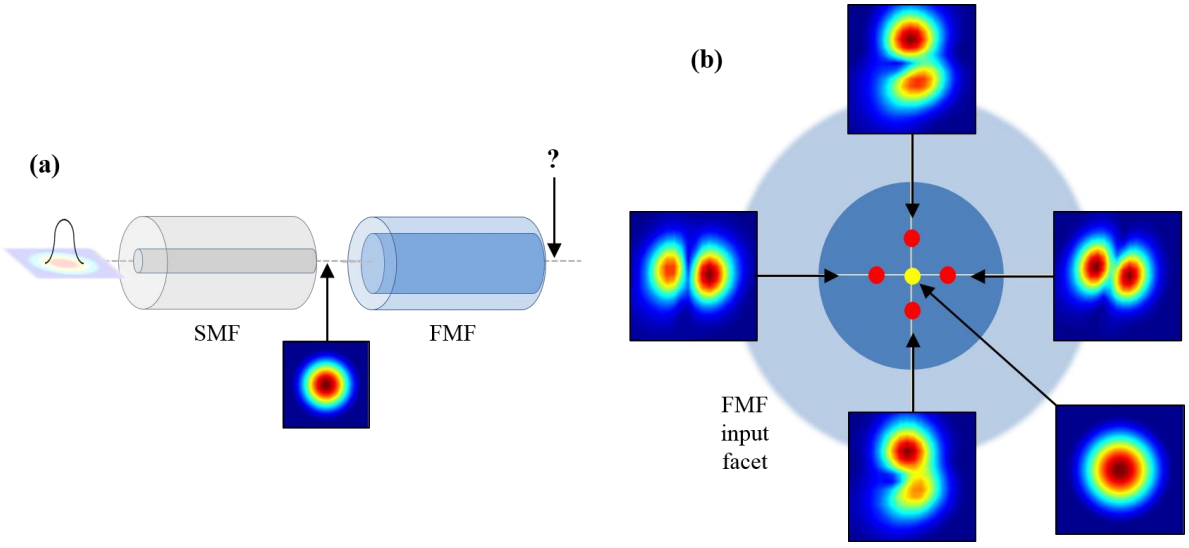

Figure 2-2: (a) Illustration of the coupling alignment between the SMF and a MMF. (b) Measured beam profile at the MMF output after changing the in-coupling alignment. Centered alignment resulted in a LP_{01}-like profile whereas HOM content was measured after perturbing the in-coupling alignment.

As a result, the propagating mode content in an optical fiber, regarding guided mode content and relative mode powers, can be controlled by proper alignment of the FMF facet with respect to the input delivery fiber.

2.4.2 Influence of coiling optical fibers on the guided modes

Up to this point, straight pieces of fiber have been considered. However, coiling an optical fiber changes the boundary conditions used to solve the wave equation (Equation (10)), resulting in a direct influence on the modes propagating in the fiber. Several analytical approaches have been proposed to characterize the effect of coiling [51], [52]. It has been demonstrated that,

bending the fiber not only induces distortions in the profile of the guided modes but also, cladding-coupling can occur for the n^{th} mode when the fiber is coiled under a limit radius labeled $R_{lim,n}$. As a result, the HOM is suppressed due to the large scattering loss at the cladding/outside interface.

These concepts are both illustrated in Figure 2-3. Starting from a non-perturbed fiber with 4 guided LP modes indicated by the bark blue lines (Figure 2-3(a)). The coil-induced changes in refractive index profile are illustrated in (b) resulting in 3 out of the 4 guided modes being coupled into leaky cladding modes. According to [34], $R_{lim,n}$ can be expressed as

$$R_{lim,n} = \frac{2V}{1 - b_n}, \tag{40}$$

with b_n the normalized propagation constant of the n^{th} mode defined by the effective index $n_{eff,n}$ such that

$$b_n = \frac{n_{eff,n}^2 - n_2^2}{n_1^2 - n_2^2}. \tag{41}$$

The influence of fiber coiling on the mode profile is also illustrated in Figure 2-3. Compared to the non-perturbed Gaussian mode field amplitude $|E|$ presented in (a), coiling the fiber results in spatial distortions which are schematically represented in (b). Detailed analysis of the beam distortions resulting from fiber coiling has been reported by Schermer et al. [52]. As a result, the depth of penetration of the evanescent tails of the field in the cladding influences the mode confinement and directly impacts the properties of the guided light.

Thus, controlled coiling of an optical fiber is one of the most accessible method to suppress residual HOM content. It should be noticed that, in some cases, the bend-induced losses might have a significant impact on the overall propagation losses in the fiber. Also, coil-induced birefringence has been demonstrated in optical fibers to control the polarization orientation of

guided light [53]. On the other hand, some applications require coil-insensitive fibers which were obtained by tailoring the fiber design using, for example, trench-assisted fiber cores [54], [55]. The effect of fiber coiling on the guided HOM content is studied in details in Sections 4.1 and 4.2 of this dissertation.

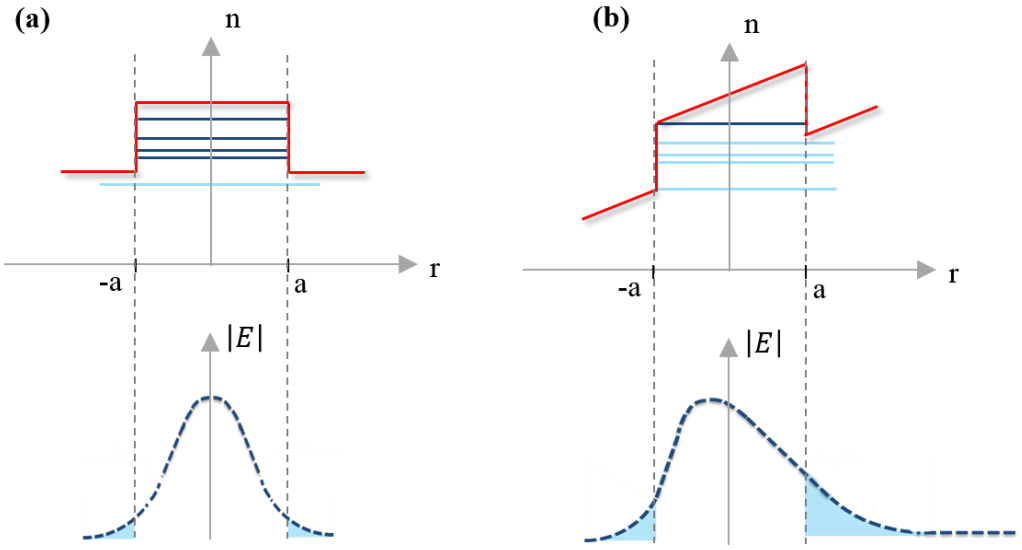

Figure 2-3: (a) Case of a non-perturbed multi-mode fiber (MMF): (top) index profile indicating 4 LP modes guided (dark blue lines) and the first cladding mode (light blue line) and the field amplitude $|E|$ of one of the guided mode (bottom). (b) Case of a perturbed MMF illustrating the coiling influence on the guided modes (1 guided and 4 leaky) and on the mode profile (spatial distortions appear).

2.4.3 Mode conversion employing holographic phase masks

This paragraph introduces a novel approach to manipulate the mode content guided in optical fibers via mode conversion. To date, mode conversion has been demonstrated using fiber Bragg gratings (FBG) [56]–[58], segments of MMF [59], microbend gratings [60] and pressure assisted mode conversion [61]. Here, we investigate the possibility to perform mode conversion in an all-fiber scheme using holographic phase mask (HPM) inscribed in Photo-Thermo Refractive (PTR) glass. PTR glass is a multicomponent, highly photosensitive glass which is well-known in

applications using inscribed binary phase elements [62] and volume Bragg gratings, in particular for wavelength stabilization of laser emission [63] and beam combining applications [64].

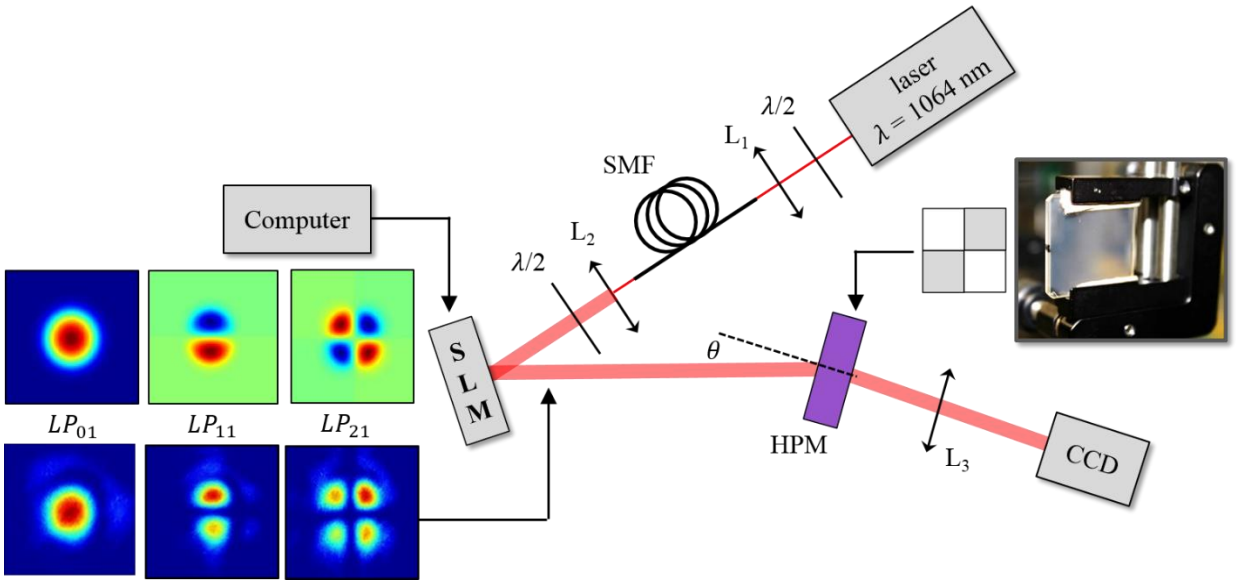

Figure 2-4: Proof-of-concept experiment to measured LP mode conversion using a four quadrants HPM in PTR glass. Light from a laser source is coupled in a SMF and incident on the SLM. Four LP modes can be modulated on the SLM via computer control: LP_{01}, LP_{11e}, LP_{11o} and LP_{21}.Under proper alignment on the HPM, the diffracted far-field is imaged using L_3 on a CCD to record the converted beam.

The following study was motived from the combination of two ideas: (a) the successful demonstration of the first step-index fiber made of PTR glass [17] in which local refractive index changes can be induces using beam a light beam, and (b) the ability to fabricate HPM devices in PTR substrates, used, to date, to achieve mode conversion between free-space TEM modes [65]. In order to determine if HPM could be used in PTR fibers to achieve in-fiber mode conversion, a proof-of-concept experimental setup has been assembled. Illustrated in Figure 2-4, a computer-controlled Spatial Light Modulator (SLM) was used in order to generate individual LP_{lm} modes (using the encoding technique from Arrizon *et al.* [66]). A laser emitting at λ = 1064 nm is coupled in a SMF to ensure Gaussian-shaped beam amplitude, collimated and incident on the SLM.

Generated LP_{lm} modes are incident on the HPM to measure "up-conversion" (from LP_{01} to HOMs) or "down-conversion" (from HOM to LP_{01}). A schematic of the four quadrants HPM used in this experiment is shown in Figure 2-4 along with a picture of the real device. Each quadrant is phase shifted by π. Under proper angular alignment on a selected section of the HPM, the incident beam is diffracted and converted. The mode conversion is measured after imaging the beam in the far field with a convex lens and recording the corresponding intensity with a CCD. This experiment and detailed results of the mode conversion analysis have been recently submitted for publication [67].

2.4.3.1 Up-conversion from LP_{01} to HOMs.

By properly aligning the incident LP_{01} mode on the HPM, several mode conversion combinations could be achieved. The experimental situation corresponding to the conversion between LP_{01} and LP_{11e}, LP_{01} and LP_{11o} and LP_{01} and LP_{21}, are illustrated in Figure 2-5. The corresponding location on the HPM are indicated with (a), (b) and (c) respectively, corresponding to different phase jumps.

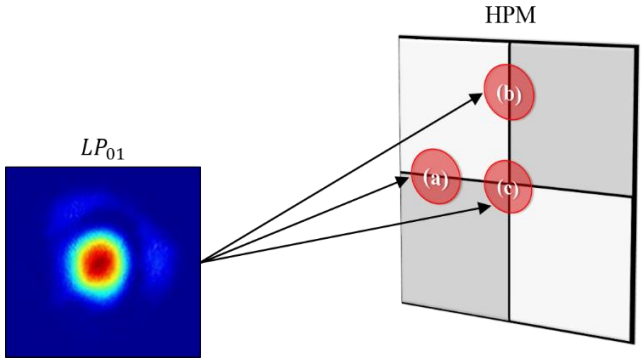

Figure 2-5: Schematic of the HPM alignment to achieve (a) LP_{01} to LP_{11e}mode conversion, (b) LP_{01} and LP_{11o} and (c) LP_{01} and LP_{21}.

The conversion from LP_{01} into the HOMs LP_{11e}, LP_{11o} and LP_{21} has been recorded on the CCD and results are shown in Figure 2-6(a), (b) and (c) respectively. For each converted beam, a transverse cut of the intensity profile has been plotted along the dotted line. As a result, the measurement of the converted modes show is in good agreement with the theoretical mode profile expected. In addition, the intensity reaches zero at each phase singularity indicating a good quality of modal conversion. A first estimation of the conversion efficiencies was measured by comparing the power measured before the HPM to the power in the converted mode. Result are shown in Figure 2-6 indicating ~70% efficiency. It was demonstrated that these high efficiencies are in agreement with theoretical predictions [67].

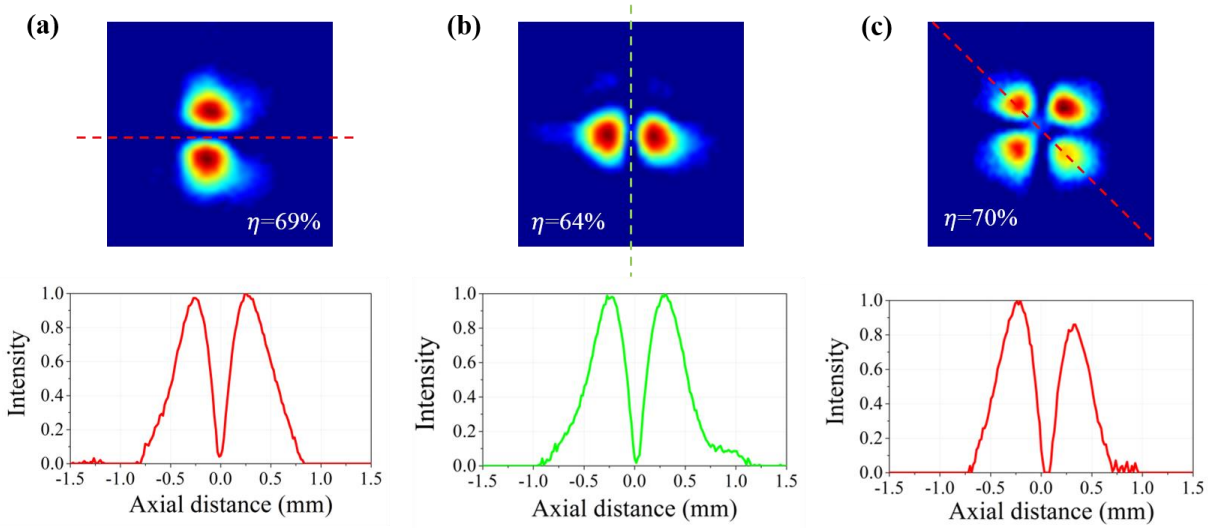

Figure 2-6: Results of the up-conversion from LP_{01} to the HOMs LP_{11e}, LP_{11o} and LP_{21}. The mode conversions are realized using a single HPM device while changing the alignment of the LP_{01} mode according to the phase singularities.

2.4.3.2 Down-conversion: example of LP_{21} converted into LP_{01}

Results from the down-conversion measurement are summarized in Figure 2-7. Following the same principle as the up-conversion experiment, the HOM LP_{21} was generated with the SLM

and, after proper alignment with the center of the HPM (illustrated with the red dot in Figure 2-7), the converted beam was recorded with the CCD with up to 65% efficiency. One can notice the presence of side lobes on the converted LP_{01} mode profile which can be minimized via further optimization of the HPM parameters and of the optical alignment.

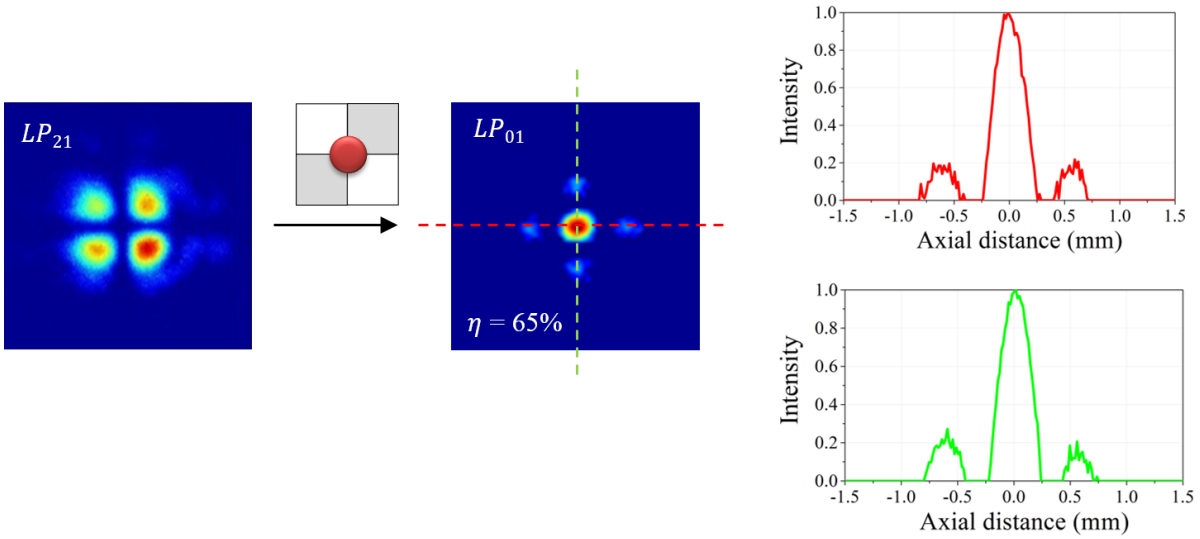

Figure 2-7: Results from down-conversion from LP_{21} (generated with the SLM) to LP_{01}.

In summary, the proof of concept has been verified since efficient *LP* mode conversion could be achieved with the HPM.As a result, it seems possible to achieve mode conversion in all-fiber devices using PTR glass fibers in which a HPM could be inscribed opening the route towards all-integrated fiber-based mode converters.

2.5 Summary

The fundamental equations describing the properties of light propagation in single-mode and multi-mode optical fibers have been introduced, and will be properly referenced in the upcoming sections of this dissertation. In addition, practical considerations were discussed regarding the influence of external perturbations on the guided light. In particular, it was

demonstrated that the mode content excited and propagating in a MMF can be chosen by controlling (a) the in-coupling alignment (individual mode coefficients c_n are defined by the overlap integral Equation (39)) and (b) the fiber coil (limit radius $R_{lim,n}$ before attenuating HOM content by cladding-mode coupling). These results were analytically described and experimentally demonstrated. Finally, mode conversion with ~70% efficiency (in average) was measured for up and down conversion between the FM LP_{01} and the HOMs LP_{11e}, LP_{11o} and LP_{21} employing a novel HPM device.

CHAPTER 3: ADVANCED TOOLS FOR MODE ANALYSIS IN OPTICAL FIBERS

Diagnostic tools to characterize conventional step-index and gradded-index optical fibers are many and common. For example, microscopes, SEM and other imaging techniques are used to measure fiber facets and extract the shape and sizes of inner-structures. Light transmission experiments and cut-back methods are standard diagnostics to evaluate the spectral response and the attenuation in optical fibers. On the other hand, piece of equipment to measure more specific fiber parameters are commercially available such as fiber profilometer (Interfiber Analysis, introduced in details in Section 3.4.1), used to measure the refractive indices across a fiber cross-section as well as stress distribution, optical backscatter reflectometer (LUMA Technologies), to locate scattering centers within tens of meters of fiber length, and more. In addition, it is possible to detect a single-mode beam from a highly multi-mode beam using a single CCD measurement since the speckle-like intensity pattern emerging MMF is unambiguous.

Within the past few years, an increasing number and variety of specialty fibers have been demonstrated to satisfy targeted applications. In many cases, specialty fibers are designed to achieve very specific polarization, spatial or modal properties which cannot be accurately measured with existing characterization techniques. For example, it is particularly challenging to resolve weakly guided HOMs since their contribution to the beam emerging an optical fiber is less than a few percent. A good example is the case of the measurement of the M^2 paremeter. This technique is by far the most common one to evaluate the quality of the total beam emerging an

optical fiber with M^2 = 1 corresponding to an ideal Gaussian beam [68]. However, in the case of few-modes specialty fibers propagating a few weakly guided modes, it has been demonstrated that even beams with Gaussian-like intensity profiles can contain small fractions of HOMs [69]. This can be emphasized considering that the total field emerging an optical fiber is the weighted sum of all propagating modes (see Section 2.2.2) and the contribution from weakly guided modes is negligible. Thus, M^2 measurements cannot be trusted when measuring the beam emerging from few-modes fibers since it is a measurement of the quality of the overall beam without access to individual transvers modes.

In this context, this chapter is dedicated to a novel generation of advanced diagnostic tools called mode analysis. These techniques were introduced within the past few years, following the evolution of specialty fiber designs, and were demonstrated to decompose the total field propagating in an optical fiber into the sum of individual transverse mode. The first Section 3.1 offers an overview the field of mode analysis techniques, providing a comprehensive overview of the techniques demonstrated to the date of this dissertation and their respective ability to measure individual field amplitude, phase distribution, state of polarization or mode fractional power. The accent is then put on the two mostly used methods: on one hand spatially and spectrally resolved imaging, also called S^2 imaging (Section3.2), and on the other hand the correlation filter method, labeled CFM (Section 3.3). Furthermore, Section3.4 of this chapter presents the first experimental determination of the working range of S^2 imaging and CFM analysis. As a result, the accuracy of each technique will be discussed after decomposing a wide variety of fiber beams. To the best of our knowledge, this is the first demonstration of the mode detection limit of S^2 imaging and CFM. These results are expected to be used in the long run to drastically improve the accuracy of the mode evaluation.

3.1 Modal decomposition in optical fibers: state-of-the-art

Several methods to perform mode analysis of optical fiber beams have been demonstrated in the past few years. This section presents a complete list of the techniques reported to the date of this dissertation, sorted in a chronological order, along with the relevant references which can be used to gain more insight on each method.

One of the first method to decompose multi-mode beams in the sum of individual *LP* modes with access to their fractional modal weight was reported by Soh *et al.* in 2004 [70]. This numerical approach was directly inspired from the previous work of Gori *et al.* [71], [72] who demonstrated the first decomposition of multi-mode Hermite-Gauss beams using the orthogonally of the Fourier-transformed modal intensity functions. The principle was based on an intensity measurement recorded after propagation of the fiber beam through a linear polarizer and a Fourier lens.

The access to individual modes is often limited by the lack of information regarding the phase singularities, in particular when using intensity based measurement. To address this issue, Shapira *et al.* reported a method using polarization sensitive near-field and far-field measurements of a fiber beam [73]. The authors used an iterative algorithm to determine the modal phase [74], [75] which, in parallel to an intensity measurement, enabled to reconstruct the total beam emerging the optical fiber.

Later on, Andermahr *et al.* demonstrated an experiment to resolve individual Mode Power (MP) values ρ_n^2 and state of polarization of *LP* modes. The concept was based on matching the *LP* modes guided in the fiber with the Hermite-Gauss modes of a three-mirror ring resonator [76].

In 2008, Nicholson *et al.* introduced the spectrally and spatially resolved imaging, so-called S^2 imaging technique [77]. The MP (ρ_n^2) of individual *LP* modes could be resolved using a Fourier

treatment of the measured Multi-Mode Interference (MMI) in the fiber (see Section 2.3). In addition, this technique was the first experimental method enabling to reconstruct individual mode amplitude and phase profiles [78].

The correlation filter method (CFM), first introduced by Kaiser *et al.* [79] is a purely experimental and unambiguous method to decompose arbitrary mode contents, evaluate individual MP and reconstruct vector-valued beams. The center piece of CFM is a correlation filter, used in a simple imaging setup, which has been carefully design according to the fiber investigated [80], [81].

Low-coherence interferometry techniques, using an interferometric experiment and a Fourier analysis, were first introduced to measure the dispersion in optical fibers [82]. More recently low-coherence interferometry has been successfully implemented to measure the relative group delay, the amplitude and phase profile of individual guided modes in optical fibers and fiber devices [83], [84]. The cross-correlated imaging technique (C^2 imaging) is the most recent implementation of low-coherence interferometry, providing access to small intermodal delays without prior knowledge of the optical waveguide [85].

Finally, a method employing high speed cameras in parallel with the intensity measurement reported by Soh *et al*.[70] was demonstrated to investigate the particular phenomenon of mode instabilities occurring above certain lasing threshold in high power fiber lasers [86].

Each one of these mode analysis technique is based on unique procedures, using either numerical or experimental approaches (or both) to access modal properties such as individual MP values, modal amplitude and phase distribution, state of polarization, inter-modal delay, modal dispersion. In the two next paragraphs of this chapter, the accent is put on two of the most widely used techniques, namely S^2 imaging and CFM.

3.2 Spatially and spectrally resolved imaging (S^2 imaging)

3.2.1 Introduction and principle of operation

The S^2 imaging technique is based on the measurement of MMI occurring during light propagation in few-modes fibers [77]. This phenomenon was introduced in Section 2.3, arising from the interference between transverse modes propagating simultaneously in a fiber with different propagation constants β_n. The results is an oscillatory behavior which can be spectrally resolved since the period of the oscillations, defined in Equation (34), is a function of the propagation length and the light wavelength. In S^2 imaging, the fiber length is fixed while a broadband light source is used to measure the MMI. After measuring the spectral response from the few-modes fiber at several locations across the fiber beam, the Differential Group Delay (DGD), defined in Equation (28) and proportional to the MMI period (see Appendix B, Equation (65)), is extracted from a Fourier analysis of the experimental data. The modal amplitudes and phase profiles as well as the MP values ρ_n^2 are measured.

Recent modal decomposition performed with the S^2 imaging mode analysis include LMA fibers [77], [78], PCF [87], all-solid and hollow core PBG fibers [88], [89], LCFs [22], CCC fibers with core diameters > 50 μm [90] as well as extended long tapers [91] and 2 μm wide silicone waveguides [92]. The range of applications of S^2 imaging has been extended to measure HOM bend-induced losses [93], efficient HOM suppression in scalable output fiber amplifiers [94]. It has also been used to understand increased performances of Q-switched 2 μm fiber lasers [95] and to study the impact of fiber boundaries on leaky modes [96]. Due to the high demand for this

diagnostic tools, a S^2 imaging measurement device has been commercially released using a tunable laser and a CCD to optimize cost and acquisition time [97].

3.2.2 Detailed experimental procedure

The typical S^2 imaging experiment is schematically represented in Figure 3-1. Since this technique is based on measuring spectral MMI, one of the key element is the use of a broadband source. There is not restriction on the light wavelength at which mode analysis can be performed as long as the wavelength range of the broadband source can be resolved by the OSA.

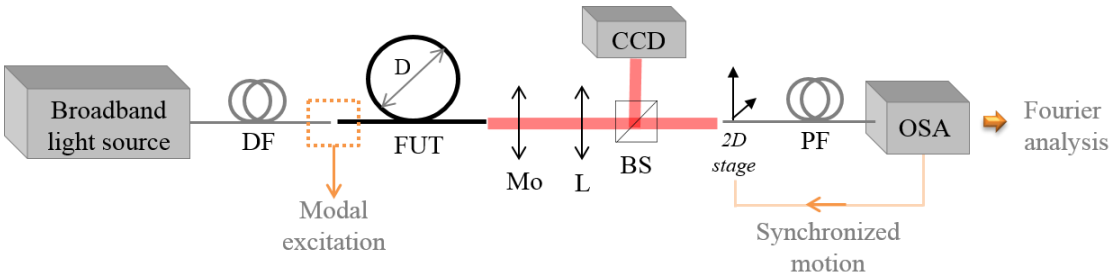

Figure 3-1: S^2 imaging experiment with DF: Delivery Fiber, FUT: Fiber Under Test; Mo: microscope objective aligned in a *4-f* imaging system with the lens L; BS: Beam Splitter; PF: Probe Fiber; OSA: Optical Spectrum Analyzer.

The light source is fiber-coupled in a delivery fiber (DF). The choice of the DF directly influences the performances of S^2 imaging and is further discussed in Section 3.3.3. In Section 2.4, we discussed in details the factor which can influence the light guided in an optical fiber. In practice, these can be controlled using the in-coupling alignment between the DF and the fiber under test (FUT) and the coil diameter (indicated by the letter D in Figure 3-1). The DF can either be fusion spliced or butt-coupled to the FUT. The respective core alignment will determine the modal excitation in the FUT. Another possibility would be to use a focusing lens to image the DF field in the FUT core. However the introduction of a lens might induce spatial aberrations in the incident

beam, directly influencing the mode overlap between the DF and the FUT and thus the mode combination excited in the FUT. The light emerging the FUT is imaged using two lenses aligned in a *4-f* imaging configuration. Using a 50/50 non-polarizing beam splitter (BS), the near-field is simultaneously imaged on the plane of a CCD and on the plane of a probe fiber (PF). On one side, the CCD allow to record an image of the FUT near-field in real-time i.e. when changing the in-coupling alignment. On the other hand, the PF, fixed on a motorized 2D stage, collects the signal from the near-field image with a spatial resolution equal to its core diameter. The S^2 imaging measurement is fully automatized using a Labview program to record transmission spectra at several locations across the entire near-field image. The duration of the measurement can vary from ~20 min to several hours depending on the size of the near-field image and the spatial and spectral resolution which are determined by the size of the steps during the PF motion (spatial resolution), and the wavelength range and the spectral resolution set on the OSA respectively.

The measured spectra are further analyzed employing a Fourier-based numerical code created to extract the individual modal properties including MP values, mode profile and phase distribution. The main steps leading to the modal evaluation are illustrated in Figure 3-2. A fiber beam made of 60% of LP_{01}, 30% of LP_{11} and 10% of LP_{21} was numerically created and is shown in Figure 3-2(a). The white grid indicates the locations of the PF where transmission spectra were recorded. First, the Fourier transform of each measured spectrum is calculated and then summed resulting in a total Fourier spectrum illustrated in Figure 3-2(b). Interfering modes appear at Fourier maxima located at the specific DGD defined by their effective index difference (Equation (28)). In Figure 3-2(b), three maxima where represented: at zero DGD which corresponds to the DC component of the measured spectra, at $\Delta\tau_1$ resulting from LP_{01} interfering with LP_{11} and at $\Delta\tau_2$ from LP_{01} and LP_{21} interfering.

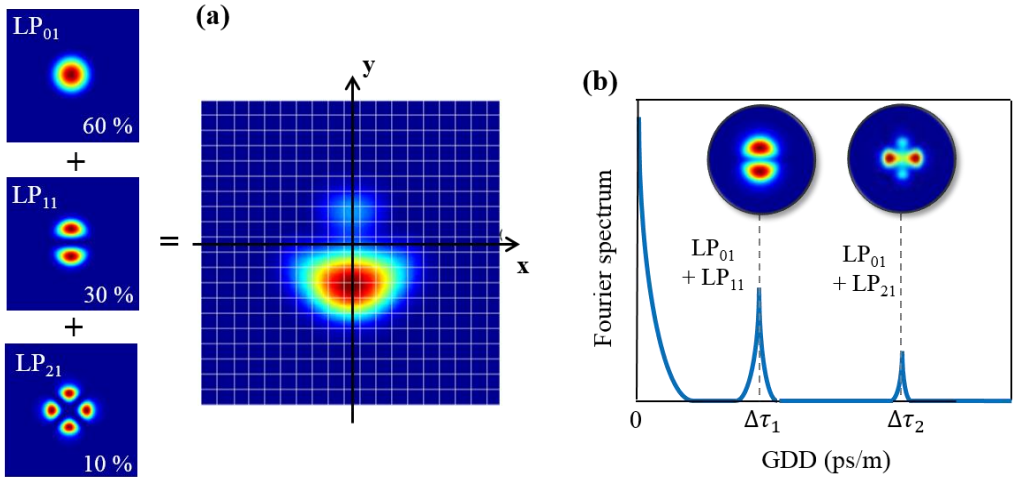

Figure 3-2: Schematic of the Fourier transform analysis performed after S^2 imaging. (a) Total field calculated assuming 60% of LP_{01}, 30% of LP_{11} and 10% of LP_{21}.The white grid indicate the locations covered by the PF to measure individual spectra. (b) Fourier spectra calculated from S^2 imaging measurements. Each maxima correspond to two modes interfering at a specific DGD $\Delta\tau_n$. The Fourier peak amplitude is used to evaluate MP values ρ_n^2 and to reconstruct the amplitude profile (calculation details are provided in Appendix B).

Since LP_{01} is dominant in this particular example (carrying 60% of the total power), the interference between LP_{11} and LP_{21} can be neglected. Individual modal properties are extracted from the Fourier maxima:

- The MP values ρ_n^2 are evaluated using the amplitude of the Fourier peak at the DGD where the HOM interfere with the FM.
- The mode amplitude is reconstructed after recording the Fourier amplitude of each measured spectrum at the fixed DGD ($\Delta\tau$ value indicated in Figure 3-2(b)). The profiles corresponding to the interference between 60% of LP_{01} with 30% of LP_{11} and 60% of LP_{01} with 10% of LP_{21} have been calculated to provide a visual example and are shown at $\Delta\tau_1$ and $\Delta\tau_2$ respectively (the value of the relative phase remained fixed). From this reconstruction the guided mode in the FUT can be identified. This is a considerable

advantage when investigating specialty fiber with complex core shapes or carrying different sets of modes (such as the ring PCF introduced in Section 1.3.

- The modal phase is measured by comparing the minima and maxima of the measured spectra at different locations across the near-field.

More details regarding the mode evaluation procedure can be found in the references [30] and [31]. In addition, a complete numerical model has been developed in parallel to the S^2 imaging experiment to evaluate the expected DGD resulting from two modes interfering and to reconstruct the total beam profile according the measured MP values and relative phases. To limit the length of this section, details on the analytical modeling of S^2 imaging can be found in Appendix B.

There are a few important experimental considerations to take into account when performing S^2 imaging mode analysis:

- The temporal scale of the Fourier spectra depends on the bandwidth and the spectral resolution used to record the MMI spectra. On the other hand, the period of the MMI depends on the length of FUT used for the measurement. The rule of thumb is that ~20 periods are necessary to calculate an accurate Fourier transform Thus, prior to S^2 imaging, a trade-off must be found so that ~20 MMI periods can be measured in a bandwidth < 40 nm.
- The choice of the PF determines the spatial resolution of S^2 imaging. The pixel size increases with the core size. However, using a smaller core size (~10 μm in diameter) limits the signal-to-noise ratio (SNR) measured on the OSA. On the other hand, increasing the core size not only increases the SNR but also leads to the apparition of HOMs which is incompatible with an accurate S^2 imaging measurement. Indeed, the MMI occurring in the PF will perturb the MMI measured in the FUT leading to incorrect mode analysis results. However, SIF with core sizes > 50 μm are characterized with a "flat" spectral response, averaged between the very high

number of guided modes. Thus, it is possible to use either small core SMF or > 50 μm core diameter SIF as PF depending on the SNR on the OSA.

- Also, it has been experimentally determined that recording 40x40 = 1600 pixels results in a minimum of 4 hours measurement duration. An option to reduce the acquisition time could be to employ a PF with large core step-index design. A second trade off must be found to ensure proper spatial resolution while ensuring a reasonable acquisition time.

As a result, the experimental conditions should be carefully selected prior to perform a series of S^2 imaging analysis in order to guarantee accurate and trustable modal decomposition

3.2.3 Discussion: current limitations

S^2 imaging can be performed without prior knowledge of the waveguide structure. There is also no restriction on the wavelength as long as the source and the OSA operates in the same spectral range. This mode analysis is particularly powerful to resolve weakly guided modes propagating in fibers attenuated up to ~40 dB which makes it particularly suitable to precisely evaluate the single-mode purity of a fiber beam (see Chapter 4).

However, in some particular cases listed blow, S^2 imaging does not provide accurate modal analysis results:

- Since this measurement is based on measuring MMI, degenerated modes cannot be resolved i.e. modes with the same propagation constant β.
- As the number of modes guided in a fiber increase, the complexity of the MMI pattern increases. An example is illustrated in Figure 3-3 where two typical transmission spectra measured after a MM fiber and a few-modes fiber are plotted

in (a) and (b) respectively. As a result of the MMI periodicity, the Fourier transform can become difficult to analyze.

- To date, the numerical routine to evaluate MP ρ_n^2 from S^2 imaging is based on the assumption that the FM is dominantly excited and result from the interference between two HOMs can be neglected. As a result, this mode analysis technique is in general restricted to few-modes fibers where small or no intermodal coupling occurs. However, the detection limit of S^2 imaging regarding the power distribution in the FM compared to the HOM is not clearly defined. The measurement accuracy in such cases is also not known. This "grey zone" of S2 imaging measurement has been recently addressed and results will be presented in details in Section 3.4.

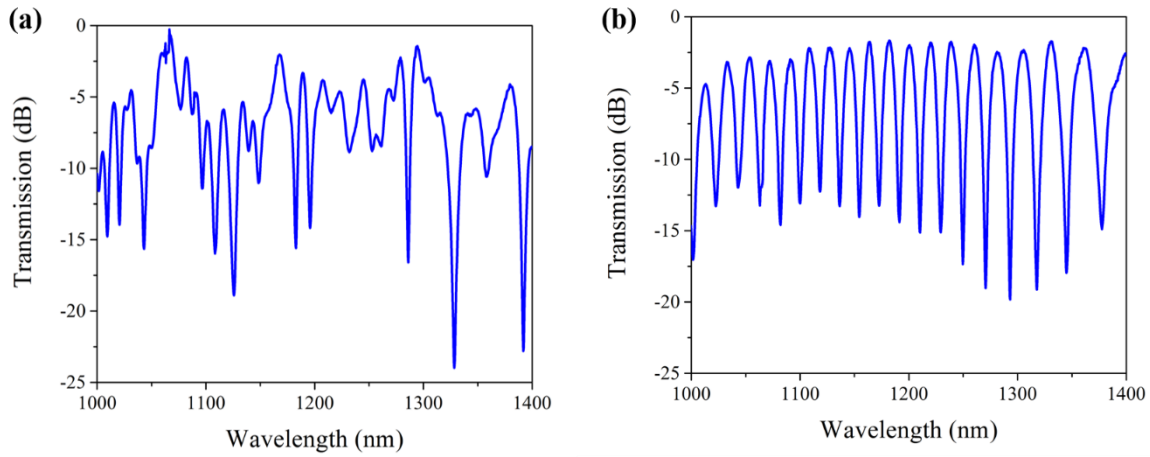

Figure 3-3: Spectral response measured at the output of (a) a MMF and (b) a few-modes fiber.

3.3 The correlation filter method (CFM)

3.3.1 Introduction and principle of operation

The CFM has been first introduced by Golub *et al*. [26] who first demonstrated transverse modes separation using spatial filters followed by Soifer *et al.* who succeeded using Computer Generated Holograms (CGH) [81]. The ability to use computer encoded filters was suggested by Lee et al. [98]. This approach has been used since then to fabricate CGH using laser lithography. Figure 3-4 shows a picture of a silicon wafer where GCHs were inscribed (the size of the hologram filters is ~0.5 cm in diameter). The two CGHs indicated in Figure 3-4 have been calculated to decompose the modes in a LMA-SIF (Section 3.4) and in a MCF (Sections 6.3 & 6.4).

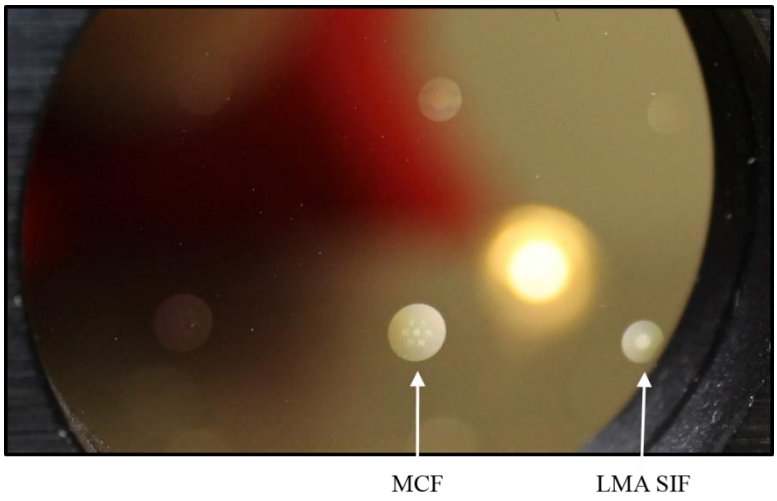

Figure 3-4: Picture of the CGH device. Two correlation filters are indicated fabricated to analyze a LMA step-index fiber (SIF) and MCF. This particular CGH was employed in the experiments presented in Section 3.4 and Section 6.3 & 6.4 respectively.

Using CGHs, the overlap integrals of the incident fiber near-field with the calculated modal transmission functions can be optically calculated. In addition, multiple channels (each one corresponding to a modal amplitude or relative modal phase) can be multiplexed in one filter using

different carrier frequencies. CGHs work in transmission and the diffracted light is analyzed in the Fourier plane using a CCD.

This technique has been employed to perform complete modal decomposition in amplitude, phase and polarization of LMA fibers [99] and MCFs [100]. Recently, it has been demonstrated that SLMs can be used as correlation filters, enabling real-time switching of the digital hologram [101]. To date, CFM has been used to measure mode-resolved bend-losses in few-modes fibers [102] and to characterize beams with orbital angular momentum [103]. Additional applications have been recently reported such as fast M^2 measurement [104], wavefront reconstruction [105], mode division multiplexing and de-multiplexing [106], [107] and characterization of fiber-to-fiber coupling [50].

3.3.2 Experimental realization

The classic experiment for CFM mode analysis is schematically represented in Figure 3-5. Compared to S^2 imaging, CFM is a narrow line-width measurement where correlation filters are designed for one wavelength. After exciting the mode content guided in the FUT, the near-field of the emerging beam profile is imaged on the CGH using a 4-f imaging scheme made of a microscope objective (Mo) and a lens. The magnification factor $m = f_L/f_{Mo}$ is carefully chosen to match the dimensions of the correlation filter. The diffracted far-field is then imaged on the CCD using a Fourier lens (L_F) and contains direct information including the MP and intermodal phase differences for each transverse mode.

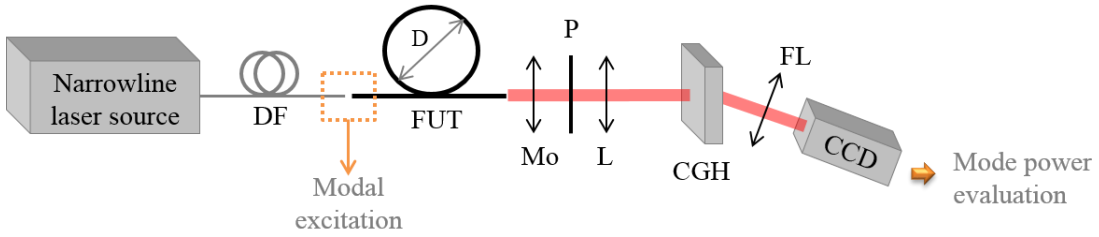

Figure 3-5: Typical CFM experiment with DF: Delivery Fiber, FUT: Fiber Under Test; Mo: microscope objective aligned in a 4-f imaging system with the lens L; P: Polarizer; CGH: Computer Generated Hologram; FL: Fourier Lens.

Results of numerical simulations are shown in Figure 3-6(a) and (b) to illustrate the decomposition of a single-mode and a multi-mode beam respectively using an amplitude encoded CGH. The far-field of the diffracted beam is recorded on the CCD using the Fourier lens (FL) The blue arrows in Figure 3-6 indicate the exact location of each mode correlation answer, each one corresponding to a specific CCD pixel. These locations were chosen when calculating the CGH. Individual mode coefficients (MP values ρ_n^2 and (or) intermodal phases ϕ_n^2) are recorded after measuring the intensity at the modal correlation answer. In Figure 3-6(a), results from the modal decomposition of the single-mode beam shown at the bottom left are plotted in a bar diagram indicating that the only non-zero correlation answer was recorded for LP_{01} resulting in $\rho^2(LP_{01})$ = 1. On the other hand, Figure 3-6(b) shows the results from the CFM analysis of the same multi-mode beam as the one previously used in Figure 3-2 for S^2 imaging. In this case, several non-zero correlation answers can be measured as shown in the bar diagram indicating $\rho^2(LP_{01})$ = 0.6, $\rho^2(LP_{11})$ = 0.3 and $\rho^2(LP_{21})$ = 0.1.

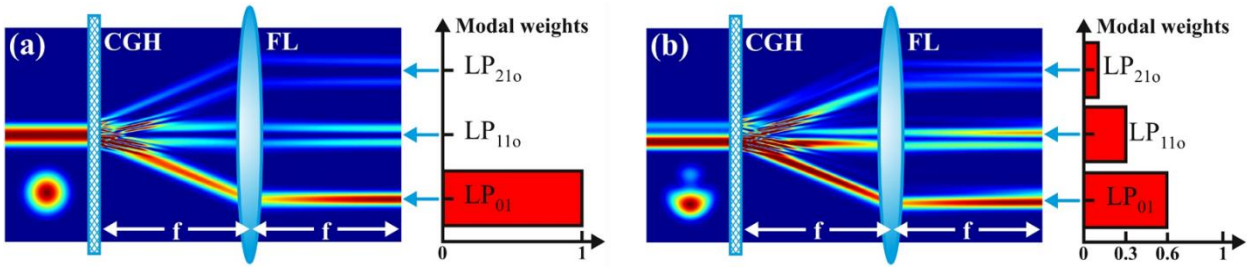

Figure 3-6: Simulated results of CFM mode decomposition of a single-mode beam (a) and a multi-mode beam made of 60% of LP_{01}, 30% of LP_{11} and 10% of LP_{21} (b). The total near field emerging the fiber is represented in the bottom left of the picture. This figure was created by Daniel Flamm.

3.3.3 Discussion: current limitations

CFM mode analysis is particularly suitable to provide a real-time decomposition of multi-mode beams and has been widely employed in various applications (Section 3.3.1). A linear polarizer can be used before the CGH to resolve polarization-degenerated beams. Along with the measurement of intermodal phase coefficients, vector-valued beams can be reconstructed and directly compared to the near-field emerging the optical fiber (using an additional BS and a CCD).

However, a specifications when employing CFM can be mentioned:

- The correlation filter is fiber-specific and wavelength-specific. As a result, one filter must be calculated and fabricated to investigate one fiber only at a particular wavelength resulting in a relatively expensive technique. However, this limitation has been overcame after proposing to use computer controlled SLM as correlation filters [101].
- Prior knowledge of the guided mode content is necessary to calculate well-matched correlation filters. The reliability and accuracy of the mode decomposition depends on the veracity of the waveguide dimensions and refractive indices. In the case of

complex waveguides, these parameters might be difficult to access imposing a limitation on using CFM in such cases.

- The resolution power of CFM when measuring low HOM contents is limited by the sensitivity of the CCD sensor at the measurement wavelength, by the ambient noise and depends on the number of channels encoded in a CGH. As a results, the lowest MP values accurately measured are on the order of a few percent.

3.4 Novel combined experiment for advanced mode analysis

Here, a novel experiment combining S^2 imaging with CFM is detailed in Section 3.4.2. These results were recently published [108], [109]. The goal was to develop an advanced tool for in-depth characterization of optical fibers, reported in details in Section 3.4.3. Using the mode decomposition results of fourteen different fiber beams with the combined experiment, the modal detection limit of each mode analysis technique has been experimentally determined for the first time, to the best of our knowledge. The modal decomposition results are presented and discussed in Section 3.4.4 followed by the conclusion on the modal capabilities of S^2 imaging and CFM.

3.4.1 Presentation of the fiber under test

The FUT used in this experiment is a standard step-index LMA fiber, labeled LMA20, commercialized by Fibercore with a core diameter of 20 μm, 125 μm cladding diameter and ~0.07 NA according to the manufacturer specifications. It has been selected to conduct the combined experiment study for several reasons: (a) it is a standard fiber design in which dimensions and indices can be accurately measured (easy CGH fabrication) (b) and it is a Few-Modes Fiber (FMF)

where 4 non-degenerated *LP* modes are supported in the core at λ = 1064 nm, offering the ability to excite different modal combinations by changing the in-coupling excitement and coil conditions while avoiding uncontrolled inter-modal coupling (see details in Section 2.4).

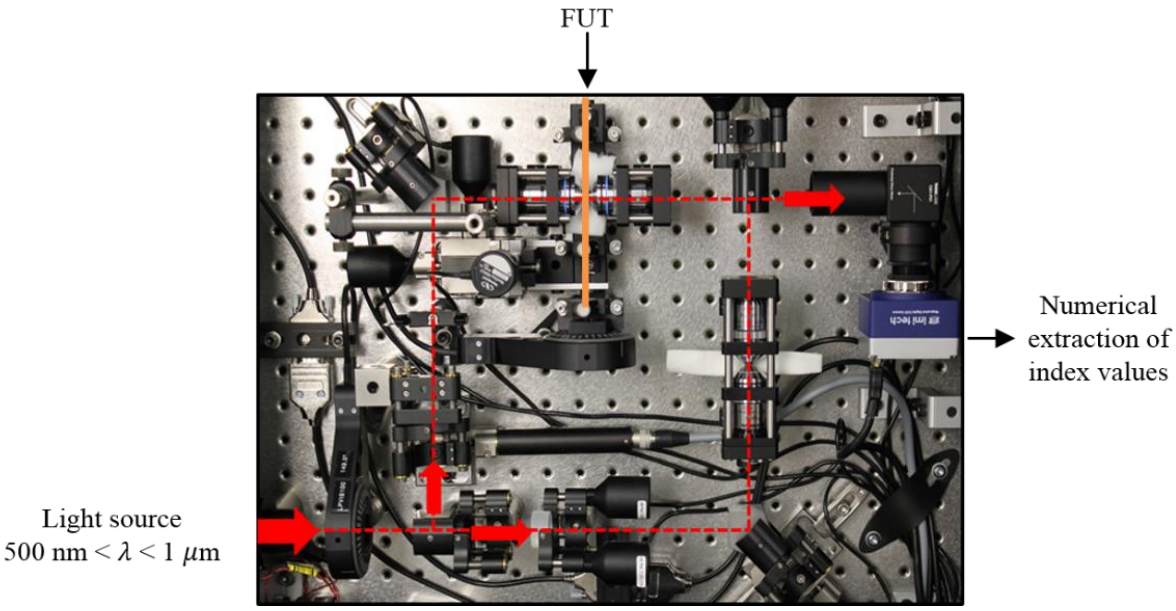

Figure 3-7: Profilometer measurement device (Interfiber Analysis) to measure the fiber refractive indices, dispersion and stress profile. The Fiber Under Test (FUT), indicated with the orange line, is located in one of the arm of the interferometer.

Accurate measurement of the refractive indices in an optical fiber has been possible since the introduction of a novel piece of equipment called profilometer [110]. A picture of this diagnostic is shown in Figure 3-7. Using an interferometric setup, the path length difference between each fiber layer and the surrounding index matching oil is recorded across 1D or 2D of the fiber facet. Values of the refractive index profile are extracted using a de-convolution algorithm at several wavelength ranging from 600 nm up to 1 μm. The fiber dispersion can be interpolated from the refractive index measurement using fitting functions such as the Sellmeier or the Cauchy equation [111]. In our applications, it is extremely useful to know the values of the refractive index

light wavelengths between 1 μm and 2 μm. Within this range, the Cauchy interpolation is known to be more accurate. Thus, the fitting function

$$n = A + \frac{B}{\lambda^2} + \frac{C}{\lambda^4} \qquad (42)$$

is used to measure n at the measurement wavelength with A, B and C the fitting parameters.

The 1D refractive index profile measured across the LMA20 is plotted as function of the fiber axial distance in Figure 3-8(a). The index values measured in the core and the cladding regions are plotted for different measurement wavelengths in Figure 3-8(b) along with the interpolated dispersion curve in the core and cladding layers in red and black respectively. According to the measured index values at λ = 1064 nm, the LMA20 fiber V-parameter is ~4.1 corresponding to four guided modes: LP_{01}, LP_{11}, LP_{21} and LP_{02}. Finally, the measured fiber indices and fiber dimensions are used in a mode solver to determine the propagation constants of the guided modes used to calculate and fabricate a perfectly matched CGH.

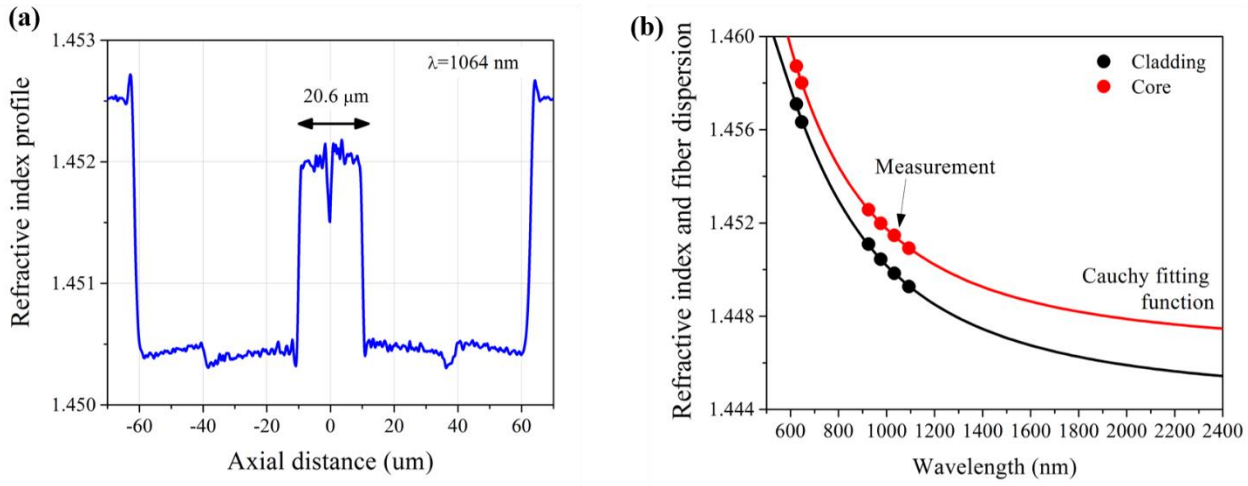

Figure 3-8: (a) Measured index profile of the LMA20 fiber at λ = 1064 nm showing distinctly the core and cladding regions. (b) Measured indices at several wavelength (plotted using round markers) and Cauchy-interpolated dispersion curves in the core (red) and cladding (black).

3.4.2 Combined experiment

The experiment combining S^2 imaging and CFM is schematically represented in Figure 3-9. Two sources with different bandwidth but emitting around the same wavelength are employed to satisfy S^2 imaging and CFM requirements: a 60 nm broadband superluminescent diode (SLD) and a narrow linewidth laser respectively. Both sources, linearly polarized, are coupled in the DF, a SMF with cut-off wavelength at λ = 780 nm. A second piece of DF is mounted on a translation stage allowing the user to manually switch between the light sources only by changing the DF-to-DF alignment.

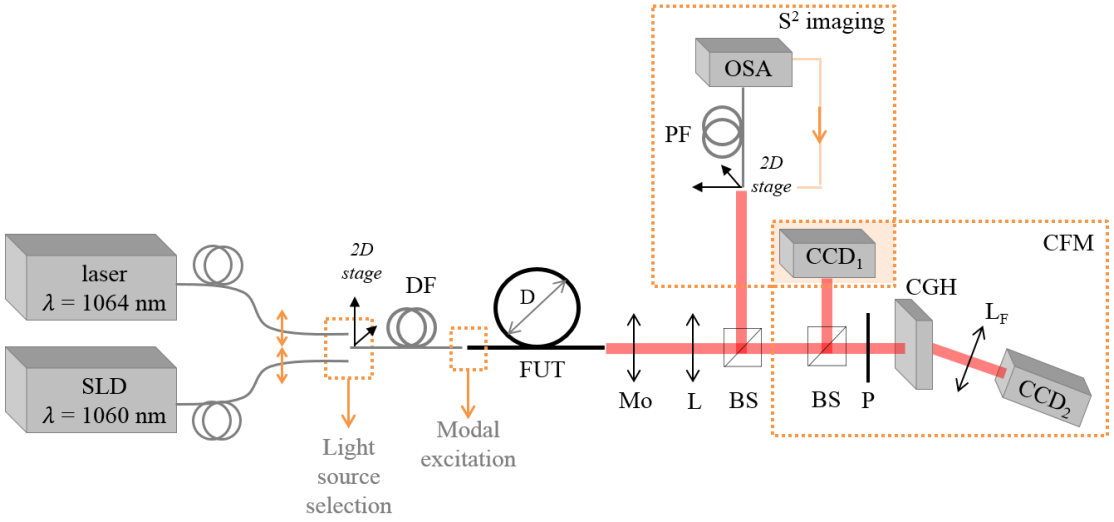

Figure 3-9: Experiment combining S^2 imaging and CFM mode analyses. DF: Delivery Fiber; FUT: Fiber Under Test; Mo: microscope objective; L: focusing lens; BS: non-polarizing 50/50 Beam Splitter; P: linear Polarizer; CGH: Computer Generated Hologram; L_F: Fourier lens; PF: Probe Fiber and OSA: Optical Spectrum Analyzer.

The source is then coupled into the FUT via the DF using a two-dimension translation stage to control the modal excitation in the LMA20. The near-field is imaged using a microscope objective (MO) aligned in a 4-f configuration with a lens (L). Two 50/50 beam splitters (BS) split and direct the beam on CCD_1 measuring the FUT near-field while the coupling/coiling conditions are

changed, on the probe fiber (PF) used for S^2 imaging mode analysis and on the CGH to perform CFM. The orange box around the CCD_1 indicate that it is the common detector between S^2 imaging and CFT and serves as near-field measurement reference.

To perform S^2 imaging, the SLD light source is coupled in the FUT via the DF. Real-time CFM analysis is performed using the laser source. A picture of the dual-light source module implemented at the front end of the combined experiment is presented in Figure 3-10. The narrow line-width laser is highlighted in green while the SLD is in red. The state-of-polarization of both sources is aligned along the horizontal axis (using a half-wave plate for the laser and the polarization maintaining of the SLD. Since the DF is not a PM fiber, coil-induced birefringence is achieved in the experiment to preserve the state of polarization of the light coupled in the FUT. Using the combined experiment presented in Figure 3-9, a the beam emerging the FUT can be decomposed with S^2 imaging and CFM without perturbing the in-coupling light alignment in the FUT and for fixed fiber coil.

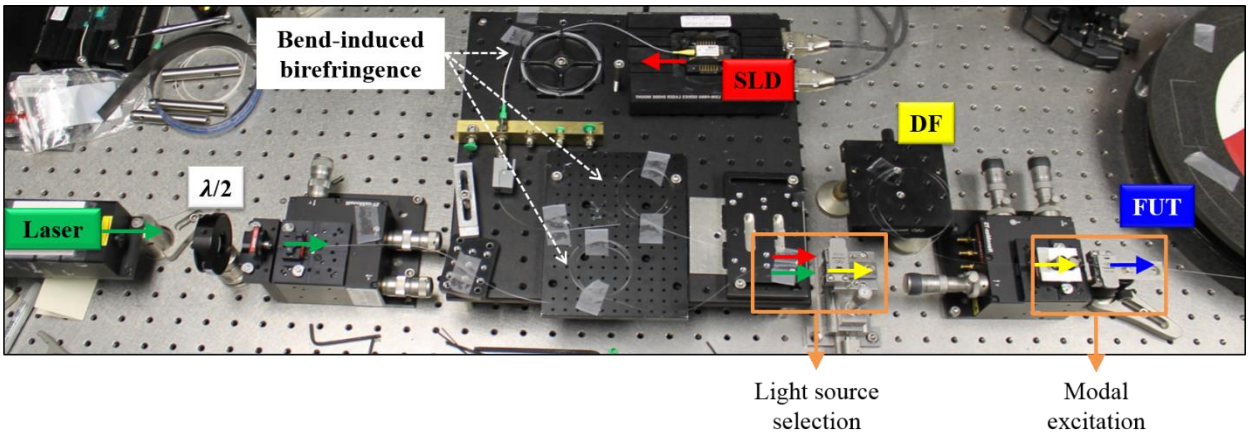

Figure 3-10: Dual light source module of the combined experiment used to control the modes content of the FUT (modal excitation box) and to select the light source depending on the mode analysis technique (light source excitation box). The laser is used for CFM and the SLD for S^2 imaging. Particular attention was paid to create and maintain a horizontally state of polarization.

3.4.3 Advanced capabilities for mode analysis using the combined experiment

In this paragraph, the procedure employed to analyze the LMA20 beams measured with the combined experiment is presented in details. The different steps are illustrated via two examples: a Quasi-Single-Mode (QSM) beam and a multi-mode beam. These two beams are obtained by changing the in-coupling DF-LMA20 alignment while monitoring the near-field on CCD_1. A Gaussian-like intensity profile corresponds to a QSM beam (achieved for centered alignment of the DF-LMA20 cores and coiling radius < 5 cm) while spatial distortions indicate the contribution of HOMs. Once a FUT beam is selected, the experimental conditions are fixed and a first CFM analysis is performed (duration is only a few seconds). Then, the light source is switched and S^2 imaging is performed on the same FUT beam for a total measurement duration of ~ 40 min. The combined experiment analysis in concluded by another CFM decomposition. After each FUT measurement and before further processing of the data, results from the two CFM analyses are compared and must show a perfect match.

The Fourier spectra calculated after performing S^2 imaging on the QSM and the multi-mode beams are plotted as function of the DGD in Figure 3-11 and Figure 3-12 respectively according to the standard procedure for data analysis described in [77]. The peak at zero DGD, called DC-component, contains the contribution from all excited mode propagating in the LMA20. In Figure 3-11(a), the QSM beam profile is shown and the corresponding Fourier spectrum, calculated and plotted in Figure 3-11(b), showed two discrete maxima at DGD = 0.12 ps/m and 0.26 ps/m. From the reconstructed modal amplitude, a residual amount of HOM LP_{11} guided in the LMA20 could be resolved. In comparison, the Fourier spectrum of the multi-mode beam (intensity profile shown in Figure 3-12(a)), plotted and represented in Figure 3-12(b), exhibits

several maxima. The modal amplitude and phase profiles have been reconstructed at two selected DGDs (0.35 ps/m and 0.56 ps/m) showing evidence of guided LP_{11} and LP_{21} modes.

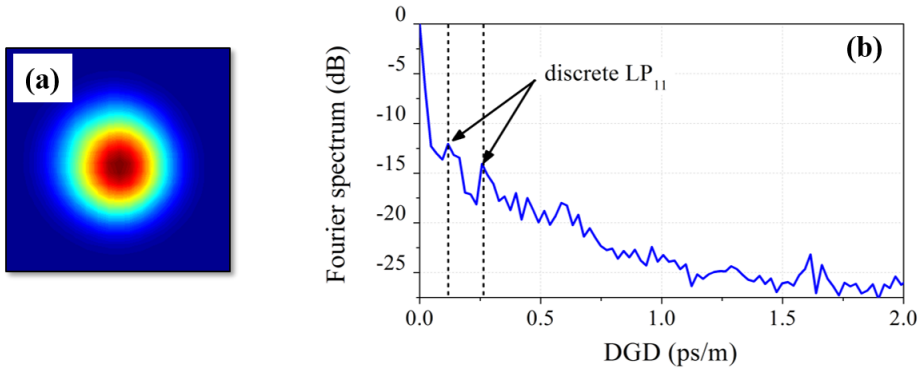

Figure 3-11: (a) Reconstructed near-field of the QSM beam. (b) Calculated Fourier spectra after S^2 imaging analysis. Two discrete DGD values, indicated with arrows, correspond to DGD where residual LP_{11} mode has been measured.

On the Fourier spectrum of the multi-mode beam in Figure 3-12(b), both sharp and broad maxima have been identified as guided HOMs. It has been already demonstrated [78] that broad Fourier maxima (red and blue areas in Figure 3-11(b)) are the result of distributed mode scattering along the fiber length and can be distinguished from discrete scattering (single peak indicated by the arrow). Distributed mode scattering is illustrated in Figure 3-12(c) where modal amplitudes have been reconstructed for several DGD values comprised in the LP_{11} grey area in Figure 3-12(b). As a result, S^2 imaging provided the powerful tool to determine whether the MP carried by HOMs is the result of (a) discrete HOM coupling at the DF/FUT interface or (b) distributed scattering along the fiber length. When evaluating ρ_n^2 values, both contributions (from discrete and distributed scattering) were considered (see Section 3.4.4).

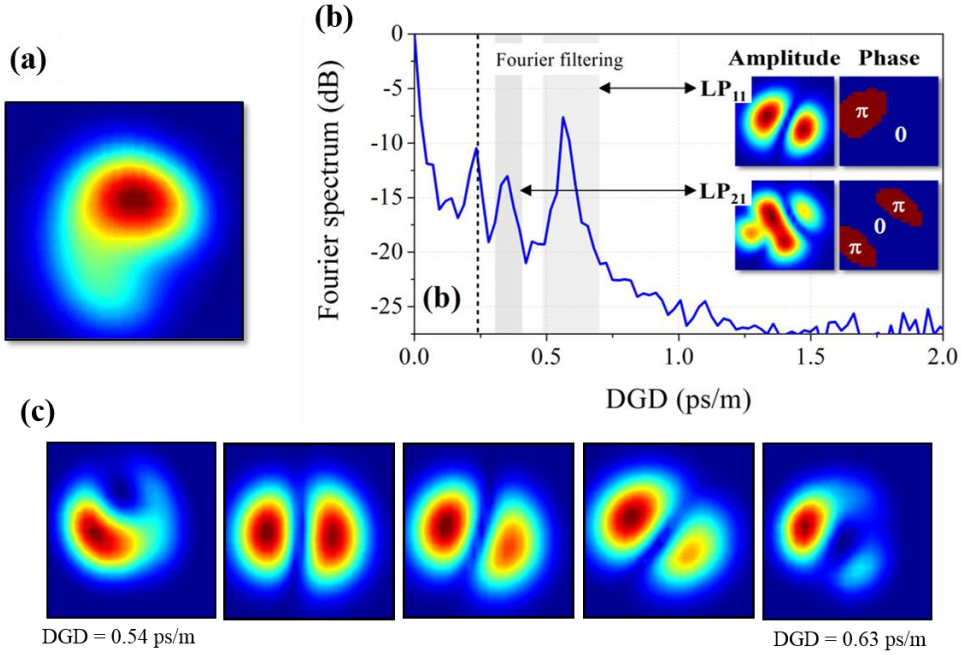

Figure 3-12: (a) Reconstructed near-field of the multi-mode beam and calculated Fourier spectrum (b). Discrete and distributed mode features are highlighted with a dotted line and shaded areas respectively. The amplitude and phase profile of the measured HOMs have been reconstructed at DGD = 0.35 ps/m and 0.56 ps/m corresponding to LP_{21} and LP_{11} respectively. (c) Amplitude profiles of the LP_{11} mode were reconstructed across the Fourier filter of LP_{11} (grey area in (b)) from 0.54 to 0.63 ps/m DGD values.

The CFM section of the combined experiment completes the scalar modal field analysis from S^2 imaging. The same QSM and multi-mode beams were decomposed using the CGH. The diffracted beam is imaged on CCD_2 and results are shown in Figure 3-13(a) and (b) respectively. The CGH has been calculated to analyze 6 amplitude channels (correlation answers denoted with white crosses in Figure 3-13) and 10 intermodal phase channels (intentionally not represented in Figure 3-13 for clarity purposes). All the channels are spatially separated using different values of carrier frequencies. As detailed in Section 3.3.2, the intensity recorded at each correlation answer, corresponding to selected pixels on CCD_2, is directly proportional to ρ_n^2 and ϕ_n^2 values. The diffracted QSM beam is shown in Figure 3-13(a). In this case, the intensity measured at each correlation function is zero except for the LP_{01} mode. On the other hand, the diffracted multi-mode

beam represented in Figure 3-13(b) shows a significantly different pattern where non-zero intensities can be measured at several correlation answers, indicating the presence of multiple HOMs. Along with the measurement of the intermodal phases, knowledge of individual MP was used to calculate the total vector-valued field for the QSM and multi-mode beams. Results are presented on top of Figure 3-13(a) and (b) respectively showing a very good agreement with the measurement recorded on CCD_1.

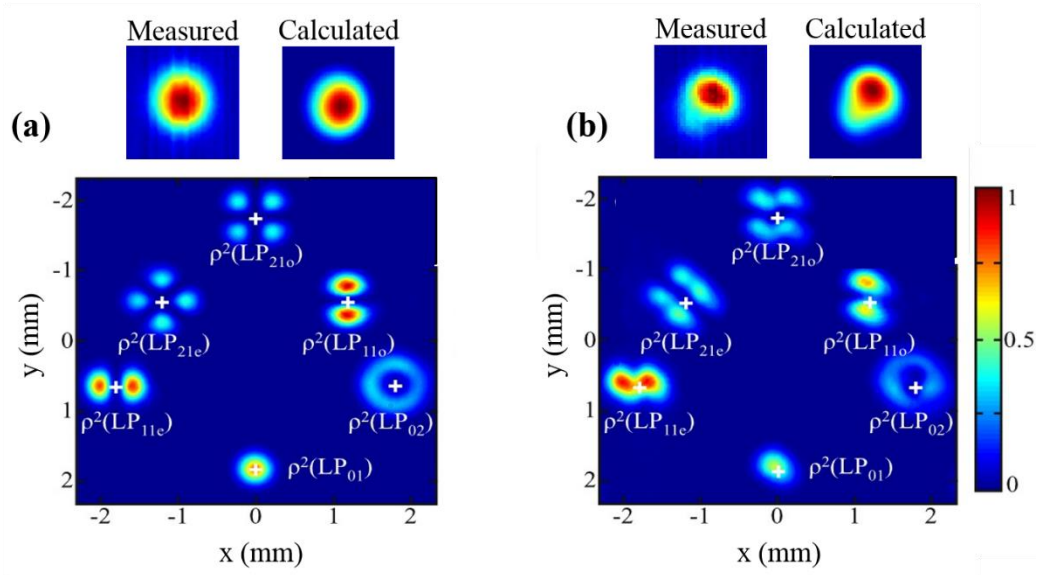

Figure 3-13: Diffraction patterns measured on CCD_2 of the QSM (a) and the multi-mode (b) beams. White crosses indicate the location of correlation answer for each mode of the FUT. The top inset displays the calculated vector-values FUT field compared to the measurement on CCD_1.

In summary, the unique combined experiment presented here benefits from the complementarity between S^2 imaging and CFM, enabling to perform an advanced characterization of optical fibers with access to individual scalar and vector-valued field components.

3.4.4 Mode Power evaluation

To date, S^2 imaging has been considered accurate when decomposing beams carrying one dominant mode. Recently, Nguyen *et al.* proposed a method to increase the accuracy of S^2 imaging when decomposing beams carrying more than two modes by identifying so-called spurious modes in the Fourier spectrum [112]. Most interestingly, Otto *et al* numerically demonstrated that the accuracy of the MP evaluation with S^2 imaging can be considerably improved employing general analytical mode evaluation algorithms [113]. In this paragraph, we experimentally investigate the limits of the S^2 analysis when decomposing several different beams.

3.4.4.1 Decomposition of a wide variety of beams using CFT

Fourteen different mode combinations have been excited in the LMA20 and decomposed using the combined experiment. For each beam, the normalized ρ_n^2 values were first evaluated with CFM and results are presented in the bar diagram in Figure 3-14 where the measured beams are sorted from smaller to larger HOM content. The same FUT beams have been decomposed with S^2 imaging and results are presented and compared in the next Section 3.4.4.2. For 2-fold polarization degenerated HOMs, both polarization contributions measured with CFM e.g. $LP_{11,e}$, $LP_{11,o}$ and $LP_{21,e}$, $LP_{21,o}$ were considered in the calculation of the MP values. In Figure 3-14, each LP mode is represented with a different color. For clarity purposes, four regimes, labeled from I to IV, were distinguished, corresponding to different mode mixtures. Regime I includes quasi-SM beams defined by $\rho^2(LP_{01}) \geq 95\%$. Regime II refers to beams carrying some HOM content but in which the FM still dominates such that $0.95 \geq \rho^2(LP_{01}) \geq 0.7$. Regime III comprises MM beams where $0.7 \geq \rho^2(LP_{01}) \geq 0.3$ and finally, regime IV contains beams where the LP_{11} mode is dominant

(corresponding to measurement 14). For each regime is indicated in Figure 3-14, a typical LMA20 near-field profile is represented on the right hand side. One can clearly observe the beam distortions as the HOM content increases.

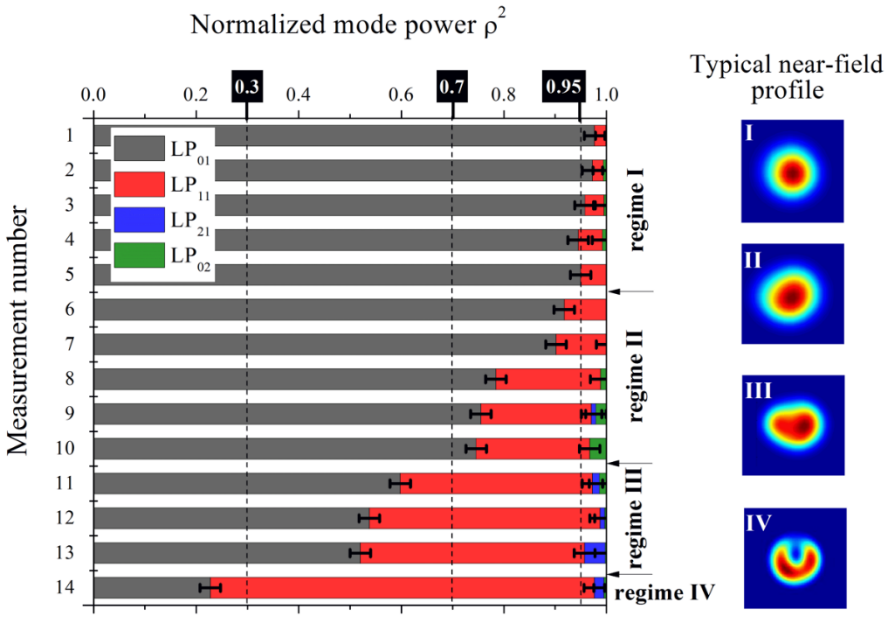

Figure 3-14: CFT mode decomposition of fourteen selected FUT beams. Measurements are sorted from low to high HOM content and each color represents a guided LP mode. The fixed measurement error of $\pm 2\%$ is shown on the plot. Typical FUT beams are depicted on the right-hand for each modal regime.

The accuracy of CFM mode evaluation mainly relies on the sensitivity of the CCD detector at the wavelength of measurement. In the present case, CCD_2 exhibits low quantum efficiency at λ = 1064 nm and certain weakly guided modes vanish in the background noise of the detector. Since the highest mode purity of the FM was measured around 98%, the resolution of CFM in the evaluation of the MP ρ_n^2 is fixed at $\pm$ 2% regardless of the modal regime. Corresponding error bars are indicated in Figure 3-14.

3.4.4.2 Direct comparison between MP evaluated using S^2 imaging and CFM

Results of the MPs evaluated in all fourteenLMA20 beams and reported in Figure 3-14 have been also evaluated using S^2 imaging measurements. To the best of our knowledge, this is the first time S^2 imaging has been performed to decompose a wide variety of QSM and MM beams with the ability to directly compare the MP results with a different mode analysis technique. This paragraph focuses on determining the influence of the evaluation procedure on the measured values of ρ^2 and furthermore determine the most suitable approach according to the type of beam decomposed.

Two distinct analytical methods suggested in [113] have been applied to evaluate ρ_n^2. and the corresponding calculation details can be found in Appendix B. The first MP evaluation, called method 1 (Appendix B), relies on the strict assumption that most of the power is carried by one dominant mode. As a result, the value of $\rho^2(LP_{01})$ is approximately equal to the amplitude of the Fourier DC-component. This approach has been the general evaluation method employed in most S^2 imaging measurements and applications listed in Section 3.2.1. The MP values obtained using method 1 are represented in Figure 3-15 using hollow circle markers. A second evaluation method, called method 2 (Appendix B), is an analytical expression defined from the general expression of n-interfering modes. This approach is particularly suitable when the power is distributed among several HOMs. ρ_n^2 values obtained using method 2 are represented using plain diamond markers in Figure 3-15.

Figure 3-15 summarizes the values of ρ_n^2 evaluated using method 1 and method 2 for each modal regime previously defined in Section 3.4.4.1 (regime I to IV corresponding to Figure 3-15(a) to (d)). For clarity purposes, the y-axis of each plot has been scaled separately. Guided modes are

represented with different colors: LP_{01} in black, LP_{11} in red and LP_{21} in blue. The ρ_n^2 values previously evaluated from CFM (Figure 3-14) are represented using square markers and they offer a direct comparison with the S^2 imaging evaluation results.

In regime I, the approximation of one dominant mode applies and calculated values for $\rho^2(LP_{01})$ and $\rho^2(LP_{11})$ using method 1 and 2 (circle and diamond markers) perfectly overlaps. It is noteworthy that HOM powers as low as $\rho^2(LP_{11}) \approx 0.006$ can be calculated from S^2 imaging measurements whereas, in this range, CFM only detects noise. This is also illustrated when evaluating $\rho^2(LP_{21})$ (blue lines in Figure 3-15(b)).

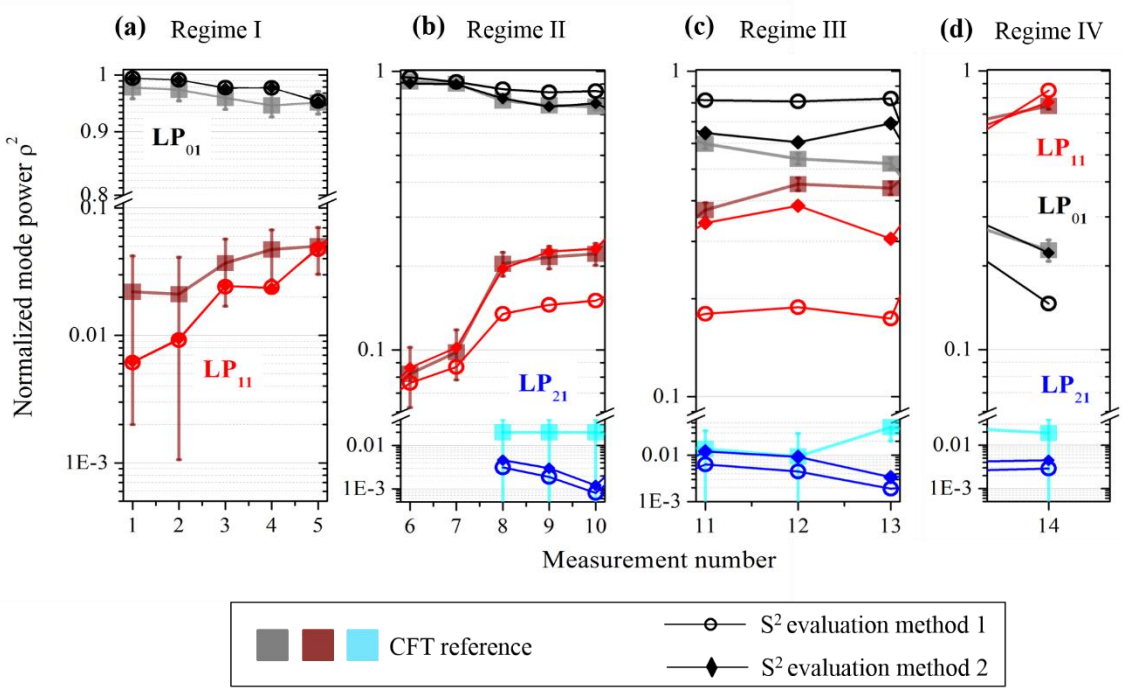

Figure 3-15: Modal decomposition of fourteen FUT beams measured with the combined experiment (a) to (d). Normalized MP values ρ_n^2 are evaluated from CFT (squares) and from S^2 imaging employing methods 1 (circle) and 2 (diamonds) [39] for individual guided modes.

In regime II (Figure 3-15(b)), MP values evaluated with methods 1 and 2 differ. However, $\rho^2(LP_{01})$ and $\rho^2(LP_{11})$ calculated with method 2 (diamonds) show a very good match with the

CFM evaluation (squares). In this regime, the strict approximation of a dominant mode does not apply and the values obtained using method 1are inaccurate.

Reaching regime III (Figure 3-15(c)), $\rho^2(LP_{01})$ and $\rho^2(LP_{11})$ evaluated with method 2 differ from CFT results as the HOM mixtures increase (in particular for measurement 12 and 13). In this regime, mode identification is difficult due to the complexity of the Fourier spectrum.

Finally, regime IV (Figure 3-15(d)) is similar to regime II except that LP_{11} carries most of the power. Evaluation results of $\rho^2(LP_{01})$ and $\rho^2(LP_{11})$ using method 2 are in agreement with CFM. In addition, S^2 imaging evaluation of low HOM content ($\rho^2(LP_{21})$) provides an unmatched accuracy regardless of the method employed.

3.4.4.3 Identification of the working range of S^2 imaging

Finally, the accuracy of S^2 imaging mode evaluation has been quantified by considering $\rho^2(LP_{11})$ values obtained for measurements 5 to 13. For these measurements, MP results from CFM can be considered as accurate ($\rho^2(LP_{11}) \geq 0.04$) and will be used as a reference. The relative difference between S^2 imaging results employing methods 1 and 2 and CFM has been calculated using the relation

$$1 - \frac{\rho^2\left(LP_{11}(S^2)\right)}{\rho^2\left(LP_{11}(CFM)\right)}. \qquad (43)$$

Results are plotted as function of the HOM MPs evaluated from CFM (the reference) and represented in Figure 3-16 for both evaluation methods. Experimentally, the relative difference between method 1 and CFM was founds to be less than a few percent for $\rho^2(LP_{11})$ values below 0.1. For HOMs carrying a higher amount of light (measurement 8 to 13), the relative difference of method 1 to CFM considerably increases indicating that the evaluation method of S^2 imaging is

not accurate. In comparison, it is clear that, when evaluating $\rho^2(LP_{11})$ with method 2, the relative difference to CFT is less than a few percent up to $\rho^2(LP_{11}) \approx 0.3$ which considerably increases the modal detection limit of S^2 imaging. For larger mode mixing, S^2 imaging evaluation fails due to the complexity of the Fourier analysis.

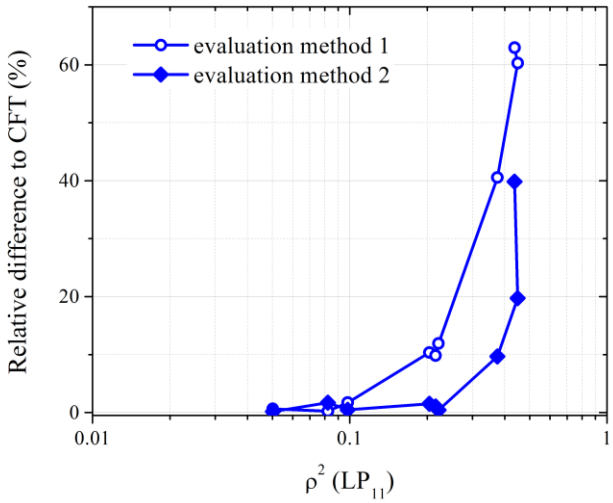

Figure 3-16: Relative difference evaluated using Equation (43) between ρ_n^2 evaluated using methods 1 and 2, both compared to CFM values presented in Figure 3-14. Data points correspond to measurements 5 to 13 and show an increased S^2 imaging accuracy when using method 2.

3.5 Summary and outlook

A novel experimental tool for mode analysis has been proposed combining, for the first time of our knowledge, two different and widely used mode analysis techniques. In addition to provide an advanced modal decomposition of optical fibers (with access to scalar and vector-valued fields), the combined experiment offers the unique capability to simultaneously decompose one beam using CFM and S^2 imaging. The direct comparison between ρ_n^2 values evaluated from CFM analysis and S^2 imaging has led to experimentally confirm that S^2 imaging modal evaluation accuracy is considerably improved when employing a generalized analytical numerical routine

(method 2 Appendix B [113]). To the best of our knowledge, this is the first demonstration that S^2 imaging can be used to accurately decompose beams where the FM carries as low as 70% of the guided light. A complete summary of the expertise of each mode analysis technique is presented in Table 3. The main differences between S^2 imaging and CFM are highlighted as well as the strengths and current limitations determined from the combined experiment results. Some challenges currently remain when evaluating highly MM beams (measurement 12 and 13) with S^2 imaging due to the complexity of the Fourier spectrum analysis. In this regime, CFM analysis provides unmatched mode decomposition capabilities.

Table 3: Comparison between mode analysis techniques.

	S^2 imaging	**CFM**
Relying on a prior knowledge of internal fiber parameters	No	Yes
Underlying mode analysis principle	Spatially and spectrally resolved MMI	Spatial correlation by means of a holographic filter
Necessary spectral linewidth	Broadband source (few tens of nm) [77] Narrow-line width tunable laser source [97]	Narrow line-width source (< 1 nm)
Measurement and computation time	Few minutes to few hours (*)	0.03 s(**)
Real-time capability	No	Yes
Detection and distinction between degenerated modes	No	Yes
Reconstruction of guided modes amplitude and phase profiles	Yes	No
Distinction between discrete and distributed mode scattering with unambiguous localization	Yes	No (FUT is treated as a black box)
MPs (ρ_n^2) evaluation	Indirect (analytical method 1 or 2 [113])	Direct intensity measurement
Upper HOM detection limit	Up to $\rho^2 \approx 0.3$ using method 2 [113]	$\rho^2 \approx 0.98$(**)
Lower HOM detection limit	$\rho^2 \approx 0.006$(***)	$\rho^2 \approx 0.02$(**)
Limitations	- Complex mode identification when measuring MM beams - Tailored fiber length and source bandwidth	Measurement accuracy depends on number of detected modes

(*) considerably reduced when using a tunable laser source
(**) with the employed camera and wavelength
(***) in this particular FUT

CHAPTER 4: IN-DEPTH CHARCACTERIZATION OF LIGHT PROPERTIES IN SPECIALTY FIBERS

This chapter introduces three different specialty Large-Mode Area (LMA) fibers, all made of high-purity Fused Silica glass but for which the inner design has been finely tuned to achieve single-mode operation. Using the S^2 imaging mode analysis technique detailed in Chapter 3, the properties of light during propagation in a LMA Step-Index Fiber (SIF), a LMA Photonic Crystal Fiber (PCF) and a LMA Leakage Channel Fiber (LCF) were measured. In the following Sections 4.1 and 4.2, results from of the in-depth characterization of these specialty fibers will be presented in details. In Section 4.1, the single-modedness of the beam delivered by the LCF design is studied across a broad wavelength range (1 μm to 2 μm). The results from a comparative study of the single-mode performances between different fiber designs at 2 μm light wavelength are detailed in Section 4.2. This section is concluded with a discussion on the suitability of each fiber design to perform in a pre-specified field of application is concluding this chapter. The results detailed in this Section have been published in the literature [22].

4.1 Low-loss, broadband and single-mode propagation in leakage channel fiber (LCF) design

LCF specialty designs belong to the category of micro-structured LMA fibers and have been introduced for the first time in 2005 by Wong *et al.* [37]. Compared to conventional LMA SIF, in which the light is confined in the core due to the TIR at the continuous core/cladding

interface, the “broken” core/cladding boundary of LCFs makes these waveguides leaky for all modes. Engineering the microscopic features of LCFs enables to control the properties of the guided light by creating large modal discrimination between the FM and HOMs resulting in low-loss propagation of the FM whereas HOMs are leaky in the LCF cladding [114][115]. LCF are resonant waveguides due to their intrinsic design, in which conditions for inter-modal coupling can be achieved [116]. The all-solid structure of LCFs presents several advantages over comparable air-cladding PCF designs resulting in easy, reliable and mechanically stable tapering and splicing procedure without risk of environmental contamination.

LMA LCF offering scaled core sizes have been designed towards power scalability applications of fiber lasers and have been successfully implemented in high-power fiber laser systems [117]. Compared to highly bend-sensitive LMA PCF rods and Large-Pitch Fiber (LPF) designs currently employed in the development of high power fiber laser systems [20], [21], [38], [118]–[120], LCFs offer an attractive alternative featuring enhanced flexibility and compactness. Also, in comparison to holey structures, requiring special handling and splicing equipment, LCF-based systems have the potential to be monolithically integrated using standard cleaving and splicing equipment.

The development of high power fiber laser sources has become a challenge with the apparition of modal instabilities [121], resulting in uncontrolled spatial beam distortions and unstable laser operation. Mode instabilities are a consequence of the formation of thermal gratings in the active core of the LMA fibers under high pumping levels [122], [123]. Several methods have been proposed in order to extend the mode instability threshold and mitigate their impact [124] such as extrinsic approach employing an acousto-optic deflector [124] and intrinsic methods involving a modification of the fiber design, in this case the use of a multi-core LMA PCF [125]

or with distributed mode filtering fibers [126]. In addition, a particular type of LCF designs called all-solid Photonic Band-Gap fibers (PBG) have been reported as one of the most promising alternative to enable further power scaling while maintaining stable and good-beam quality laser beams [88], [127]. However, to apply for these applications, LCF designs must deliver high purity single-mode beams. This property has been investigated in details and results are discussed in Section 4.1.2.

4.1.1 Preliminary characterization of the LCF

The LCF prototype presented here has been designed and fabricated by Nufern Inc. An image of the cross section of the LCF has been recorded with a microscope and is shown in Figure 4-1(a). The micro-structured cladding layer contains Fluorine-doped rods (dark regions) which are periodically arranged in a solid Fused Silica matrix (light gray). The F-doped rods are made of a lower refractive index than the surrounding silica matrix. When designing LCF, several parameters can be modified including the diameter of the F-doped rods, the spacing between rods (defined as the fiber pitch Λ), the number of rings of F-dopded and the number of F-doped rocs missing on the fiber center which forms the core.

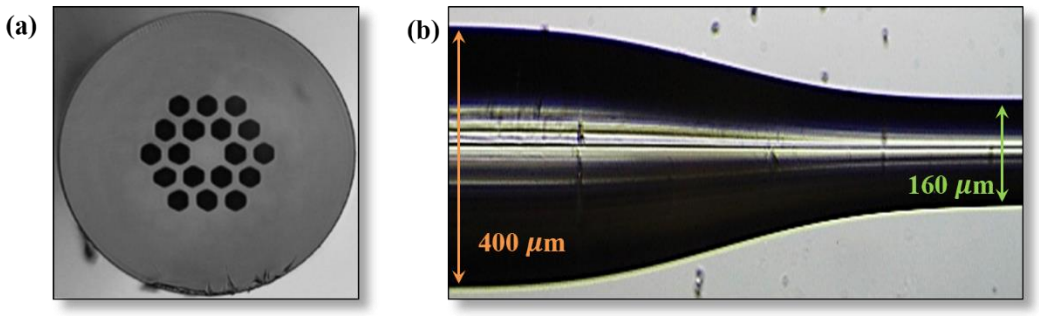

Figure 4-1: Microscope images of: (a) The LCF cross section showing periodic arrangement of F-doped rods and (b) a LCF taper made using standard fusion splicing equipment (GPX-3000 by Vytran Corp.) to reduce the LCF OD from 400 μm to 160 μm.

The LCF dimensions have been measured and values are summarized in Table 4. This prototype was made of a single cladding structure with outer diameter (OD) of 400 μm and a core diameter of ~50 μm offering a total available core area on the order of $\sim 2000 \mu m^2$. Each F-doped rods is 28 μm in diameter separated by a 38 μm pitch.

Table 4: Measured dimensions of the LCF. The measurement error is ± 0.5 μm

Core diameter	49.1 μm
Cladding diameter	400 μm
F-doped rods diameter	27.8 μm
d/Λ	0.74

Furthermore, the refractive indices of the LCF have been measured using the profilometer described in Section 3.4.1. The fiber OD was reduced from 400 μm to under 200 μm, maximum size supported by the profilometer. A picture of the LCF taper, made using standard fusion splicing equipment (GPX-3000 by Vytran Corp.), is shown in Figure 4-1(b). It illustrates the advantage offered by solid fiber designs compared to holey fiber designs to be manipulated with standard equipment and integrated in all-fiber systems. Results of the 2D refractive index profile of the tapered LCF measured at 633 nm wavelength are shown in Figure 4-2(a) where each color indicate a different index value e.g. F-doped rods appear in blue. The 2D refractive index profile highlights structural features which are in accordance with the record LCF facet in Figure 4-1(a). The 1D refractive index profile across the fiber facet was measured with the profilometer using several light wavelength ranging from 600 nm up to 1 μm. It is important to note that the accuracy of 1D index measurement decreases as the number of microstructures in the fiber increase. The 2D measurement and 1D measurement of the LCF indices at the same light wavelength of 633 nm show a good agreement which proves the accuracy of the 1D index measurements in this micro-structured fiber design. The measured refractive indices of the fused silica matrix and of the F-

doped robes in the LCF are plotted for several wavelength and results are indicated in Figure 4-2(b) using black and red markers respectively. The lines in Figure 4-2(b) represent the LCF dispersion interpolated from the index measurement following the procedure described in Section 3.4.1.

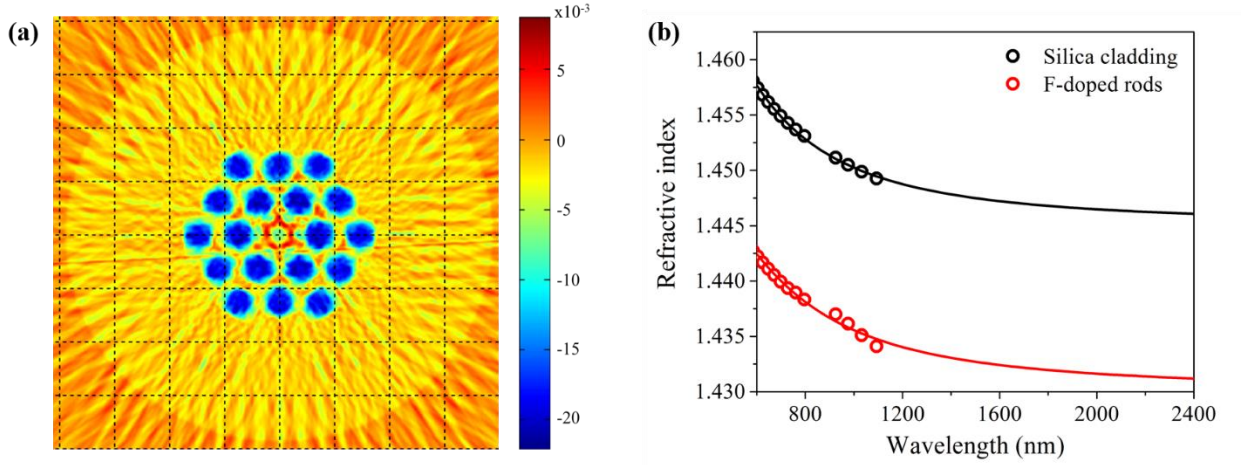

Figure 4-2: (a) 2D measurement of the LCF refractive index profile at 625 nm light wavelength. Different colors stand for different index values. (b) Measured refractive index of the fused silica matrix and the F-doped rods, extracted from 1D measurements, at several wavelength (black and red markers respectively). The dispersion in each medium was interpolated and is plotted with a line.

The LCF dimension and index values have been used in a mode solver (Fimmwave by PhotonDesign) to calculate the expected guided modes. Calculations were performed for light wavelength comprised between λ = 800 nm to λ = 2.4 μm using the measured fiber dimensions and indices values. Results are presented in Figure 4-3 where the difference between the mode effective index and the cladding effective index, labeled Δn, is plotted as function of light wavelength. A positive value of Δn indicates a guided mode in the LCF core. Two modes propagating with the same value of Δn are degenerated. According to the results shown in Figure 4-3, two non-degenerated guided modes are expected to be guided in the LCF, i.e. LP_{01} and LP_{11} plotted in black and red respectively while the HOMs LP_{21} and LP_{02}, are leaky in the LCF cladding.

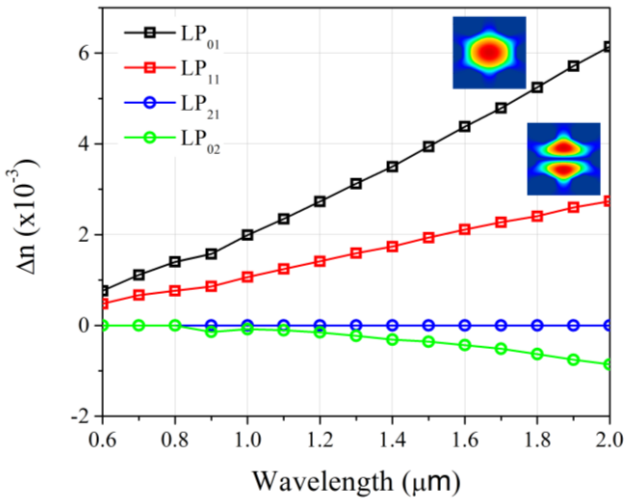

Figure 4-3: Calculated difference between mode effective index and LCF cladding index for four first *LP* modes as function of wavelength (commercial software package from PhotonDesign).

To complete the LCF characterization, the transmission of a supercontinuum white light source ($400 < \lambda < 2.4$ μm), has been measured after propagating 10 meters in the fiber core. Results are presented in Figure 4-4(a) where the resulting attenuation was plotted across a broad wavelength range. An interesting results is that several light wavelengths are guided in the LCF with an attenuation of 1dB/m or less. This is the case for typical lasing wavelength 1.06 μm, 1.55 μm and 2 μm indicated in Figure 4-4(a) with black, red and green lines respectively. In addition, the near field of the beam emerging the LCF around 1 μm has been recorded using a CCD and is shown in Figure 4-4(b). Even though numerical simulations (Figure 4-3) predict that LP_{11} is guided in the LCF at this wavelength, the spatial beam uniformity measured in Figure 4-4(b) does not allow to predict any HOM content. As a result, in-depth characterization of this fiber design has been performed using S^2 imaging in order to determine the accurate guided mode content in the LCF.

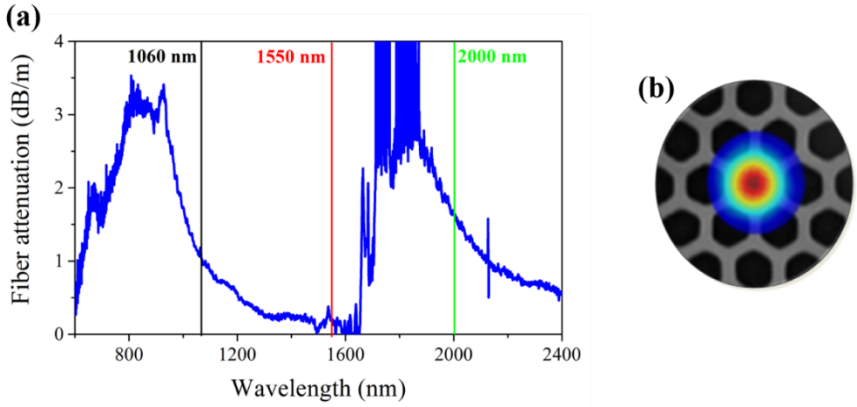

Figure 4-4: (a) Measured broadband attenuation in the LCF. (b) Measured near-field profile of the beam emerging the LCF at a wavelength of 1 μm (represented on top of the LCF structure for visual aid).

4.1.2 Measured guided transverse modes from 1 μm to 2 μm wavelength

4.1.2.1 Results from S^2 imaging analysis

The mode content guided in the LCF has been measured using the S^2 imaging technique. This choice was motivated by the ability to perform S^2 imaging using broadband light source without restriction on the wavelength as long as it matched with the detection range of the OSA. For example, if CFM would be used to decompose the mode content, one correlation filter for each measured wavelength would have to be designed and fabricated resulting in a costly operation. In addition, the modes LP_{01} and LP_{11} guided in the LCF (Figure 4-3) are non-degenerated which is well suited to perform S^2 imaging analysis. The same S^2 imaging experiment presented in Section 3.2.2 was used to investigate the LCF. Three broadband, fiber-coupled light sources emitting around 1.06 μm, 1.55 μm and 2 μm wavelength respectively have been used to excite the modes in a 10 m long piece of the LCF resented in Section 4.1.1. The DF (SM980 with single-mode cut-off at λ = 980 nm) and the LCF were fusion spliced using a standard Ericsson fusion splicer in

order to ensure a good and stable in-coupling alignment stability over the duration of the measurement. To limit the effect of external perturbations on the mode content, the fiber is coiled with a loose diameter (> 60 cm) and stands flat on the optical table. The Fourier spectra extracted from the S^2 imaging analyses are plotted at the three selected wavelengths and results are shown in Figure 4-5(a). At each measured wavelength, a single DGD peak is measured resulting from the interference between two modes guided in the LCF core. The DGD values differ for different wavelength which is in agreement with the DGD definition in Equation (28).

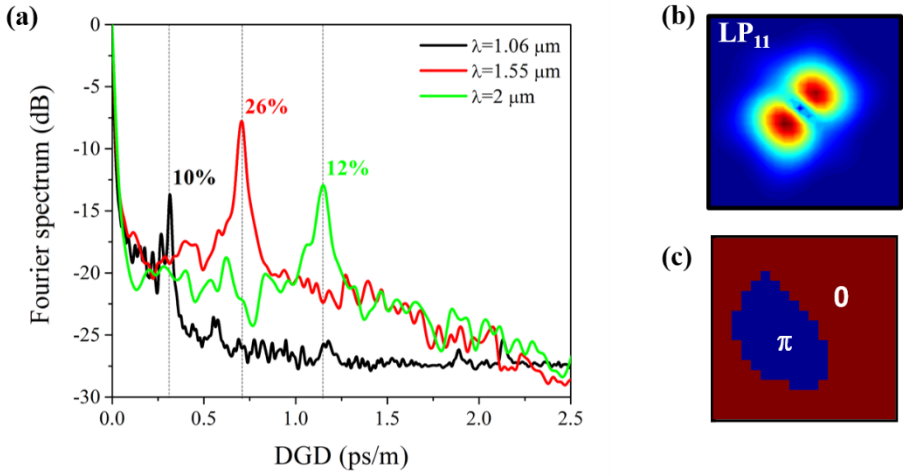

Figure 4-5: (a) Fourier spectra calculated from S^2 imaging measurements of the LCF at light wavelength of 1.06 μm, 1.55 μm and 2 μm in black, red and blue respectively. The HOM LP_{11} was identified after reconstructing the intensity (b) and phase profile (c) of the mode interfering at the DGD values indicated with the grey lines.

The intensity and phase distributions of the interfering mode have been reconstructed at the Fourier maxima (Figure 4-5(b) and (c) respectively) clearly indicating that LP_{11} is guided in the LCF and interfere with LP_{01} during propagation. $\rho^2(LP_{11})$ values were evaluated using the general analytical method described in Section 3.4.4.2 (corresponding to method 2 defined in Appendix B). Results are shown in Figure 4-5(a) indicating that $\rho^2(LP_{11})$ = 26% at the light wavelength λ = 1.55 μm. On the other hand, $\rho^2(LP_{11}) \approx$ 10% for λ = 1.06 μm and 2 μm. As a

result, the numerical predictions presented in Section 4.1.1 were experimentally verified after decomposing two guided modes in the LCF design from 1μm to 2 μm.

4.1.2.2 Coil-induced HOM suppression

In this section, S^2 imaging analyses were performed for various LCF coiling radii in order to determine if the HOM could be efficiently suppressed (by cladding mode coupling), leading to single-mode propagation. Results are displayed in Figure 4-6(a) where $\rho^2(LP_{11})$ is plotted as function of the LCF coiling radii. This study has been performed using 1.06 μm light wavelength, 1.55 μm and 2 μm corresponding to black, red and green markers respectively. The corresponding near-field profile of the beam emerging the LCF has been reconstructed and results are shown in Figure 4-6(b), (c) and (d) respectively for coiling radii > 30 cm.

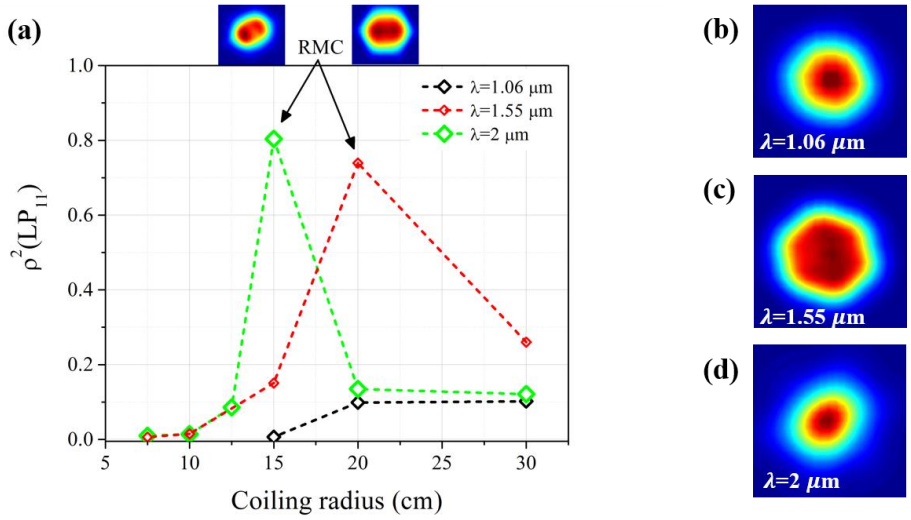

Figure 4-6: (a) Measured $\rho^2(LP_{11})$ in the LCF as function of coiling radius for the three wavelength investigated. Coiling conditions corresponding to resonant mode coupling (RMC) are indicated along with the corresponding intensity profile. The near-field intensity profiles emerging the fiber at each studied wavelength have been reconstructed under larger coiling condition (R=30 cm).

In comparison to the light propagating at 1.06 μm and 2 μm, measured with Gaussian-like intensity profile (confirmed by the MP values in Figure 4-5(a) on the order of 10%), the beam at 1.55 μm light wavelength was distorted (consistent with $\rho^2(LP_{11})$ = 26% calculated in Figure 4-5(a)). As the coiling radius is reduced, the mode LP_{11} was gradually suppressed. The values of the limit coiling radius to achieve efficient suppression of the HOM, labeled R_{lim} and defined by Equation (40), are summarized in Table 5. As expected, the value of R_{lim} depends on the light wavelength. Under specific coiling conditions, a sharp increase of $\rho^2(LP_{11})$ was measured. This phenomenon corresponds to resonant-mode coupling (RMC) between LP_{01} and $LP_{11}$where the power transfers from LP_{01} into LP_{11}, resulting in a dominant HOM. This effect has been previously observed in LCF designs [116]. The corresponding near-field profile reconstructed and show in inset of Figure 4-6(a) confirm the presence of a dominant HOM.

Table 5: Measured values of LCF radii to ensure coil-induced single-mode operation (R_{lim}) and resonant-mode coupling (R_{RMC})

Wavelength (μm)	**R_{lim} (cm)**	**R_{RMC} (cm)**
1.06	~ 15	-
1.55	~ 10	~ 20
2	~ 10	~ 15

4.1.2.3 Coil-induced losses in the FM

Pure single-mode operation can be achieved in LCF under controlled coiling conditions. In this section, the coil-induced losses in LP_{01} have been evaluated for different coiling conditions. To do so, $\rho^2(LP_{01})$ was calculated and bend-induced losses, labeled α_{Bend}, were calculated using

$$\alpha_{Bend} = 10 \times log\left(\frac{\rho^2|_{R_{lim}}}{\rho^2|_{R=30\ cm}}\right) \quad (44)$$

where the value of $\rho^2(LP_{01})$ at R=30 cm is considered as the straight fiber reference. These values are summarized in Table 6 at R_{lim} ensuring single-mode beam delivery. Moreover, the overall losses α suffered by LP_{01} while propagating in 10 m of LCF were calculated by adding the fiber attenuation (labeled α_{Att}) previously shown in Figure 4-4(a) with bend-induced losses following

$$\alpha = \alpha_{Att} + \alpha_{Bend}. \quad (45)$$

The overall loss values calculated under single-mode operation of the LCF, defined by R_{lim}, are summarized in Table 6.

Table 6: Losses of LP_{01} when propagating in the LCF including attenuation and bend-induced losses which are provided at R_c, coiling condition determined from the mode analysis results in Figure 4-6(a)

Wavelength (μm)	**Measured α_{Att} (dB/m)**	**Measured α_{Bend} (dB/m)**	**Measured α (dB/m) in the FM**
1.06	1.07	0.24	1.31
1.55	0.18	0.9	1.08
2.00	1.67	0.06	1.73

The overall loss experiences by LP_{01} have been plotted as function of the coiling radii and are shown in Figure 4-7. Plain markers indicate the conditions for single-mode operation, i.e. for $R<R_{lim}$,. In summary, coiling the LCF has a limited influence on the FM losses (variable α in Table 6) while the HOM LP_{11} is efficiently suppressed by cladding-mode. This results emphasizes the significant mode discrimination achieved in LCF structures as HOM can be efficiently suppressed while maintaining a low-loss guidance of the FM

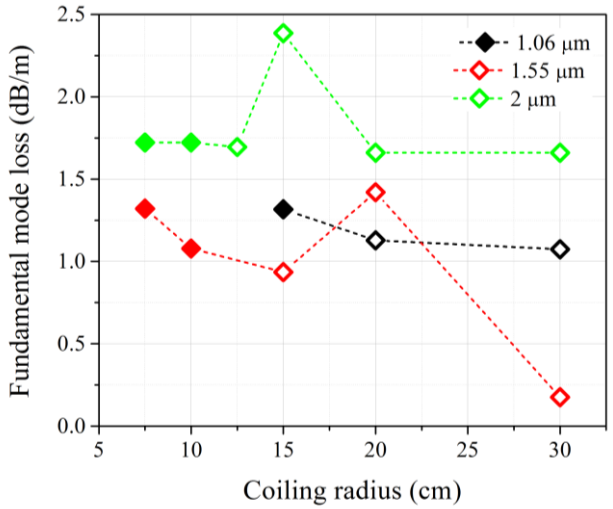

Figure 4-7: Overall losses suffered by LP_{01} after propagation in 10 m of coiled LCF for light at three different wavelengths. These values were calculated from the mode analysis experiments. Plain markers indicate conditions of single-mode propagation.

4.1.3 LCF broadband performances summary

Single-mode operation of the LCF was achieved for light wavelengths in the range of 1 μm to 2 μm under proper coiling conditions. Even though both simulations and experiments demonstrated that the core of this fiber supported two guided modes (LP_{01} and LP_{11}), the design-induced large modal discrimination enabled to efficiently suppress LP_{11} while maintaining reasonably low loss level in LP_{11} with α < 2 dB/m measured for the three wavelengths of interest. Considering laser and amplifier systems, which usually employ active fibers of a few meters long, as well as the high doping levels achieved in active fibers, the overall loses α could be easily compensated by the high gain factors achieved during light amplification.

In addition, these results are the first demonstration of the broadband single-modedness offered by LCF design [22]. Endlessy single-mode operation has already been measured in micro-structured PCF [9]. This novel property of LCF designs could become a serious advantage during

large-scale manufacturing of laser systems where only one fiber design could be used to generate continuous single-mode laser emission between 1μm and 2 μm wavelengths.

4.2 Comparative study of single-mode propagation between different large-mode area (LMA) fiber designs for 2 μm applications

The recent interest in light sources emitting in the 2 μm wavelength range has been mainly motivated by the large number and wide range of applications which could benefit from using light at an eye-safe wavelength. Most popular applications include directed energy and long range atmospheric propagation, spectroscopy, LIDAR, medical surgery as well as pumping of mid-IR light sources [128]–[132]. To date, thulium(Tm)-doped optical fibers seems to be the preferred gain medium to generate high power and high efficiency laser light around 2 μm [133].

During the development of 2 μm fiber lasers emitting high power performances, special attention was maintain good beam qualities. To do so, several Tm-doped LMA fibers were designed for applications around 2 μm light wavelength, such as Step-Index Fibers (SIF) [134], Photonic-Crystal Fibers (PCF) [135], [136], and large-pitch fibers [120]. However, it is common for extreme LMA fiber design to guide a small amount of weakly guided HOMs. Under high pumping levels, the HOM may significantly contribute to the laser emission, resulting in unstable laser performances and distorted beam profiles. As a result, performing a high-accuracy mode analysis in LMA specialty fiber designs would help to guarantee stable laser performance, power scalability and diffraction-limited beam quality.

In this section, the performances of three different LMA fibers designed for 2 μm applications are compared. After presenting the selected fibers in details in Section 4.2.1, the

expected guided mode content at 2 μm has been calculated in order to predict the fiber performances. Section 4.2.2 presents the results for the guided mode content measured at 2 μm with the S^2 imaging technique for each of the selected LMA fibers designs. The influence of the coupling conditions and the coiling diameters on the fibers were measured and compared. Finally, in Section 4.2.3, the respective ability of each LMA fiber design to deliver ultra-pure single-mode beams is discussed, including the measured mode-field area. A conclusion on the measurements is given in Section 4.2.4. The results detailed in the rest of this section have been published in the literature [137]–[139].

4.2.1 Selected LMA fiber designs

The selected LMA fiber are all passive designs primarily designed for power scaling applications of laser and amplifier systems emitting diffraction limited beam quality at wavelengths around 2 μm. A microscope image of each LMA fiber sample is shown in Figure 4-8. The first sample (Figure 4-8(a)) is a polarization maintaining SIF design with 25 μm diameter core, 400 μm diameter cladding, and ~0.08 numerical aperture (NA). This fiber has been fabricated by Nufern Inc. and similar designs using Tm-doped core have been successfully implemented in 2 μm high power monolithic fiber laser [8,17]. The LMA SIF design is directly compared to a PM PCF made by NKT Photonics A/S with a 50 μm diameter core, ~0.06 NA surrounded by a periodic array of air-holes and a pump cladding of 250 μm diameter. Several studies have been reported using a Tm-doped version of this LMA PCF design in cw and Q-switched laser cavities [9,18]. The third design is the LCF previously presented in Section 4.1. Even though the selected LCF has not been

specifically designed for 2 µm applications, promising performances at this wavelength have been recently reported [20]. A summary of the manufacturer-specifications can be found in Table 7.

Table 7: Selected LMA fiber design specifications

	SI LMA	PCF LMA	LCF LMA
Core/cladding diameter (µm)	25/400	50/250/550	50/440
Core NA	0.08	0.06	0.07
Fiber length (m)	3.1	2.3	9.0
MFD (calculated at 2 µm)	24	35	42

To calculate the guided modes, the refractive indices and dispersion curves for each LMA fiber have been extracted at 2 μm after being measured with a profilometer (introduced in details in Section 3.4.1). Fiber dimensions and indices were used in a FEM mode solver to calculate the guided modes. From the mode list, the Mode-Field Diameters (MFD) of the FM LP_{01} have been calculated and results are also given in Table 7.

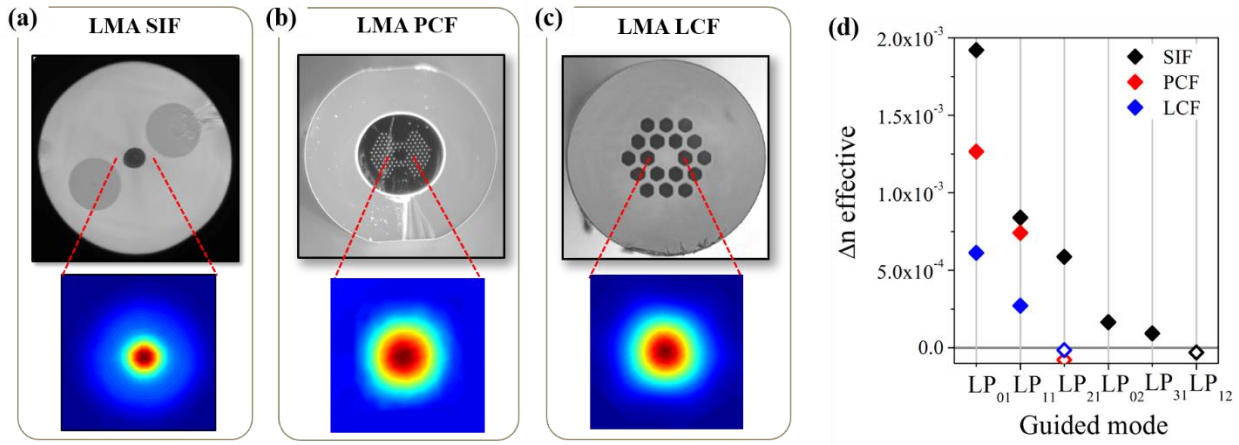

Figure 4-8: Microscope images of the facets of the LMA SIF (a) PCF (b) and LCF (c) with the corresponding emerging beam profiles imaged measured at 2 μm on a CCD. (d) Results from calculation at 2 μm of the difference between the guided modes effective index and the cladding index for the first LP modes in black, red and blue respectively. Empty markers indicate cladding modes.

More results of the mode solver calculations are plotted in Figure 4-8(d), showing the effective Δn, the effective difference between modes and cladding indices for the first LP modes

calculated with the mode solver. A positive Δn value indicates a core mode whereas a negative Δn corresponds to a cladding mode. As a result, five modes (LP_{01}, LP_{11}, LP_{21}, LP_{02} and LP_{31}) can be supported in the core of the SIF while only LP_{01} and LP_{11} are expected to be guided in the core of the PCF and LCF.

4.2.2 Mode analysis performed at 2 μm

Light emitted by a 2 μm ASE source fiber coupled in a SMF for delivery was used to excite the guided modes in these LMA fibers. After optimizing the SMF-to-LMA free space coupling alignment, the LMA fibers were loosely coiled on a plane surface to prevent any external perturbation of the guided light. After propagating through a given length of fiber (provided in Table 7), the emerging beam profile is imaged onto a CCD. The recorded profiles are shown in Figure 4-8(a), (b) and (c) for the SIF, PCF and LCF designs, respectively. Each profile shows a smooth and uniform Gaussian-like spatial distribution.

To investigate the fields emerging from the LMA fibers (Figure 4-8(a), (b) and (c)) in greater detail, S^2 imaging mode analysis has been performed to decompose the total fields into individual transverse modes [21]. The experimental setup is directly inspired from the original S^2 imaging experiment detailed in Section 3.2. The measurement was performed using light from a broadband Tm-doped fiber-coupled ASE source emitting between 1.92 and 1.96 μm. The DF was mounted on a 3-axis stage and is butt-coupled to the LMA fiber under investigation. Using the z-axis of the stage, the mode-field matching between the delivery SMF and the LMA fiber was adjusted to minimize coupling losses. Furthermore, the x and y-axis of the stage allow a precise control of the overlap between the SMF beam and the core of the LMA fiber.

4.2.2.1 Effect of in-coupling alignment on modal content

Due to the significant dimension mismatch between LMA fibers and conventional fiber components, most LMA-based fiber lasers are assembled in cavity architectures using free-space optics. In such cases, imaging schemes are designed using specific lens combinations to optimize the coupling efficiency in the core of the LMA fibers. In addition, it is well known from the general waveguide theory that the mode combination excited in an optical fiber depends on the overlap between the incident field and the allowed guided modes. For example, for a centered alignment between the core of the SMF and the LMA, the power will be only coupled in circularly symmetric modes labeled $LP_{0,n}$.

In order to evaluate the effect of light coupling on mode excitation and propagation, the mode content in the three LMA fibers was measured for two coupling conditions while maintaining the fibers unperturbed (coil diameter > 60 cm). The measurement was initiated by finding the central alignment position. To do so, the in-coupling SMF position is adjusted with respect to the LMA fiber core by adjusting the x and y-axis of the stage while observing the near-field on the CCD. Once the imaged beam exhibited a Gaussian-like profile, the lateral stage axis was translated by 2 μm to create an intentional in-coupling offset. Results are presented in Figure 4-9 for the LMA SIF. S^2 imaging was performed and the corresponding Fourier spectra were plotted as function of the DGD. Results are shown in Figure 4-9(a) for centered excitation and 2 μm offset alignment (black and green curve respectively). The measured near-field profiles under each coupling alignment are shown in inset (top and bottom of Figure 4-9(a) respectively). In the Fourier spectrum, the DGD values corresponding to HOMs interfering with the FM are indicated using arrows. For centered in-coupling alignment, $\rho^2(LP_{01})$ = 73% while $\rho^2(LP_{02})$ = 20%

(corresponding MPI = -7 dB) and some residual amount of power was coupled in LP_{11}. In comparison, four HOMs could be resolved after creating a 2 μm offset of the in-coupling alignment.

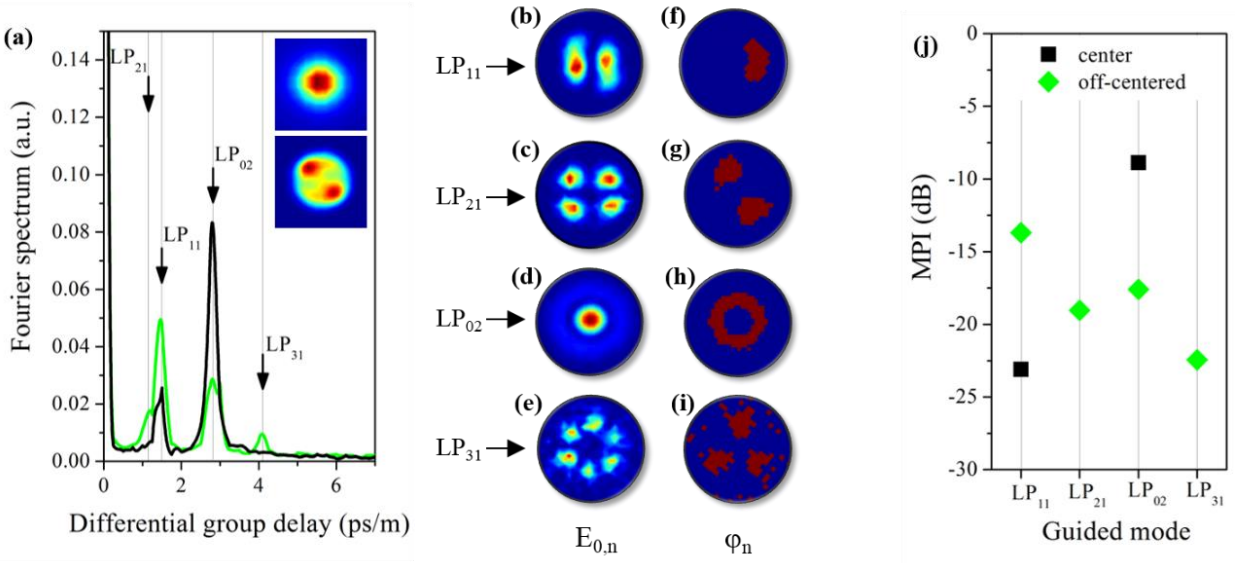

Figure 4-9: (a) S^2 imaging Fourier spectra of the LMA SIF measured at 2 μm for two different in-coupling alignments: centered (black) and 2 μm lateral offset (green). The intensity of each corresponding beam emerging the SIF, measured on a CCD, are shown in inset. The measured guided HOM content is indicated with arrows. From (b) to (e), the modal amplitude $E_{0,n}$ and from (f) to (i) phase φn have been reconstructed for the measured LP_{11}, LP_{21}, LP_{02} and LP_{31} guided HOMs. The MPI values are plotted in (j) for centered and offset excitation in black and green respectively.

From the S^2 imaging analysis, the guided mode amplitude ($E_{0,n}$) and phase (φ_n) profiles have been reconstructed and results are presented in Figure 4-9(b-e) and (f-i), respectively. The HOMs LP_{11}, LP_{21}, LP_{02} and LP_{31} were identified indicating a total of five modes, including the FM, propagating in the LMA SIF. These results show a good agreement with the mode solver results shown in Figure 4-8(d). The MP distribution has been calculated using the evaluation method 2 detailed in Appendix B. Here, the Multi-Path Interference (MPI) values were plotted for each guided mode in Figure 4-9(j) according to the definition $MPI = 10 \times \log(\rho_n^2)$. Results for

the center (black) and off-center (green) alignments are provided. These measurements confirm that a small in-coupling offset alignment in the LMA fiber directly influences the combination of modes excited and propagating. As a result, lasing performances in terms of stability, efficiency and beam profile can be directly impacted.

This in-coupling alignment investigation was repeated with the LMA PCF and LCF. From the mode analysis results, only the HOM LP_{11} could be measured with S^2 imaging which is again in agreement with the mode solver predictions. The measured MPI values are summarized in Table 8.

Table 8: MPI values (in dB) of LP_{11} content measured by S^2 imaging analyses

Lateral offset	**PCF LMA**	**LCF LMA**
0 μm	-18.4	-13.2
2 μm	-16.1	-11.7

As for the SIF, even at center excitation, considerable amount of power was carried by LP_{11} with 1.4% in the PCF (-18.4 dB) and 4.7% in the LCF (-13.2 dB), which can be attributed to imperfections in the launching conditions and finite mode coupling during propagation. In the off-center excitation, the overlap between the incident beam and the HOM increases resulting in a small increase of the MPI value of LP_{11}.

4.2.2.2 Coiling-induced HOM suppression

In order to suppress the residual HOM content, fiber coiling was used to coupled HOMs to leaky cladding modes [51], [52]. Here, the guided mode contents have been measured while changing the coiling diameter under fixed coupling alignment fixed to the center position. The Fourier spectra after S^2 imaging analysis of the LMA SIF, PCF, and LCF are presented in Figure

4-10(a), (b), and (c), respectively. In Figure 4-10(a), after coiling the LMA SIF down to 10 cm, the LP_{02}mode was strongly attenuated while LP_{11} was still guided. This can be explained by an energy transferred from LP_{02} to cladding modes while a small amount of power was still coupled to LP_{11} during propagation. On the other hand, it was found that the PCF design could not be coiled with diameters smaller than 40 cm without inducing significant propagation losses resulting in signal-to-noise ratio too low to perform relevant S^2 imaging analyses. From the Fourier spectra in Figure 4-10(b), the initially guided HOM LP_{11} experiences losses as the fiber is coiled tighter.

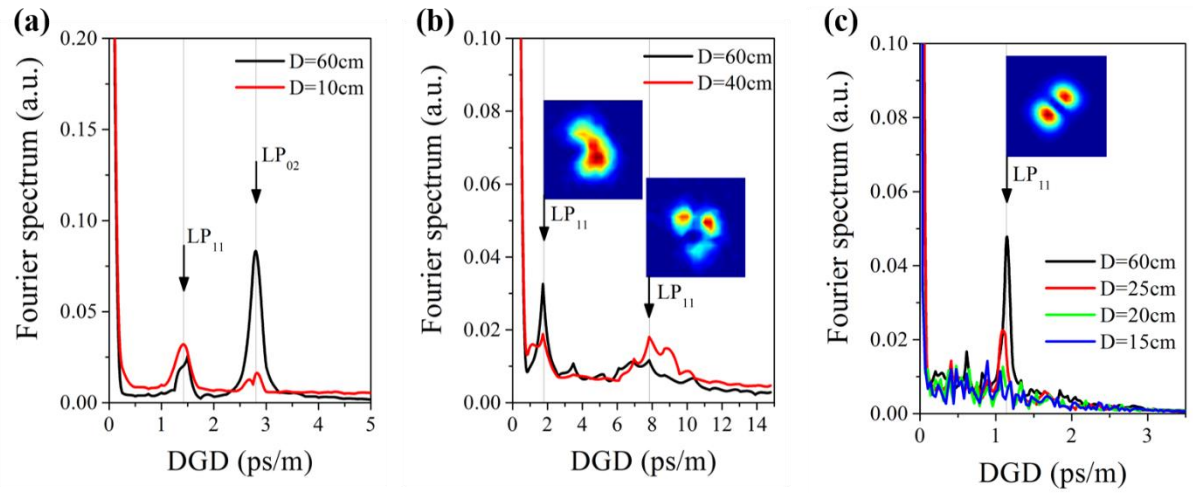

Figure 4-10: S^2 imaging Fourier spectra of the LMA SIF (A), PCF (b), and LMA LCF (c) for various coiling diameters. The guided HOMs are indicated with an arrow and the corresponding reconstructed modal amplitude is shown in the respective inset.

When the LMA PCF was coiled tighter, some amount of LP_{11} was suppressed. However, a small amount of HOM remains indicated by the profile reconstructed and shown in Figure 4-10(b). Finally, the effect of coiling the LCF on the HOM LP_{11} has been measured and results are presented in Figure 4-10(c). This fiber could be coiled down to 15 cm diameter without inducing major bend-induced losses indicating a good light confinement in the core. From the Fourier

analysis, the initially guided LP_{11} mode could be very efficiently suppressed below 20 cm diameter coil.

Results from these mode analysis measurements were summarized and the MPI values of each guided mode in each fiber design are plotted as function of fiber coil in Figure 4-11: SIF in black, PCF in red and LCF in blue. Unfilled symbols are used for MPI values of the LP_{11} modes and solid symbols denote LP_{02}. Results show that the MPI of the single HOM guided in LMA PCF and LCF designs has been reduced by 5 and 18 dB after coiling the fiber around 40 cm and 15 cm diameter, respectively. As a result, values of $\rho^2(LP_{11})$ as low as 0.5 % and 0.07 %, respectively could be measured. In the SIF however, while LP_{02} is efficiently suppressed (MPI reduced by ~ 20 dB), coiling-induced mode coupling and power transfer occurs resulting in a slight increase of the power carried by LP_{11}.

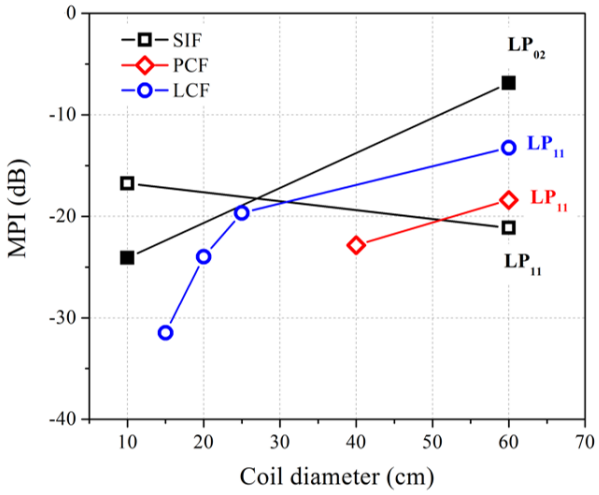

Figure 4-11: Measured MPI in the SIF (black), PCF (red) and LCF (blue) designs for various coiling diameters. For MPI ofLP_{11}1, open symbols are used while filled symbols are data for the mode LP_{02} (only measured in the SIF). Lines are shown for guidance of the eye.

4.2.3 Comparison of the single-mode performances between LMA fiber designs

4.2.3.1 Single-mode purity

The single-mode purity can be defined as the fraction of power that is carried by the FM during light propagation. Using the measured MPI and MP values, the single-mode purity can be calculated by subtracting the sum of the HOM ρ_n^2 from the total value of 1. Results are plotted in Figure 4-12 as function of coil diameter for the LMA SIF, PCF and LCF in black, red and blue respectively. From the single-mode purity results, the critical coiling diameter to ensure single-mode propagation, labeled D_{SM} can be determined. From the S^2 imaging mode analyses we demonstrate that ~100% single-mode purity can be achieved in the PCF and LCF designs at D_{SM} = 40 cm and 20 cm, respectively. These locations are indicated by filled symbols in Figure 4-12. The corresponding overall bend-induced losses, arising from light being coupled in the cladding, has been measured after recording the total transmitted power (in the LMA fiber cores) before coiling (D > 60 cm) and at D_{SM}, and are indicated in Figure 4-12. Light propagating in the PCF experiences higher bend-induced losses while reaching the single-mode regime compared to the LCF design. Furthermore, it was possible to reach an ultra-pure single-mode regime in the LCF where more than 99.9 % of the light was measured in the FM LP_{01} for D_{SM} = 15 cm with limited bend-induced losses. As a result, both designs are able to deliver pure single-mode 2 μm light with strong potential for high performances fiber laser applications. In comparison, only 90% single-mode purity could be achieved in the SIF design indicating that, even after coiling the fiber around a tight loop of 10 cm in diameter, a residual amount of power was still carried, mainly by LP_{11}. As a result, pure single-mode propagation could not be reached.

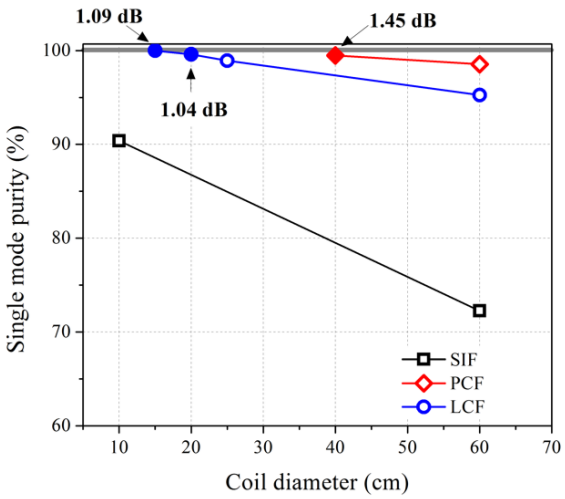

Figure 4-12: Single mode purity of the 2 μm beam emerging from the SIF (black), PCF (red), and LCF (blue) as function of coiling diameter. Single-mode regimes are indicated by plain markers. The values indicate the overall bend-induced losses measured at specific coil diameters.

4.2.3.2 Mode effective area

In addition to bend-induced losses, tight coiling of LMA fibers also influences the profiles of the emerging beam and the mode-field area (MFA) of the FM [52][115]. To measure and compare the MFA between the LMA fiber designs, our starting point was to image the near-field of the total beam emerging the LMA PCF and LCF on the CCD at the single-mode regime previously determined (smallest coiling diameter for the SIF). These profiles are shown in Figure 4-13(a), (b) and (c), respectively. Transverse profiles have been extracted from the measured 2D profiles after D > 60 cm (representing the case of an unperturbed and straight fiber) and at D_{SM}. After applying a Gaussian fitting function, the value of MFD, defined at $1/e^2$ from the maximum, has been extracted. As a result, the mode-field area (MFA) was calculated and the results are plotted in Fig. 6(d) for the SIF (black), PCF (red) and LCF (blue) designs. Filled symbols denote pure single-mode light propagation at D_{SM}. In these cases (40 cm for the PCF and 15 cm for the

LCF), the coefficient of determination of the Gaussian fit, labelled R^2, is shown in Figure 4-13(d) indicating a very good fitting quality. The MFA of the beam emerging both LMA PCF and LCF designs experience a decrease as the single-mode regime is reached. This trend confirm the suppression of residual HOM content.

For comparison, the MFAs of the three LMA fibers have been calculated from the theoretical MFD values given in Table 7. These MFAs are plotted in Figure 4-13 as three solid lines with respective colors. For the PCF and LCF, measured MFA values show a very good agreement with numerical predictions once single-mode propagation has been achieved. It can be noted that the corresponding beam profiles measured and shown in Figure 4-13(a) and (b) show a good uniformity. In the SIF design however, as the coiling diameter decreases, significant beam distortions have been observed which is related to the increased of LP_{11} MPI. As a result, the MFA value at 10 cm coil was determined by artificially fitting the distorted beam to a Gaussian distribution. Thus, this particular measurement value is not accurate as indicated with a large error bar. It should be also noted that, for this particular SIF, there might be a bending regime, perhaps in-between 10 cm and 60 cm, where a purer single-mode beam could be achieved due to reduced LP_{01}-to-LP_{11} coupling at specific bending diameters.

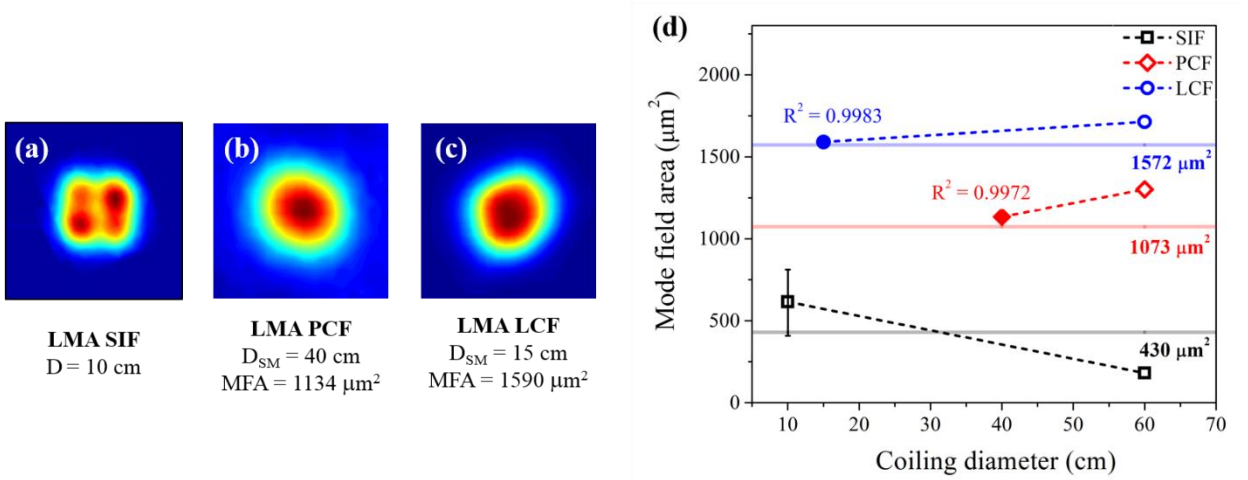

Figure 4-13: Measured intensity profiles emerging LMA SIF (a), PCF (b) and LCF (c). (d) Measured mode-field area for different coiling diameters in black, red and blue, respectively. Filled symbols indicate single-mode beams. For comparison, MFAs (at 2 µm, without bending) have been calculated for each fiber. Values are indicated in (d) below the corresponding colored lines.

4.2.4 Compared performances summary between LMA SIF, PCF and LCF

In summary, S^2 imaging was performed using a broadband light source emitting at 2 μm to characterize and compare the performances of three LMA fibers in terms of single-mode delivery and available MFA. First, it was demonstrated that light guided and propagating in unperturbed LMA fiber designs is, slightly multi-mode in the case of the PCF and LCF (with a residual amount of power carried by the first HOM LP_{11}), or clearly multi-mode in the SIF. Efficient HOM suppression in the PCF and LCF designs was measured under proper coiing conditions.

From the three samples investigated, it could be concluded that PCF and LCF designs appear to be the most promising candidate to ensure stable, single-mode, high efficiency and high quality 2 μm laser emission. These LMA designs outperform the SIF, delivering single-mode beam purity higher than 98% after coiling PCF and LCF with diameters of 40 cm and 20 cm,

respectively, where the maximum single-mode purity achieved in the SIF was not exceeding 90% under coiling diameter as small as 10 cm due to residual inter-modal coupling. In addition, it is worth noting the good performances of the LCF design, originally not designed to perform in this wavelength range. For coiling diameters around 15 cm, ultra-pure single mode regime has been demonstrated corresponding to more than 99.9% of the light carried by the FM with an available mode-field area of ~ 1600 μm^2. The later results make this design a promising candidate for further power scaling applications of fiber lasers.

It is important to note that other LMA fiber designs, different from the ones used in this study, have also been demonstrated for single-mode 2 μm laser emission such as large-pitch fibers with MFD ~60 μm [120]. Recently, novel Tm-doped PCF designs have been numerically demonstrated to deliver robust single-mode operation with ~80 μm MFD [140].

These recent studies illustrate the high interest of the scientific community in compact and high performances 2 μm sources. The results presented in this study have demonstrated the significant influence of the design parameters on the performances of the delivered beam. It emphasizes the need for high-accuracy fiber fabrication procedures and in-depth diagnostic techniques able to accurately decompose the light.

CHAPTER 5: MONOLITHIC INTEGRATION OF SPECIALTY FIBERS IN ALL-FIBER LASER SYSTEMS

Advances in the research field of optical fibers can be sorted in two distinct trends. On one hand, the demonstration of a wide variety of novel specialty fiber designs, tailored to deliver high-optical performances, have significantly contributed to improve existing optical systems as well as to discover new applications (e.g. fiber lasers, supercontinuum generation, mode-division multiplexing, etc). This trend were highlighted in Chapters 3 and Chapter 4 of this dissertation. On the other hand, taking advantage of the success of fiber-based optical systems, a large variety of fiber-based optical components were demonstrated in the past two decades. Fiber-based devices have been generally fabricated using SIF designs such as directional coupler [141], polarization sensitive coupler and splitters [142], Faraday isolator and circulator [143], multi-channels pump combiners [144] and fiber Bragg gratings (FBG) [145]. They are robust, compact and cost-effective, offering a wide range of possibilities to transfer free-space optical elements into efficient, all-fiber integrated systems.

This Chapter of the dissertation is centered on the monolithic integration of specialty fibers into all-fiber systems. In practice, SIFs (used in conventional fiber devices) and novel specialty fiber designs are poorly compatible due to their different sizes and designs. As a result, their monolithic integration raises several challenges which are listed in Section 5.1. In Section 5.2, a novel all-fiber Mode-Field Adapter (MFA) device is demonstrated to efficiently couple the light between two fibers with different core sizes followed by Section 5.3 presenting the first

demonstration of efficient light transmission through a monolithic fiber chain made with a SMF and a LMA PCF is achieved using all-fiber MFA devices. The MFA concept is extended to assemble the first monolithic fiber laser combining a conventional FBG devices in SMF and an active LMA PCFT. Results are detailed in Section 5.4 and summarized in Section 5.5.

5.1 Motivation and challenges

All fiber architectures offer unique advantages compared to free-space based optical systems. However, their practical realization is often challenging due to the differences in fiber material, fiber structures and fiber sizes.

5.1.1 Monolithic all-fiber systems

Fiber-based optical systems outperform free-space architectures in terms of compactness (fibers are in essence flexible and can be bent), robustness (due to the reliability of fusion splicing techniques), stability (high purity Fused Silica glass have a low thermal expansion coefficient which makes them mechanically stable in addition of being chemically stable up to ~1000 °C) and efficiency (low-attenuation of light wavelengths ranging from the visible to the near-IR). In addition, a wide variety of cost-effective fiber-based devices are commercially available offering several alternatives to design all-fiber systems.

However, the dimensions and design discrepancy between conventional fiber components using SIFs and specialty fibers limits their monolithic integration. As a result, even though tailored specialty fiber designs enable high optical performances, their implementation has been restricted, in most cases, to free-space architectures which are likely to deliver unstable performances due to

difficult and time-consuming optical alignments. To address this limitation, a few studies have been published in the literature to demonstrate specialty-fiber-based optical components such as FBGs [146][147], PCF couplers [148] and wavelength independent mode converters [149]. However, specialty fiber-based devices cannot be easily manufactured at large scales and are only applicable to optical systems using the same specific fiber design.

5.1.2 Challenges related to efficient fiber-to-fiber light transmission

When assembling fibers made of different material, designs and (or) dimensions, light transmission suffers from losses at the fibers interface related to parasitic reflection (e.g. Fresnel reflection), misalignment or mode-field mismatch. Losses related to Fresnel reflections can be mitigated using an appropriate index matching oil. The relative fiber misalignment can be minimized by performing active fiber alignment during fusion splicing. In comparison, mode-field mismatch depends on intrinsic properties of the optical fibers. The fraction of transmitted light after propagation through a junction between mode-mismatched single-mode fibers can be estimated using the relation demonstrated by Marcuse [49]:

$$T = \frac{4\omega_1^2\omega_2^2}{(\omega_1^2 + \omega_2^2)^2} \qquad (46)$$

where ω_1 and ω_2 are the mode-field radii of the fundamental mode.

The easiest and most commonly implemented method to reduce coupling losses between mode-field mismatched optical fibers is to use free-space imaging schemes made of lenses associations with appropriate magnification factor. However, the introduction of free-space optical elements increases the overall footprint of the optical system and introduces a higher degree of

complexity in the optical alignment, resulting in lower coupling efficiencies, and strongly influencing the laser output stability, performances and handling.

A concrete example in which mode-field matching is crucial is in the development of monolithic fiber lasers. In the last decade, increased performances of fiber lasers in terms of power and energy scaling have been reported [150], [151], first employing LMA SIF [152] and later using LMA PCF [153]. The monolithic integration of fiber lasers present several advantages over systems based on free space elements: compactness, user-friendly and stability of laser emission is therefore easier to achieve. To date, several LMA SIF-based high-power laser systems presenting monolithic architectures have been demonstrated [154], [155]. However, LMA PCF-based laser and amplifier systems typically employ several free space sections [156]–[158].

A typical example is the monolithic integration of LMA PCFs which is attractive and yet challenging due to the poor compatibility with SMF-based components in terms of design and dimensions. The complex nature of the inner structure of PCFs requires highly controlled splicing procedures to achieve low-loss SMF-PCF splices. Often, detrimental effects such as air-holes collapsing, stress formation at the splice and misalignment occur and need to be mitigated. In the case where the SMF and the PCF present similar MFDs, successful splices have been realized using controlled fusion splicing techniques [159],[160]–[162] and CO_2 lasers [163]. Efficient light transmission with splice losses between ~ 0.5 up to ~ 2 dB/splice has been measured. On the other hand, PCF core dimensions, in particular LMA designs, differ from typical SMF. PCF-to-SMF coupling has been demonstrated using mode-field matching techniques involving tapering [164], [165] and pressure-assisted splicing [166]. Furthermore, a few mode-field matching techniques have been reported between large PCF-to-SMF. One of them involved a GRIN fiber lens surrounded by two coreless fiber segments to reproduce the typical scheme of free-space imaging

[167]. However, this approach is limited to passive PCFs with a maximum PCF-to-SMF mode-field- mismatch on the order of four. Furthermore, thermal expansion of cores is a method commonly employed in industry to efficiently couple pump light from multi-mode SIF into double cladding LMA PCF-based high power fiber amplifiers [168]. The latter method requires rather bulky and expensive equipment resulting in complex realization. The permanent changes induced to the inner structure and size of the PCF which might affect the propagating light. As a result, the output performances of the system may be substantially modified.

5.2 All-fiber mode-field adapters (MFA): concept and introduction

In this section, a novel all-fiber approach to achieve mode-matching and mitigate coupling losses is presented in details.

5.2.1 MFA using graded-index multi-mode fibers

The novel mode-field matching approach demonstrated in this section uses the concept of Multi-Mode Interference (MMI) previously described in Section 2.3 of this dissertation. MMI occurs in MMFs and the two most common designs are the Step-Index Multi-Mode Fibers (SIMF) and Graded-Index Multi-Mode fibers (GIMF). In these fibers, both dimensions and numerical aperture were chosen to guide multiple transverse modes as previously defined in Section 2.2.2. The typical index profiles of a SIMF and a GIMF made with the same core radius R are schematically represented in Figure 5-1(a) and (b) respectively. The index profile of SIMFs is defined by Equations (1) and (2) with n_1 and n_2, the refractive index of the core and cladding layers respectively. On the other hand, the parabolic index profile of GIMFs is defined by [32]

$$n(r) = n_0 \sqrt{1 - 2\Delta \left(\frac{r}{R}\right)^2} \qquad (47)$$

with n_0 the index at the center of the core, Δ the fractional refractive index difference and $\alpha \approx 2$ in the fiber core characterizing the near-parabolic index profile ($\alpha \approx 1$ in the cladding).

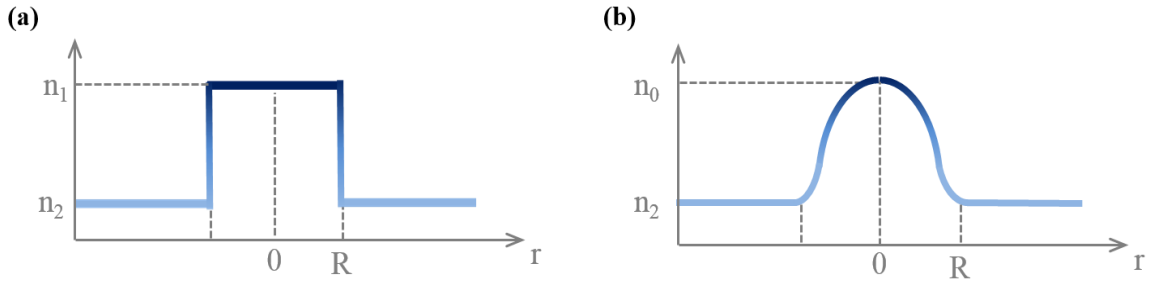

Figure 5-1: Schematic representation of the refractive index profile of (a) a Step-Index Multi-mode Fiber (SIMF) and (b) a Graded-Index Multi-mode Fiber (GIMF) with identical core radius labeled R.

The concept of mode-field adaption using MMF is detailed using the example of two commercially available SIMF and a GIMF with R = 25 μm. After measuring the refractive index distribution in both fibers (procedure detailed in Section3.4.1), index values at λ = 1550 nm and fiber dimensions were used in a mode solver (Fimmwave from PhotonDesign) to numerically determine the propagation constant β_n of the guided modes. Assuming that the light coupled in the MMFs is aligned with the center of the core, only the radially symmetric modes $LP_{0,m}$ are excited due to the input mode overlap (detailed explanation can be found in Section 2.4.1). Results are plotted for the first $LP_{0,m}$ in Figure 5-2 with unfilled markers and full markers in the case of the SIMF and the GIMF respectively. The results from the numerical mode solver indicate that the modes guided in SIMF and the GIMF follow different trends. In the SIMF, guided modes are propagating with decreasing propagation constants as the mode-order increases. In GIMF, a similar trend is obtained from the calculations, however, the decrease is linear (indicated by a

dashed line in Figure 5-2). As a result, the relative propagation constant difference $\Delta\beta$ (with $\beta = k_0 n_{eff}$ according to Equation (9)) between the guided $LP_{0,m}$ modes, i.e. their relative effective index difference Δn_{eff}, is constant. In terms of MMI, defined by Equation (34), this translates into a periodic oscillation during light propagation in the GIMF whereas the MMI in SIMF is the result of the superposition between several oscillatory functions with random periodicities.

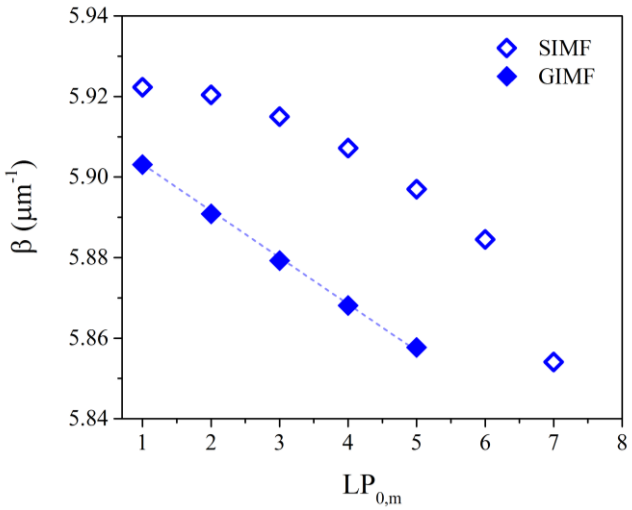

Figure 5-2: Calculated propagation constant β_n of the first guided Bessel modes $LP_{0,m}$ in the SIMF (unfilled markers) and in the GIMF (full markers) using a mode solver. The MMF are commercially available with a core radius R = 25 μm. Their refractive index were measured at λ = 1550 nm and the values were used in the mode solver.

To illustrate this particular phenomenon, results of light propagation in the SIMF and the GIMF, calculated using a commercial software package called Fimmprop (by PhotoDesign), are presented in Figure 5-3(a) to (d) respectively. In both cases, the input fiber was assumed to be single-mode at the calculation wavelength λ = 1550 nm. Results of the calculated light intensity propagating in the core of a 10 cm long segment of SIMF and along a 1.2 mm long segment of GIMF are show in Figure 5-3(a) and (c) respectively. As expected from the results in Figure 5-2, the total light (i.e, the linear superposition of all the guided modes) propagating in the SIMF exhibits a chaotic behavior due to the complex MMI. In comparison, the intensity of light

propagating in the GIMF is periodic due to the constant Δn_{eff} between the guided modes which results in a periodic MMI pattern. For completion, the normalized transmission has been calculated using a second segment of SMF at the MMF outputs. Results are plotted as function of the MMF length and show Figure 5-3(b) and (d) corresponding to the SIMF and the GIMF respectively. The Self-Reproduction Length (SRL), corresponding to the propagation distance z after which the initial phase relation between the guided modes is retrieved (previously defined in Section 2.3 with Equation (36)) was calculated. Due to the high degree of randomness of the MMI occurring in the SIMF, SRL > 10 cm compared to SRL = 0.5 mm in the GIMF. As a result, results in Figure 5-3(c) and (d) indicate that the length of the GIMF segment z can be accurately chosen to achieve self-imaging (z = 500 μm in the present case). Most interestingly, controlled length of GIMF can be used to act like a beam expander and deliver larger beams (for example at z = 250 μm).

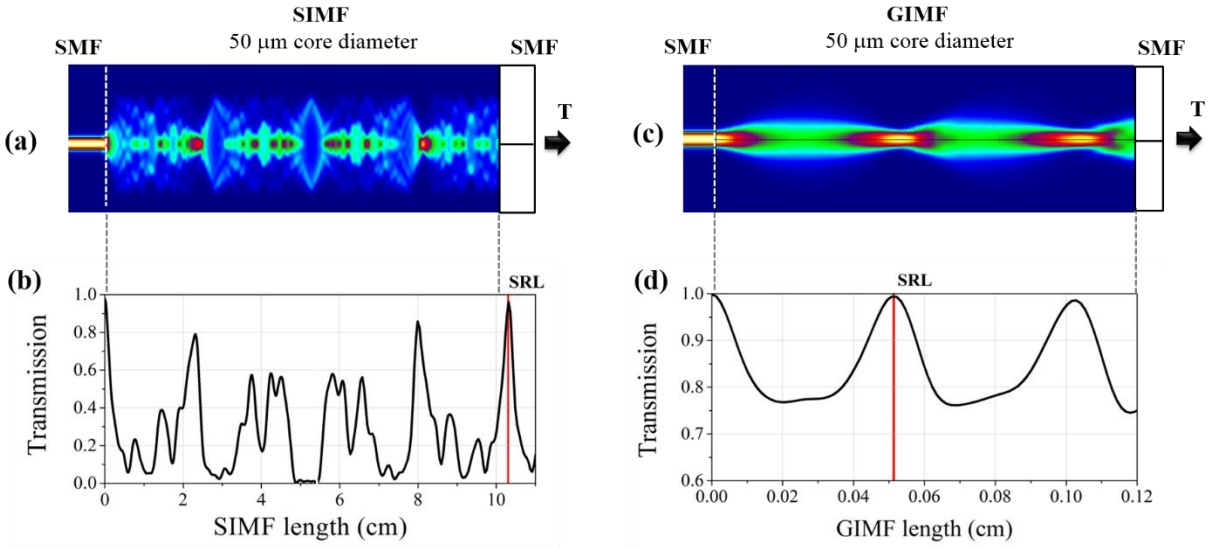

Figure 5-3: Calculated light propagation in a 50 μm core diameter (a) SIMF and (c) GIMF. The in-coupling fiber is single-mode at the calculation wavelength λ = 1550 nm. The normalized transmission has been calculated as function of the fiber length when collecting with a SMF after the SIMF (b) and the GIMF (d). The red line indicates the Self-Reproduction Length (SRL) (defined in Section 2.3).

5.2.2 MFA between mismatched step-index fibers

The concept of using selected lengths of GIMFs to control the beam expansion has been successfully implemented in analytical and experimental studies to mitigate losses at the coupling between two mode-mismatched single-mode Step-Index Fibers (SIF) [48], [169]. In the following, important results regarding mode-field matching achievements, previously published in the literature, are highlighted as an introduction to the upcoming Sections 5.3 and 5.4. The system presented in Figure 5-4 has been demonstrated by Hofmann *et al.*at the University of Central Florida [169]. Light transmission at the wavelength λ = 1550 nm was studied through a fiber chain made of two single-mode SIFs presenting an initial mode-field area mismatch of a factor 4. A Single-Mode Fiber (SMF) with core diameter of 10 μm and a Large-Mode Area (LMA) fiber with 20 μm core in diameter are illustrated in Figure 5-4(a). According to Equation (46), only 60% of the light is transmitted.

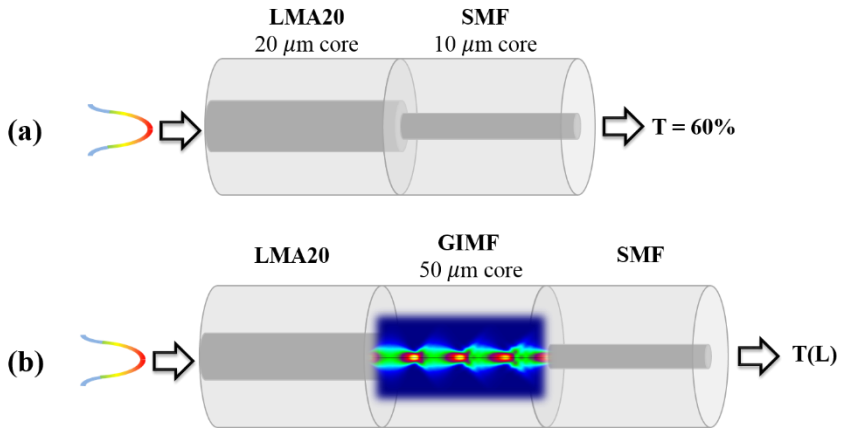

Figure 5-4: (a) Illustration of the direct coupling between a Large-Mode Area (LMA) with 20 μm core and a 10 μm core Single-Mode Fiber (SMF) resulting in 60% of the light being transmitted. (b) Schematic of the mode-matched fiber chain using a Mode-Field Adapter made of a GIMF segment. Light transmission varies according to the selected length of GIMF employed.

Experimentally, after introducing a 275 μm long piece of GIMF with 50 μm core diameter between the SMF and the LMA fiber, as shown in Figure 5-4(b), the initial coupling losses have been reduced from 40% down to less than a few percent [169]. The selected segment of GIMF is called Mode-Filed Adapter (MFA) and is determined according to the initial mode-field mismatch between two fibers. Besides being extremely compact, GIMF-based MFA devices were demonstrated to be robust, stable and reciprocal devices, achieving high mode-matching perfoemances under large temperature gradients (under 100°C) and across spectral bandwidth of several hundreds of nm.

5.3 MFA between a LMA photonic crystal fiber and conventional fiber

Most of the fiber lasers employing LMA PCF are built incorporating free-space optical elements. The main reason arising from the high structural and dimension mismatch with conventional fiber-based devices. In the following section, the ability to mode-match an active LMA PCF with a SMF using GIMF MFAs is numerically and experimentally studied. Results presented in Sections 5.3 and 5.4 have been published in the literature [170]–[172].

5.3.1 Motivation

The two fibers detailed in this section are illustrated in Figure 5-5. First of all, the conventional SMF (Fibercore SM980 shown in Figure 5-5(a)) had a single-mode cutoff at λ = 980 nm and a core diameter of 5.8 μm. This fiber is commonly employed in fiber-based optical devices operating around λ = 1060 nm. The second fiber is an active (Yb-doped core) double-clad LMA PCF (fabricated by NKT Photonics) with a 40 μm core diameter and a 200 μm diameter pump

cladding (Figure 5-5(b)). This specialty fiber was developed for amplifier and laser applications including power scaling [157], [158]. Due to its large dimensions and complex design, the LMA PCF was implemented in free-space laser architectures. Images of the SMF and LMA PCF facets were recorded with a microscope and are shown in Figure 5-5(a) and (b) respectively. The size ratio between these structures is respected to emphasize their relative size and structural differences. Results of the calculated mode profile (λ = 1060 nm) guided in each fiber core are shown in Figure 5-5(c). The Mode-Field Diameter (MFD), defined at $1/e^2$ from the intensity maxima, was calculated to be 27 μm in the LMA PCF compared to 6.3 μm in the SMF resulting in a factor ~18 mismatch between the two mode-field areas. As a reminder, to the date of this dissertation, only a factor 4 mismatch between the mode-field area of two different fibers has been successfully demonstrated [167], [169].

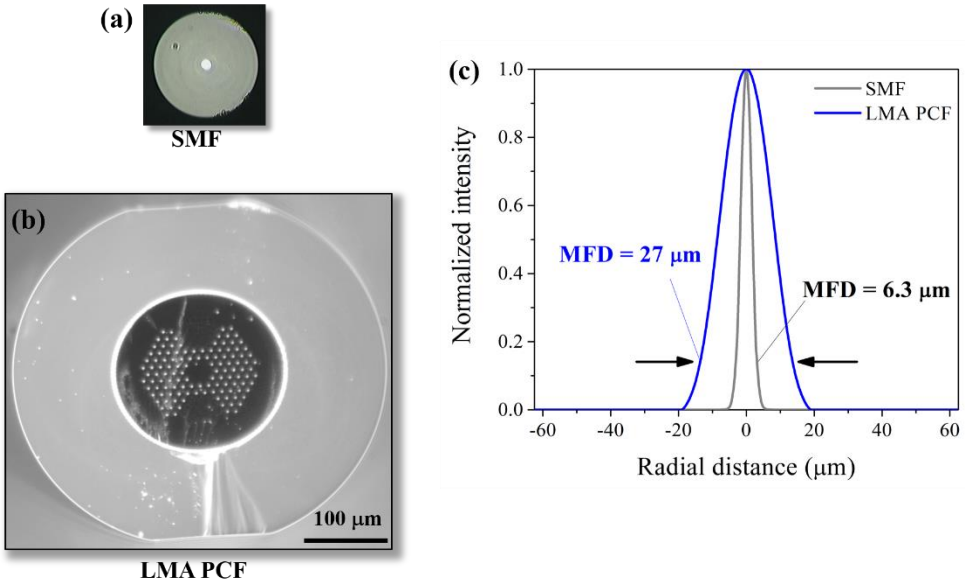

Figure 5-5: Microscope image of the fibers facets: (a) a conventional SMF and (b) a double-clad, active LMA PCF. The dimensions of images (a) and (b) have been scaled to represent the realistic size mismatch between the SMF and the LMA PCF. (c) Calculated mode profile (λ = 1064 nm) guided in the core of the SMF (black) and the LMA PCF (blue). The Mode-Field Diameter (MFD) values measured at $1/e^2$ (indicated with two arrows).

5.3.2 Numerical calculation of optimized mode-field matching

During light propagation from the LMA PCF directly coupled to the SMF, only 20% of the light is expected to be transmitted (estimated using Equation (46) and the calculated MFD values in Figure 5-5(c)). In order to predict the optimum conditions for mode-field matching GIMF-based MFA devices, numerical simulations have been performed at λ = 1064 nm (wavelength in the absorption band of the Yb-dopants in the core of the LMA PCF). The light transmission has been calculated through the SMF-MFA-PCF chain schematically presented in Figure 5-6(a). Several GIMFs with core diameters of 50 μm, 62.5 μm and 100 μm, labeled GIMF50, GIMF62.5 and GIMF100 respectively, were investigated. The calculated light transmission in the LMA PCF core, plotted as function of the GIMF segment length, are presented in Figure 5-6(b). As a result, the beam expander capabilities of GIMFs are confirmed as it appears that the overall transmission through the fiber chain can be improved by using segments of GIMFs between the SMF and the LMA PCF. In particular, the highest transmission was calculated when using a MFA device made with a 250 μm long segment of GIMF50, corresponding to the SRL of the MMI. In this case, it was found that the transmission increased from 23% (without MFA which is in agreement with the predicted values using Equation (46)) up to 95.8 %. This increase was due to the mode-overlap achieved between the SMF and the LMA PCF using the GIMF50 MFA. In comparison, the overall transmission could also be improved using segments of GIMF62.5 and GIMF100 but did not outperform the transmission levels reached with GIMF50. This can be explained by the fact that mode-matching capabilities of a GIMF do not only depend on the size of the core, but it also depends on the refractive index profile and on the number of guided modes. In addition, an overall

transmission of 100% could not be achieved with any of the GIMF commercially available. However, it could be possible to tailor a GIMF design to achieve higher transmission values.

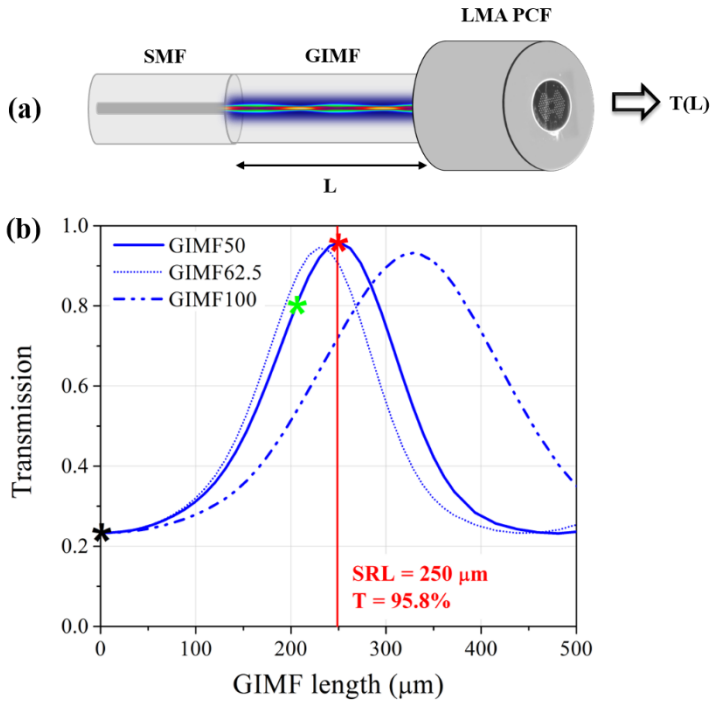

Figure 5-6: (a) Schematic representation of the mode-matched SMF-MFA-LMA PCF chain. (b) Calculation results of light transmission through the chain shown in (a) as function of GIMF length considering three different GIMFs with different core sizes. (The red, green and black markers will be used in the Section 5.4.2).

To complete this numerical approach, a complete chain made of two SMF-LMA PCF junctions has been modeled. The system is illustrated in Figure 5-7(a) and (b) where the direct coupling case between the SMF and the LMA PCF is compared to the mode-matched chain using the MFAs previously determined. The overall light transmission collected in the output SMF was calculated at λ = 1064 nm. The low light transmission of 5.5% (corresponding overall loss = -12.5 dB) measured in the SMF-PCF-SMF chain has been (Figure 5-7(a)) has been significantly improved using two MFAs made of 250 μm long segments of GIMF50 to 92% (Figure 5-7(b)).

Up to 92% of the overall light was transmitted (corresponding overall loss = -0.4 dB) when using appropriate MFAs corresponding to an overall improvement of 12 dB.

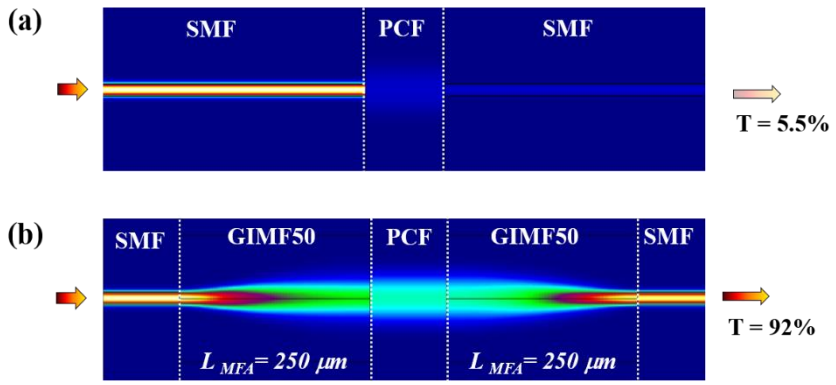

Figure 5-7: Calculated light transmission (λ = 1064 nm) through two complete monolithic fiber chains. (a) Case of direct coupling case SMF-PCF-SMF resulting in 5.5% of light being transmitted. (b) Using two MFAs made of 250 μm segments of GIMF50 at the SMF-PCF junction increases the overall transmission to 92% (corresponding to 12 dB improvement).

5.3.3 Experimental realization and characterization

An easy, robust and reproducible assembly procedure to fabricate the two fiber chains simulated in Figure 5-7, has been elaborated and individual steps are presented in this section. The procedure is initiated by fusion splicing a piece of SMF to a piece of GIMF using a standard arc-based splicer (FSU 995 by Ericsson). Then, high-precision cleaving of the selected GIMF segment is achieved with micrometric resolution using a fiber cleaver (FK 11 by PK Technology) fixed on a translation stage with micrometer steps increments and imaged with a 20x microscope objective. After imaging the splicing point between the SMF and the GIMF, the diamond blade is translated by the desired GIMF length and then cleaved with an established accuracy of ± 5 μm. In the final step, the SMF-GIMF chain is fusion splices with the active LMA PCF. To simplify this procedure, the PCF outer diameter was chemically etched down from 440 $\mu\mu$ to 240 μm, decreasing the

difference with the SMF outer diameter of 125 μm. A filament-based splicing system (GPX-3000, Vytran), which allows to actively control the splicing parameters, was used to achieve mechanically strong SIF-to-PCF splices without altering the original air-hole structure of the PCF cladding. A microscope image of a complete chain SMF-MFA-PCF-MFA-SMF fabricated following these steps is shown in Figure 5-8(a).

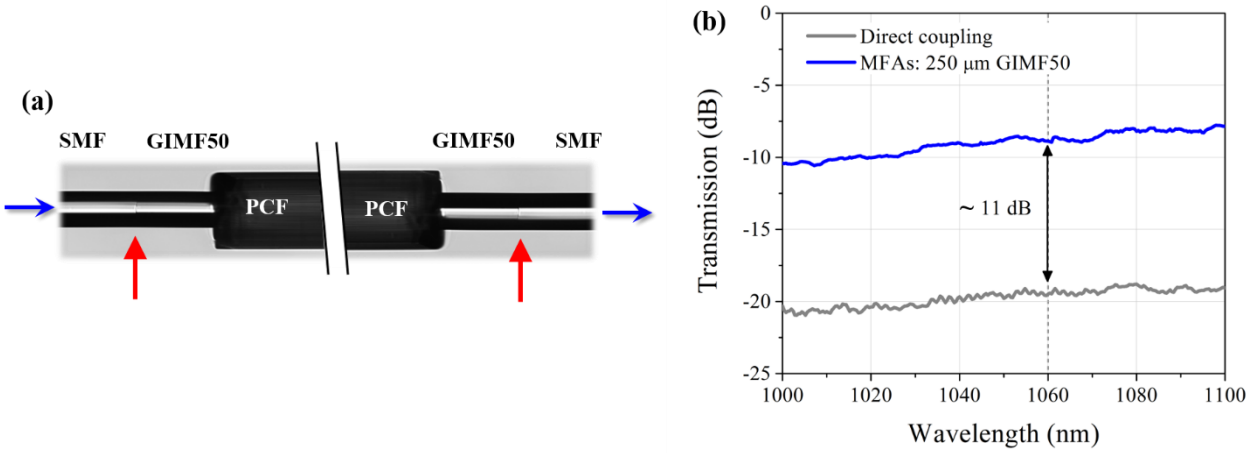

Figure 5-8: (a) Microscope image of a monolithic chain SMF-MFA-PCF-MFA-SMF where each MFAs is a 250 μm long pieces of GIMF50. The splicing points between the SMF the GIMF are indicated with red arrows. (b) Measured light transmission through two fiber chains without (grey) and with MFAs (blue) showing 11 dB of improvement in the overall transmission at λ = 1064 nm.

To measure the transmission through the two fabricated chains, a superluminescent diode (Thorlabs), emitting a bandwidth of 60 nm centered around 1050 nm, was used as the light source and was coupled into the core of one of the SMF. The transmission was recorded at the second SMF end using an OSA (Yokogawa). Results of measured light transmission are shown in Figure 5-8(b), comparing the transmission through SMF-PCF-SMF (grey line) with the transmission through the mode-matched chain SMF-MFA-PCF-MFA-SMF (blue line). The transmission recorded after the mode-matched fiber chain has improved by ~11 across the full spanning range. These results confirm the finding of Hofmann et al. who demonstrated that short MFA segments

perform across hundreds of nm of spectral bandwidth [169]. In particular, the transmission measured after the chain SMF-PCF-SMF increased from -20 dB to -8 dB when using MFAs designed at λ = 1064 nm. These experimental results are in agreement with the ~12 dB improvement predicted with the numerical simulations in Figure 5-7. Thus, the significant increase in transmission has been experimentally confirmed using appropriate GIMFS MFAs between two fibers presenting an intrinsic mode-field area mismatched of a factor 18 [170]–[172].

In both chains, the remaining ~10 dB losses can be attributed to residual splicing losses between the SIF and the PCF. In practice, it has been particularly challenging to achieve reliable and good quality cleaves of the PCF facet. However, it is possible to achieve reasonably low splicing losses using highly controlled techniques (e.g. CO2 splicers) and splice loss under 2 dB have been demonstrated between SIF and PCF [159],[160]–[162].

5.4 Novel all-fiber laser employing an active LMA PCF and conventional fiber Bragg gratings

In this section, the GIMF MFA approach is extended to assemble monolithic fiber lasers utilizing FBGs written SMF to provide the cavity feedback and active LMA PCF as the gain medium. Two different fiber lasers have been assembled and results of the characterization are presented and discussed.

5.4.1 First experiment: monolithic laser using one MFA

The first monolithic laser is illustrated in Figure 5-9. A Multi-Mode Laser Diode (MMLD) emitting at λ = 974 nm wavelength was fiber-coupled to a SIMF with 105 μm core and 125 μm

cladding diameter. The SIMF was fusion spliced to the SMF in which a high reflector (HR) FBG has been inscribed to reflect 99% at the Bragg wavelength λ = 1064 nm with 14 nm FWHM bandwidth. The FBG SMF segment was uncoated and the length kept under 2 cm to prevent pump scattering losses. The PCF cladding absorption was measured around ~15 dB/m at 974 nm pump wavelength. Thus, the length of active PCF used in the cavity for efficient pump absorption was ~1.1 m to ensure high pump absorption. The monolithic laser cavity was terminated by the flat cleaved output facet of the active PCF providing ~ 4% feedback from the Fresnel reflection. Two chains have been fabricated, one including a MFA (250 μm ($\pm$ 5 μm) long segment of GIMF) between the FBG SMF and the LMA PCF, and one by fusion splicing the FBG SMF directly to the PCF. In the mode-matched chain, the ~2 cm long SMF-GIMF section was packaged robustly mounted on microscope slides to ensure mechanical strength and stability as well as low pump scattering loss.

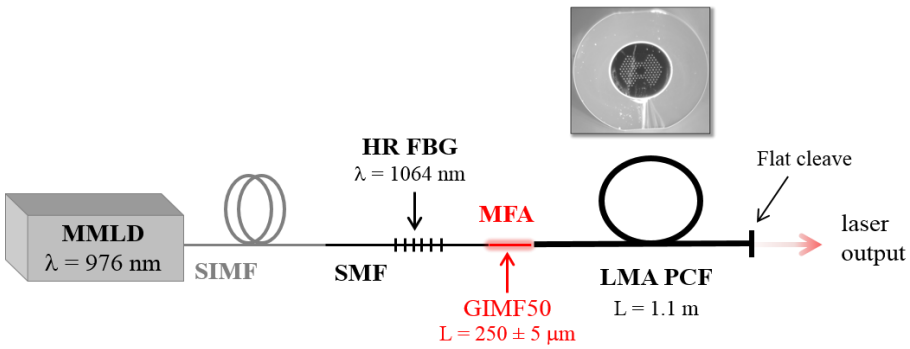

Figure 5-9: Schematic of the monolithic fiber laser cavity including a 99% high reflector fiber Bragg grating at 1064 nm ($\Delta\lambda$=14 nm) and ~ 4% reflective output coupler.

The emission spectrum at the output of the direct-coupling chain and the mode-matched chain has been measured above threshold with an OSA (Yokogawa) and results are presented in Figure 5-10(a). The direct-coupling chain SMF(HR FBG)-PCF, plotted in grey in Figure 5-10(a), emits a free-running laser line centered at 1030 nm, wavelength corresponding with the maximum

gain of the Yb-atoms. Since no mode-field matching section was used in this case, this laser emission arises from parasitic reflections at the SMF-to-PCF interface which has been previously characterized with considerable losses (Figure 5-8(b)). In comparison, when pumping the mode-matched chain SMF(HR FBG)-MFA-PCF above threshold, a laser line centered at 1058 nm with ~ 30 dB signal-to-background ratio was recorded (blue line in Figure 5-10(a)). This laser emission was generated from the cavity formed between the HR FBG (14 nm FWHM bandwidth is visually indicated in Figure 5-10(a)) and the 4% reflection at the PCF output. The output power measured emitted from the mode-matched laser cavity was measured while varying the launched pump power and results are presented in Figure 5-10(b) showing a 60% of laser slope efficiency. The maximum measured output power of ~8 W was limited by the available pump power and by the high splicing loss. However, in this configuration, the laser line-width could not be accurately controlled due to the large HR FBG bandwidth.

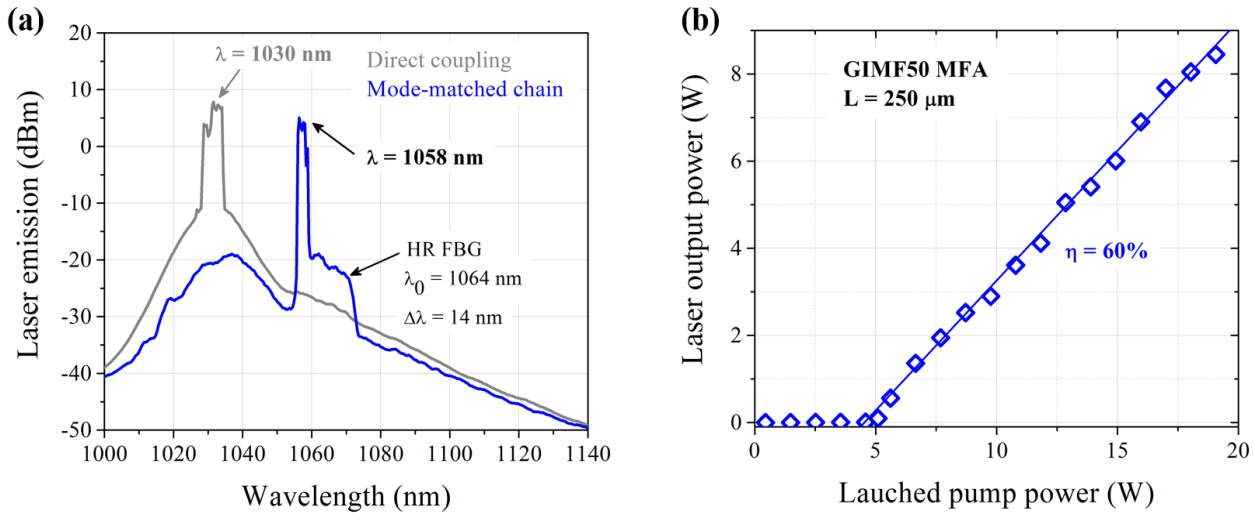

Figure 5-10: (a) Measured emission spectrum above lasing threshold through two monolithic fiber cavities with (blue) and without (grey) MFA between the HR FBR and the LMA PCF. (b) Output power measured at the λ = 1058 nm laser line emitted by the mode-field matched laser cavity as function of the launched pump power.

5.4.2 Second experiment: all-fiber laser using two MFAs

A second monolithic fiber laser configuration was fabricated and characterized. Figure 5-11 shows a schematic representation of the all-fiber monolithic laser cavity which is similar to the system presented in Figure 5-9 with the addition of a narrowband low reflector (LR) FBG (30% reflective at 1063.7 nm with 0.2 nm FWHM bandwidth) written in an identical SMF (O/E land). The LR FBG is spliced to the output facet of the PCF with the goal to improve the laser spectral stability over time.

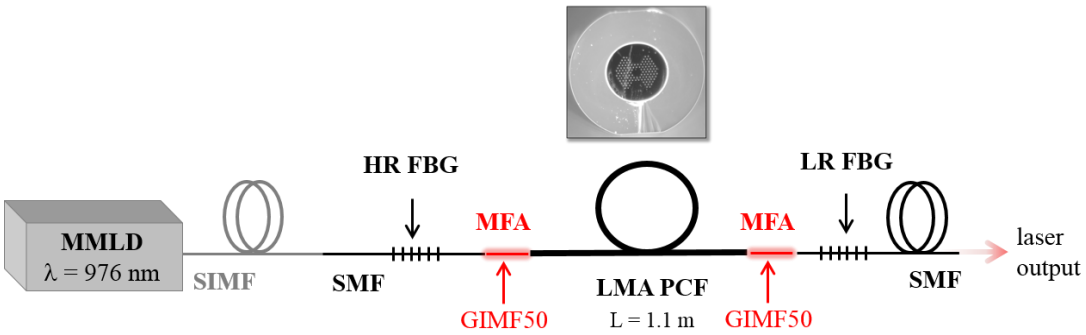

Figure 5-11: Schematic of the second monolithic fiber laser cavity including a pair of matched FBGs in SMF which are fusion spliced to both ends of the active LMA PCF. Locations of the two identical MFAs are indicated in red. The line-width of the laser emission is controlled using a narrow band LR FBG at the fiber laser output.

The output power has been measured for three fiber laser cavities using different SMF-to-PCF coupling configurations. Results obtained from the first configuration employing two identical MFAs made of the optimized GIMF50 length (250 μm) are presented in Figure 5-12. As the pump level increases, laser emission was characterized with a smaller slope efficiency than the previous configuration reported in Figure 5-10(a). The measured laser emission spectrum, displayed in Figure 5-12(b) shows a spectrally stabilized narrow-line laser emission at 1063.7 nm wavelength with an estimated 200 pm FWHM bandwidth, clearly indicating that the laser is initiated by the LR FBG feedback.

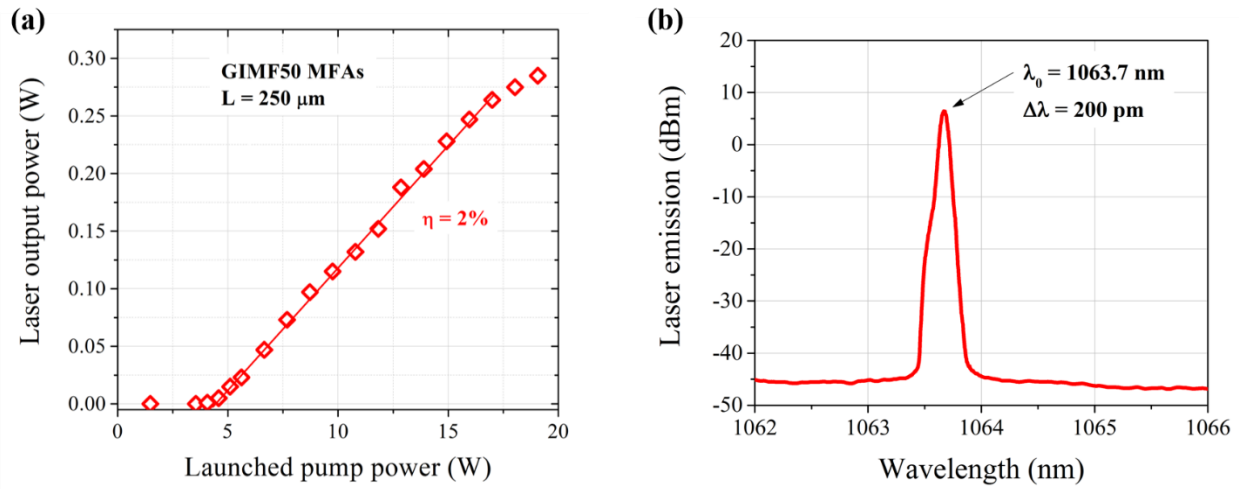

Figure 5-12: (a) Measured laser output power as function of launched pump power and (b) output spectrum measured from an all-fiber laser cavity employing two optimized MFA made of 250 μm of GIMF50.

These results were directly compared with two different monolithic fiber laser cavities: one directly splicing the FBGs to the PCF (no use of MFA) and one employing two identical but non-optimized MFAs made of 200 μm long segments of GIMF50. The power emerging these two cavities was recorded for various launched pump powers and results are summarized in Figure 5-13 in black and green respectively. When pumping the directly-coupled cavity, no hint of laser emission could be recorded indicating that losses (expected at the PCF interface) dominate, inhibiting any laser emission even at high pumping levels. On the other hand, when using non-optimized MFAs, a laser emission was recorded and characterized with a lower slope efficiency compared to the results obtained from the first "optimized" laser chain in Figure 5-12. A qualitative explanation is proposed to understand this trend using the findings presented in Figure 5-6(b). On this plot, the three chains previously mentioned are indicated with matching colored markers, i.e. red corresponding to 250 μm long segment of GIMF50, green to 200 μm and black attributed to direct-coupling. In the optimized MFA case, up to 92% overall transmission was predicted (in the ideal case of zero splice losses). In comparison, in the non-optimized case (200 μm long GIMF50),

the maximum obtainable transmission was 56% indicating significant coupling losses due to the mode-field mismatch. Without MFAs, only 5% of the light was expected to be transmitted. In other words, the light lost due to the mode-mismatch between the PCF and the SMF adds to the splicing losses at this junction. As a result, both effects contribute to inhibit the low (non-existent) laser performances shown in Figure 5-13. From a relative point of view, the MFA-optimized chain delivered the laser beam with the highest performances.

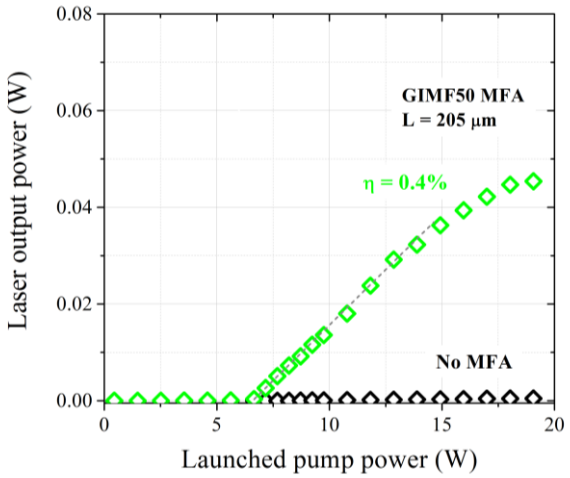

Figure 5-13: Measured laser output power as the pump light increases for a monolithic fiber cavity made with a pair of two identical 205 μm long GIMF50 MFAs (green) and without any MFAs (black).

5.5 Summary and outlook

After motivating the need for all-fiber integrated optical systems, novel MFA devices, using the periodic MMI propagating in GIMFs, were introduced as an attractive approach to mitigate the coupling losses arising from mode-mismatched optical fibers. The concept has been successfully demonstrated using the case of two mismatched SIFs and was further extended to mitigate the coupling losses between SMF and LMA PCF (estimated around 80%), presenting an initial eighteen-fold mode-field area mismatch. Results from numerical simulations enabled to

determine the optimum length of GIMF required to improve the chain transmission, predicting an overall transmission around 92% when using 250 μm segments of GIMF with 50 μm core in diameter. These numerical predictions were experimentally confirmed after measuring the transmission through a SMF-MFA-PCF-MFA-SMF resulting in ~11 dB improvement compared to the non-matched fiber chain across more than 100 nm bandwidth. This robust approach has been implemented to assemble the first monolithic fiber laser combining FBGs in SMF and active LMA PCF using all-fiber MFA devices. A few laser cavities have been assembled using different MFA configurations and their performances were compared. In each case, fiber lasers using MFAs outperformed lasers with direct SMF-to-PCF coupling. These results were recently published in peer-reviewed journal article [170].

This study opens the route towards the integration of LMA PCF in all monolithic fiber lasers using simple, robust scalable and cost-effective all-fiber devices compared to other complex and expensive methods. To give an outlook, several aspects could contribute to improve the measured laser performances. For example, by operating the laser at the gain maximum at 1030 nm, instead of forcing the laser emission at the FBG Bragg wavelength λ = 1065 nm which limited the obtainable slope efficiency and output power. In addition, cavity losses can be further mitigated by reducing the intra-cavity splicing loss. In particular, laser output performances could be further improved through better engineering of the cleaving process. Finally, it could be possible to tailor the GIMF design to scale the mode-field between the SMF and the LMA PCF, eventually reaching a "perfect" match with 100% light transmission.

CHAPTER 6: GAIN DYNAMICS AND TEMPORAL EFFECTS IN FIBER LASERS UTILIZING AN ACTIVE SPECIALTY MULTICORE FIBER

The last chapter of this dissertation is focused on developing a novel generation of monolithic fiber laser employing specialty gain fibers made of seven active cores. The motivation behind this study follows the growing interest of the scientific community in multicore waveguide structures which started a few decades ago with the first introduction of fiber bundles in the 80's Offering unmatched performances in terms of spatial and spectral resolution, fiber bundles were widely used in biomedical applications using confocal imaging [173] and multispectral imaging [174]. At the dawn of the 20th century, the evolution of the fiber fabrication techniques, enabling to create highly-controlled micro-structured fiber designs, strongly contributed to revive the research interest in Multi-Core Fibers (MCF). Since then, several MCF's have been demonstrated made of different designs and different material. One advantage of these structures compared to conventional single-core, step-index fibers is their high modularity resulting from the multiple configurations of core arrays achievable. Among the MCF designs, two main categories can be distinguished labeled isolated core MCF (IC-MCF) and coupled-core MCF (CC-MCF).

On one hand, isolated-cores IC-MCF designs were developed for applications requiring low-cross talk between the multiple cores forcing the light to propagate in each core independently from its neighbors. IC-MCF designs are preferred for efficient data transmission [89], [176], mode-division multiplexing [177], multi-channel amplification in fiber amplifier [178] and recently power scaling in fiber lasers beyond the current onset of modal instability [125].

On the other hand, in CC-MCFs designed with small pitch values Λ, light guided in one core evanescently couples back and forth with the neighboring cores resulting in the formation and propagation of eigensolutions called supermodes. Each guided supermode is a linear superposition of the *LP* modes guided in individual cores. A direct analogy can be done between CC-MCFs and MMFs as several transverse modes exist and propagate simultaneously. In both fibers, the phenomenon of Multi-Mode Interference (MMI), introduced in Section 2.3, occur during light propagation. MMI in MMFs has found many applications to date including the MMI-based fiber devices previously listed in Section 2.3 [43]–[47] as well as recent emerging such as mode-division multiplexing [179], tunable lasers [180] and power scaling of fiber laser [181].

To date, the concept of MMI has been widely studied in step-index and graded index Multi-Mode Fibers (MMF). In comparison, CC-MCFs, which are also MMI devices, offer a significant flexibility in terms of inner fiber design. By controlling the number of coupled-core, their sizes and relative organization, the variety of achievable configurations is considerably expanded. As a direct consequence, tailoring the design of CC-MCF is a resourceful field of research with the unique potential to outperform existing MMFs used in current MMI-based fiber devices and the ability to further discover novel applications.

Output beams from MM fiber laser generally suffer from spatial and temporal instabilities due to the propagation and amplification of several transverse mode.

CC-MCF have been used as a few-modes devices in mode-division multiplexing [177], [182] multiplexing. Also, a very recent study demonstrated that CC-MCFs can be used as sensing devices with enhanced sensitivity [183]. But the core of the research to develop novel CC-MCF relies on the ability to access information on the guided supermode content, related propagation properties and dependence on the inter-core coupling. Several numerical studies were reported to

study for example the supermode formation in multi-core PCFs [184] and the mode-coupling analysis when designing trench-assisted MCF [175]. One particularly interesting property has been widely studied in CC-MCF. Due to the self-organization in two-dimensions arrays [185], the lowest order supermode propagating is called the in-phase supermode and exhibits a characteristic diffraction limited far-field profile. This discovery and the potential to generate high brightness beams [24], [186] has motivated the scientific interest to study methods to select the in-phase supermode such as phase-locking [187], Talbot cavities in MCF lasers [188], [189], structured output couplers [190], external waveguides [191], [192] and self-Fourier resonators [193]. Additional applications such as beam shaping [190] were also demonstrated. Also, modal selection and phase control have been the most successful approach demonstrated to stabilize the output of MMF laser cavities [194], [195]. One of the main drawbacks is the use of external free-space elements to achieve efficient mode selection in CC-MCFs. In this case, not only the monolithic advantage of using a single fiber device containing multiple cores is lost but the overall stability of the systems suffers from the very complex optical alignment with several micro-sized cores.

However, the major consequence of achieving strict supermode selection is that the real potential offered by CC-MCF lasers remains currently unknown. Even though a few numerical studies have been reported aiming to uncover the physics behind multi-supermode amplification[196], [197] and coupled-mode theory in laser systems [198], [199], the lack of experimental demonstration is currently the main bottle-neck for the further development of MCF lasers since complex inter-mode coupling and competition mechanisms during light amplification are, to date, not fully understood.

Here, the results of the complete characterization of a multi-supermode CC-MCF laser including mode competition, lasing dynamics and temporal effects are presented in details. First

of all, the active 7-coupled-cores fiber is introduced in Section 6.1. An analytical model to predict light transmission in this CC-MCF is detailed in Section 6.2. Then, an experiment is presented in Section 6.3 to measure (a) the supermode content in the CC-MCF and (b) the gain of individual supermodes amplified in the CC-MCF. These results are discussed in details in this dissertation and represent, to date, the first experimental demonstration of gain competition between supermodes. In Section 6.4, an experiment to measure the laser dynamics in the CC-MCF is introduced using a fully monolithic fiber laser cavity. Finally, the first observation of self-mode locking generated in a linear MCF laser cavity is demonstrated in Section 6.5. This chapter in concluded in Section 6.6 summarizing the main findings and give future outlook.

6.1 Introduction and characterization of the active multi-core fiber (MCF)

The fiber used in this chapter is the product of a collaboration with the Institute of Photonics Technology (IPHT) in Jena, Germany who designed and fabricated the CC-MCF. It is important to note that the REPUSIL fabrication technique, recently introduced, has been used to fabricate this fiber [200]. This approach is based on the sintering and vitrification of doped powders and has been demonstrated to overpass the current limitations of MCVD when fabricating very Large-Mode-Area fibers. In the following, the label CC-MCF will be changed to MCF for simplicity.

The MCF is made of 7-cores uniformly doped with Ytterbium (Yb) atoms (~$4.5.10^{25}$ Yb^{3+}/m^3) embedded in an all-solid Fused Silica matrix. The dimensions of the micro-structures have been extracted using an image of the MCF facet recorded with a microscope and illustrated in Figure 6-1(a). The diameter of each Yb-doped core (light grey) was measured to be 5.9 μm ($\pm$ 0.1) in average and the core-to-core separation, also called pitch Λ, was 9.3 μm ($\pm$ 0.2) in average. The hexagonal cladding geometry has been intentionally designed to improve the pump absorption

during cladding pumping. The MCF outer diameter (OD) is 125 μm (along the long diagonal of the hexagon) offering a good compatibility for fusion splicing with conventional fibers with same OD. Also, reproducible and reliable cleaving and splicing can be achieved with standard fiber equipment due to the all-solid fiber geometry.

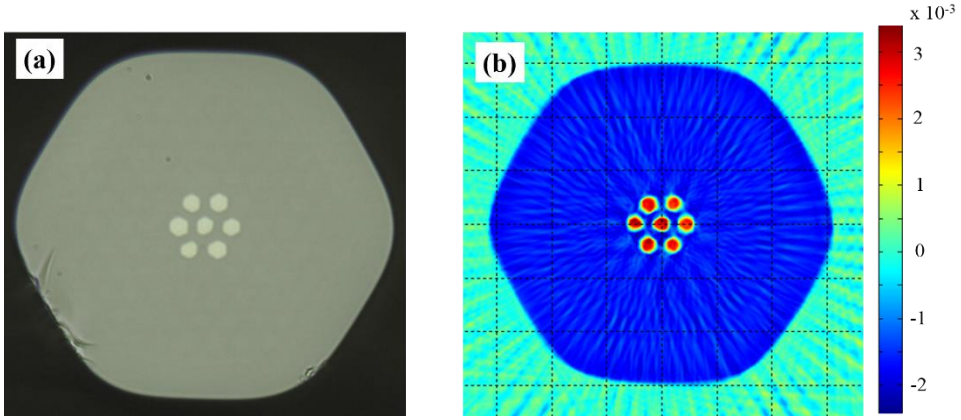

Figure 6-1: (a) Microscope image of the active 7-cores fiber (b) 2D measurement of the MCF refractive index profile.

The refractive index distribution across the MCF facet has been measured with the profilometer introduced in Section 3.4.1 (from Interfiber Analysis) and results are presented in Figure 6-1(b) using light at λ = 633 nm wavelength. The 7 Yb-doped cores (red) and the solid fused silica cladding (blue) show a good material uniformity. In addition, the refractive index differences between each fiber layer and the surrounding (green) were measured to be $\Delta n \sim 3.10^{-3}$ and $\Delta n \sim 2.10^{-3}$ in the core and cladding respectively. This measurement has been repeated for several light wavelength ranging from 0.5 μm to 1 μm. The measured values of core and cladding refractive indices are plotted as function of the measurement wavelength in Figure 6-2 using red and black markers respectively. Following the procedure described in Section 3.4.1, the fiber dispersion in the core and cladding has been interpolated and plotted using red and black curve in Figure 6-2 respectively. The numerical aperture of each individual cores has been calculated using

equation (20) and is also represented in Figure 6-2 using the blue line indicating an almost constant value around ~0.095.

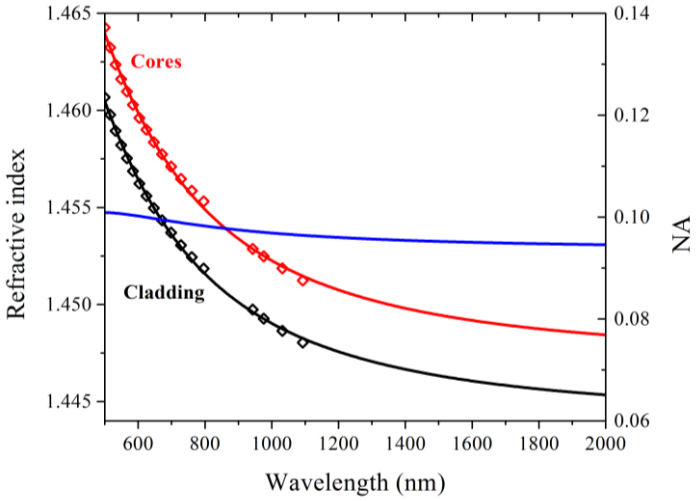

Figure 6-2: Measured refractive indices in the core and cladding layers of the MCF (red and black markers respectively) and extrapolation of the core and cladding dispersion relation after applying a Cauchy fitting function. The blue line corresponds to the calculated numerical aperture of individual cores.

The measured MCF dimensions and indices are imported in a fiber mode solver (Fimmwave by Photon Design) which solves the guided modes using a vectorial finite element method. Calculations were carried at the wavelength corresponding to the maximum gain of the Yb atoms, i.e. λ = 1.03 μm. Results are presented in Figure 6-3(a) to (g) showing the field distribution of 7 supermodes, labeled SM_i, with n = 1,…,7. The value of the fiber V-parameter (Equation (19)) can be calculated using the measured MCF core diameter and the NA measured in Figure 6-2. The measured MCF V-parameter is ~1.67 indicating that the condition for single-mode guidance is achieved in each core of the MCF which confirms the existence of 7 non-degenerated supermodes. The first supermode (SM_1 in Figure 6-3(a)) is the so-called in-phase supermode where all the cores emit in-phase. The corresponding far-field profile is diffraction limited.

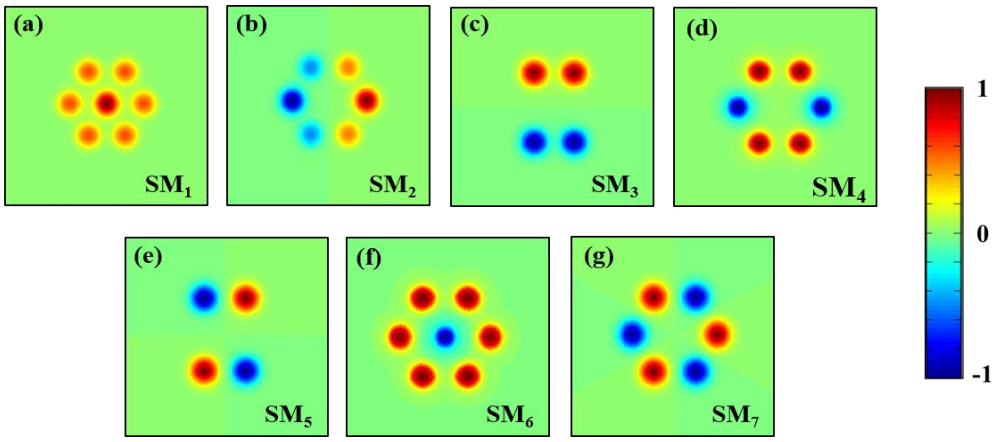

Figure 6-3: Normalized field distributions of the supermodes guided in the 7-cores MCF calculated at a light wavelength of λ = 1.03 μm.

During light propagation in the MCF, several supermodes are guided leading to the formation of MMI. This phenomenon has been introduced in details in Section 2.3 and is characterized by an oscillatory response with periodicity defined in Equation (34). The wavelength and length dependence of the MMI period has been measured in the MCF using a straightforward light transmission experiment. A monolithic fiber chain including a Single-Mode Fiber (SMF), a piece of MCF and a second segment SMF has been assembled using standard fusion splicing techniques (Ericsson). The selected SMF is a single-core, step-index fiber with 5.8 μm core diameter and 125 μm OD. It was chosen (a) to be single-mode at the wavelength of interest i.e. λ = 1.03 μm, (b) to be well-matched to individual cores of the MCF, and (c) because it is used in most fiber-based components. Robust fusion splices SMF-to-MCF were achieved with less than 0.5 dB insertion losses. Before recording the light transmitted by the fiber chain SMF-MCF-SMF, particular attention must be paid regarding the in-coupling mode overlap between the SMF and the MCF which will determine the combination of guided supermodes (see Section 2.4.1). Thus, in order to obtain reproducible performances of MCF-based systems, the alignment in SMF-to-MCF splices must be achieved very carefully and must be systematically reproducible.

Several fusion spliced SMF-to-MCF segments have been measured with the profilometer around the splice location. An example is presented in Figure 6-4 showing a microscope view of the SMF-MCF fiber chain (the interference fringes are used to measure the refractive indices) and 2D index profiles measured at several locations along the splice (separated by 10 μm). The result is a unique 3D measurement of the refractive index profile across a fiber splice.

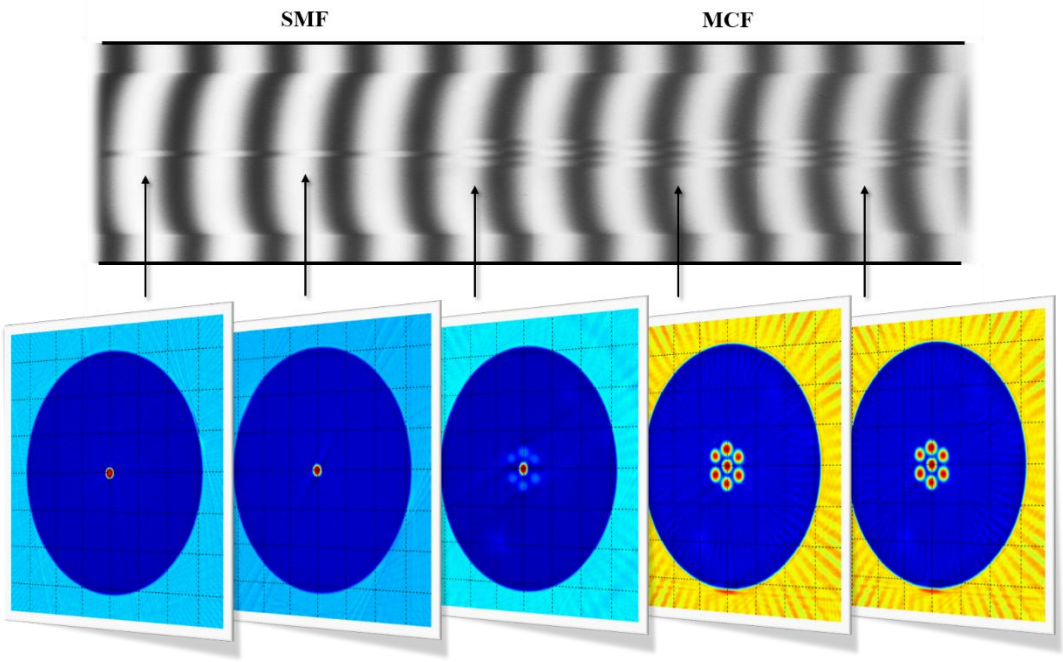

Figure 6-4: Profilometer measurement through a SMF-to-MCF fusion splice. To facilitate the comparison, a MCF with circular cladding geometry was employed. Both circular and hexagonal MCF geometries have been fabricated using the exact same material components.

Two main information can be extracted: (a) the spatial evolution of the refractive index profiles through a splice and (b) the relative fiber alignment after splicing. The 3D profilometer measurement shows a good overlap between the SMF core and the MCF center core within an accuracy of $\pm$ 2.μm (limited by the transverse resolution of the profilometer) which confirms the reproducibility of the SMF-to-MCF alignment during splicing. In addition, two relevant comments can be done regarding Figure 6-4. First, the color scale differs between each 2D profile and can

only be considered for esthetic purposes. Second, the same procedure was employed to validate center and robust splicing between the SMF and the hexagonal MCF of interest.

A fiber-coupled broadband light source emitting around 1.06 μm wavelength (superluminescent diode by Thorlabs) was used to excite the modes in the MCF. The transmission of the chain SMF-MCF-SMF was measured with an OSA. Results are presented in Figure 6-5(a) for different length of the MCF varying between 1m long to few cm long. As expected, a periodic and contrasted spectral modulation (average depth is ~10 dB), characteristic of the MMI between the transverse modes, was measured. The overall envelope of the transmission measurement is dictated by the emission spectrum of the source. The MMI period has been measured and plotted for several MCF lengths. Results are represented in Figure 6-4(b) (blue dots) and compared with calculation results (grey line) obtained after simulating the fiber chain using different length of MCF with Fimmwave (PhotonDesign). The good agreement between experiment and simulation emphasizes the accuracy of the measured fiber inner dimensions and refractive indices and shows a good understanding of the SMF-to-MCF coupling.

To complete the characterization of the MCF, the absorption during cladding pumping has been measured using a multi-mode pump diode emitting at 976 nm light wavelength. The cladding absorption was found to be 1.6 m^{-1} ($\pm$ 0.1m^{-1}) corresponding to a minimum length of MCF around L ~60 cm to guaranty an efficient absorption of the pump light towards laser emission.

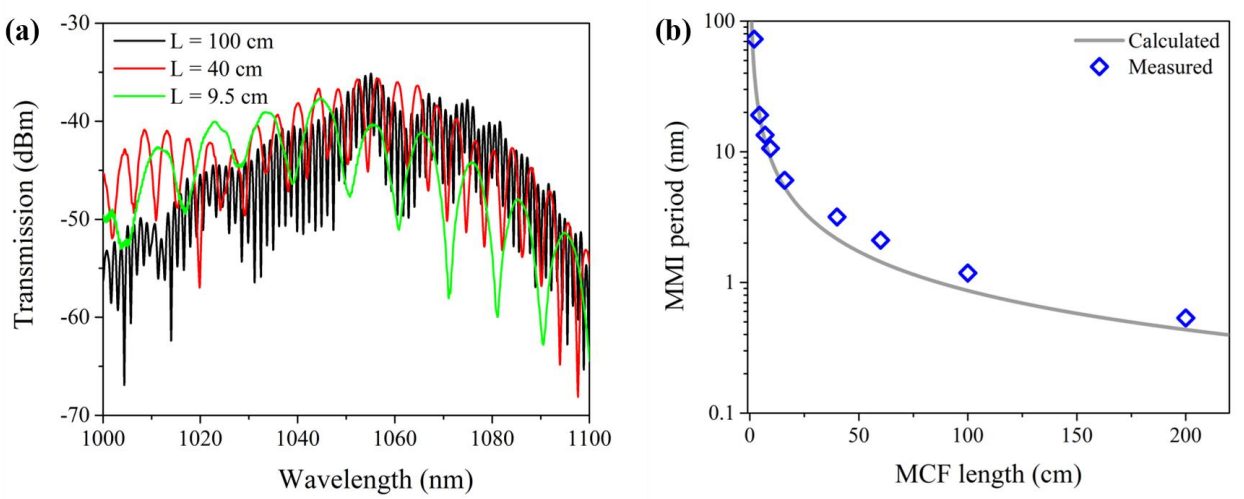

Figure 6-5: (a) measured MMI transmission through a SMF-MCF-SMF fusion spliced chain for several MCF lengths. (b) Measured MMI period as function of MCF length (blue) compared to simulation results (grey line). Results are plotted using a dB scale for clarity purposes and show a good overlap.

6.2 Light transmission in MCF: analytical model

The periodic oscillation of the MMI pattern measured in Figure 6-4 indicates that only a few supermodes are excited and propagate in the MCF (see details in Appendix A & B). In order to predict the corresponding combination of guided supermodes, an analytical model based on the coupled mode theory [201] is presented in details in this section. Details regarding the calculation steps can be found in Appendix C while only the main results are presented in the following.

Assuming that the incident light is coupled in the center core of the MCF using a perfectly matched SMF, only supermodes with non-zero intensity in the center core i.e. the supermodes overlapping with the SMF core, can be excited. When collecting the light emerging the MCF with a segment of SMF, the total transmission was be calculated to be (Appendix C):

$$T(\nu) = 1 - 4P_1P_6\sin^2(\phi_0 + 2\pi\tau_0\nu) \qquad (48)$$

with ν the light frequency, ϕ_0 the phase term and τ_0 the intermodal delay which can be expressed as

$$\phi_0 = 2\sqrt{7}\tilde{c}(\nu_0)L - 2\sqrt{7}\widetilde{c_1}\nu_0 L \quad (49)$$

$$\tau_0 = \frac{\sqrt{7}}{\pi}\widetilde{c_1}L. \quad (50)$$

In addition, P_1 and P_6 correspond to the intensity in SM_1 and SM_6 respectively, the two supermodes in the MCF with non-zero intensity in the center core (profiles (a) and (f) shown in Figure 6-3). According to the model (Appendix C), values of P_1 and P_6 were calculated to be ~30% and ~70% respectively. In Equation (49) and (50), $\tilde{c}$ stands for the overall coupling coefficient in the MCF while the coefficient $\widetilde{c_1}$, with units of time over length, can be assigned as the Differential Group Delay (DGD) between the two guided supermodes SM_1 and SM_6. Also, $\widetilde{c_1}$ can be directly calculated from the derivative of $\tilde{c}$ with respect to the frequency ν. Results from calculations performed at λ = 1.06 μm light wavelength (corresponds to a frequency of ν_0 = 281.76 THz) are shown later in Figure 6-7.

The coefficient $\widetilde{c_1}$ can be experimentally evaluated. To do so, the transmission through a 90 cm long segment of MCF, fusion spliced with two pieces of SMF, has been recorded using the SLD and results are shown in Figure 6-6(a), plotted as function of the light frequency. The Fourier transform of the periodic transmission has been calculated and results are presented in Figure 6-6(b) as function of the DGD also labeled $\widetilde{c_1}$. In the Fourier transform, a peak can be resolved at 2.2 ps/m < $\widetilde{c_1}$ < 2.5 ps/m, interval defined at the FWHM of the peak. The fact that only one peak could be measured in the Fourier spectrum indicate that only two supermodes are in practice guided in the MCF.

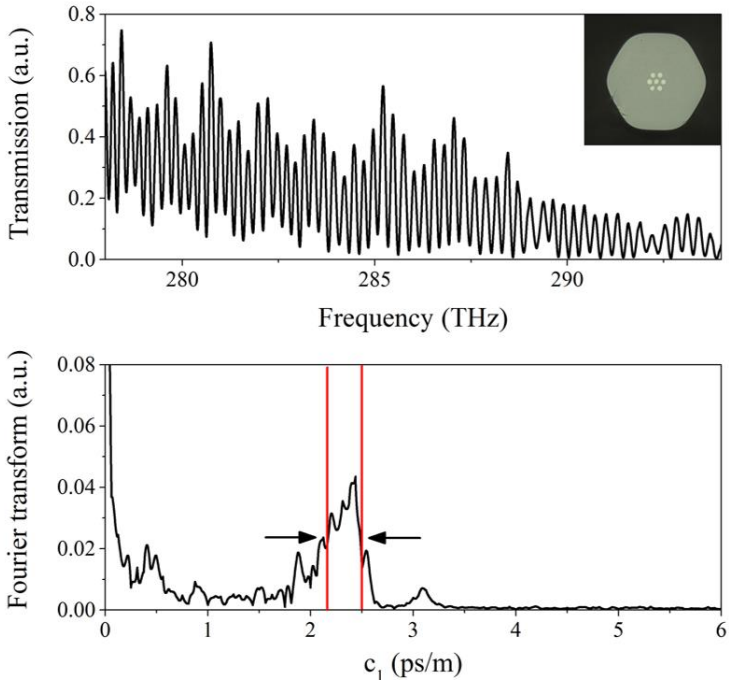

Figure 6-6 (a) Light transmission measured after a chain SMF-MCF-SMF showing the periodic MMI response. (b) Fourier transform calculated from the measured transmission and plotted as function of the intermodal coupling coefficient $\tilde{c_1}$. The maxima corresponding to the two interfering supermodes is indicated by the red interval at the peak FWHM.

Experimentally measured values of the coefficient $\tilde{c_1}$ are directly compared with analytical calculations in Figure 6-7. In the plot showing the values of $\tilde{c_1}$ for various fiber pitch, the grey-shaded area corresponds to the range of the experiment i.e. MCF pitch values Λ = 9.3 μm ($\pm$ 0.2) from Section 6.1 and 2.2 ps/m < $\tilde{c_1}$ < 2.5 ps/m, previously determined in Figure 6-6. Results in Figure 6-7 show a good overlap between experimental and analytical values of the coefficient $\tilde{c_1}$. As a result, around λ = 1.06 μm light wavelength, SM_1 and SM_6 are expected to propagate in the MCF with both ends spliced to SMF.

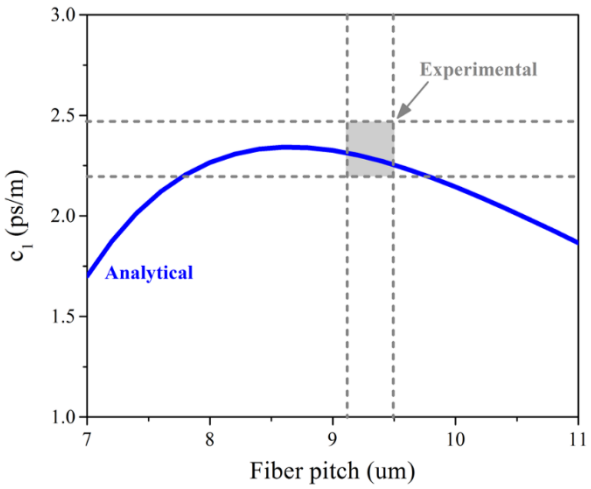

Figure 6-7: Comparison between analytical calculations and experimental determination of the coefficient $\tilde{c_1}$, also called Differential Group Delay (DGD).

However, it is important to moderate these finding since, in the real experimental world, optical systems are subject to environmental fluctuations which are generally not considered when developing an analytical model based on perfect conditions. For example, a second peak appears on the Fourier spectrum in Figure 6-6(b) for $\tilde{c_1} \approx 3.1$ ps/m, indicating that a third residual supermodes is most likely guided in the MCF. There are several potential explanations to the discrepancy with the analytical model predicting only 2 supermodes;

- The fact that the input coupling between the SMF and the MCF center core depends not only on the alignment during splicing, but also on the fact that the relative size and NA between the two fibers which slightly differ which might result in a small amount of light being coupled in additional supermodes.
- The very long interaction length of the MCF (~90 cm), increases the probability that external perturbations such as coil, twist or air fluctuation might perturb the guided light in the MCF. As a result, residual inter-mode coupling may occur.

6.3 Mode-resolved gain analysis and lasing operation in monolithic MCF lasers

The goal of the following Sections 6.3 and 6.4 was to utilize the multi-mode system in the MCF to investigate the dynamic mechanisms during multi-supermode lasing operation. Compared to analog standard MMF systems [181], [194], [195], using MCFs in laser systems gives access to more degrees of freedom, allowing a better control on the combinations of guided modes. However, mechanisms of intermodal coupling between supermodes and mode competition are complex in MCF and not fully characterized, currently limiting the potential of these MMI systems.

6.3.1 Experimental setup

An experiment to achieve gain-resolved mode analysis is schematically presented in Figure 6-8. The selected decomposition technique was the Correlation Filter Method (CFM), previously detailed in Section 3.3. In the present experiment, CFM has been selected among other mode analysis techniques (listed in Section 3.1) for its ability to spatially decompose the transmission functions of each guided modes with a Computer Generated Hologram (CGH) and for its capabilities to decompose highly multi-mode beams in real-time. For the present investigation, a CGH device, well-matched to the active MCF, previously characterized (Section 6.1), was fabricated and provided by D. Flamm and M. Duparré (FSU, Jena, Germany). This CGH was designed to decomposed the modal amplitude of the 7-guided supermodes in the MCF around λ = 1060 nm. The corresponding theoretical mode profiles were presented in Figure 6-3.

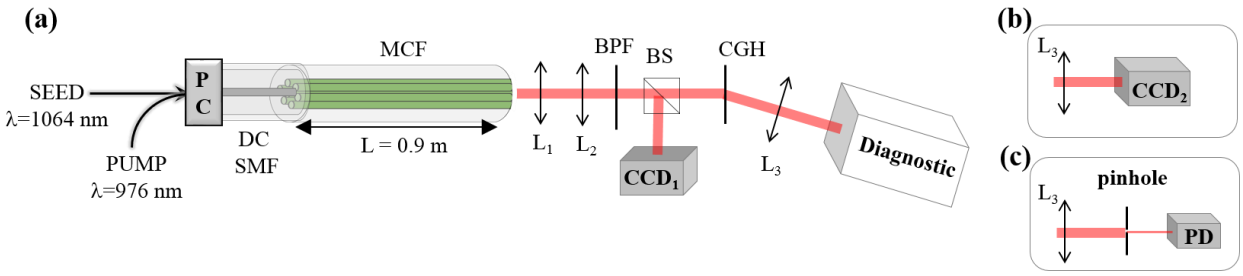

Figure 6-8: (a) Mode-resolved gain experiment with PC: pump combiner; DC SMF: double-clad single-mode fiber, L_1 and L_2 aligned in a *4f*-system with magnification factor of 75; BPF: band-pass filter; BS: beam splitter; CGH: computer generated hologram; L_3 the imaging lens. Two diagnostics were used: (b) L_3 in combination with CCD_2 to perform CFM and (c) L_3 followed by a pinhole with 200 μm diameter and PD: photodetector to perform mode-resolved gain analysis.

A fiber-based multi-mode pump combiner (PC) is employed to couple either or both seed light (a narrow-line laser emitting at 1064 nm) and pump light (a multi-mode laser diode at 976 nm). The seed light is coupled via the signal port made from a matching SMF (core diameter of 5.8 μm) with double-cladding geometry (1st cladding is 105 μm in diameter and OD is 125 μm) while the pump light is delivered in a MMF with 105 μm core diameter and 125 μm OD. The DC SMF is fusion spliced to the 90 cm long active MCF segment characterized in Sections 6.1 and 6.2. The MCF has been previously uncoated to avoid pump scattering and has been inserted in a fused silica capillary to be kept straight and isolated from external fluctuations. The output end of the MCF is flat cleaved and the emerging near-field is imaged on the plane of the CGH and of the CCD using a beam splitter (BS). The 4f-imaging scheme has been carefully chosen (L_1 is a 40x microscope objective and L_2 has 300 mm focal length) to ensure the proper magnification factor (M = 75) between the MCF and the CGH. The CFM diagnostic assembled on the right hand side of Figure 6-8 to perform mode decomposition has been introduced in details in Section 3.3. A few modifications from the original measurement have been made here;

- A bandpass filter for wavelengths around λ = 1064 nm ($\Delta\lambda$ 10 nm) has been inserted in the beam before the CGH in order to select the seed light and to block the residual pump.
- In the original CFM, the far-field from the CGH is imaged on a CCD which records all the correlation answers imaged on different pixels (Figure 3-13). Here, a pinhole is used after the CGH in parallel with a photodetector (PD) to measure the amplitude of the signal at selected correlation answers (the pinhole acts as a CCD pixel).

6.3.2 Mode-resolved gain analysis

Two cases are investigated in this section starting with the unperturbed MCF followed by the analysis of the perturbed MCF via coil and transverse stress.

6.3.2.1 Unperturbed MCF

The experiment was initiated by performing an analysis of the supermodes guided in the MCF using the light from the seed laser (pump off). To do so, the diagnostic shown in Figure 6-8(b), using a CCD to record the correlation answers, following the conventional scheme used for CFM (Section 3.3) was used.CFM was performed and the mode power (MP) values ρ_n^2 of each supermode SM_n propagating through the 90 cm segment of MCF were measured and results are plotted in Figure 6-9. As a result, the mode power values $\rho^2(SM_1)$ = 26% and $\rho^2(SM_6)$ = 31% were extracted. Even though these values differ from the analytical predictions Section 6.2, two guided supermodes could clearly be identified. The corresponding MCF near field has been recorded with the CCD_1 and is shown in Figure 6-9. For each CFM measurement performed in this section, the standard deviation has been calculated by comparing an average of 20

measurement with 200 measurements (total recording time was ~1 min). The result gives an indication of the measurement stability over time and is represented by the black line in each of the following bar-diagram. Even though the measurement presented an overall good stability (Figure 6-9), it is important to note that a non-negligible amount of power, was measured in other supermodes with $\rho^2(SM_5)$ = 10% and $\rho^2(SM_7)$ = 15 %. These findings confirm the observations made in Section 6.2, where a hint of additional propagating supermodes, other than SM_1 and SM_6, was measured around $\tilde{c_1} \approx$ 3.1 ps/m on the Fourier spectrum in Figure 6-6(b).

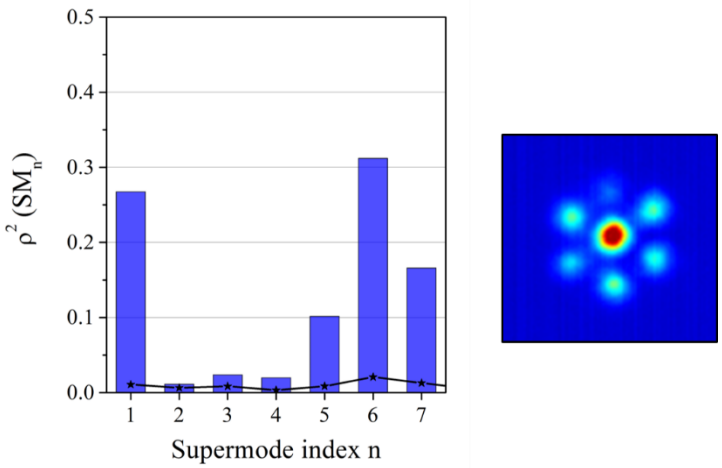

Figure 6-9: Modal decomposition after propagation of the seed laser (λ = 1064 nm) and corresponding near-field emerging the MCF. The pump is OFF during this measurement. The standard deviation is represented using the black line.

Then, the second part of this experiment consists in the measurement of the optical gain carried by individual supermopdes. To do so, a pinhole (200 μm in diameter) was inserted after the far-field imaging lens L_3 (Figure 6-8(c)) and carefully aligned on one modal correlation answer while monitoring with the CCD. Using a PD, the power was measured at a selected correlation answer was measured for increasing pump power (while remaining below the laser threshold) while the seed power remained constant. From this measurement, the gain factor γ_n of the

amplified supermode SM_n, defined as the ratio of the seed power between pump ON (P^{ON}) and pump OFF (P^{OFF}) such that

$$\gamma = 10 \times log\left(\frac{P^{ON}}{P^{OFF}}\right) \quad (51)$$

were measured. Results are shown in Figure 6-10 where γ_1 and γ_6 (the mode-resolved gain factor measured after filtering the correlation answer of SM_1 and SM_6 respectively) were measured as function of the pump power. According to the measurements, $\gamma_1 \neq \gamma_6$ indicating that, under the same pumping conditions, SM_1 is preferably amplified compared to SM_6, even though $\rho^2(SM_6)$ > $\rho^2(SM_1)$ when passive light (λ = 1064 nm) propagates in the MCF (see Figure 6-9). At 3.3 W pumping level, γ_1= 12 dB and the gain factor of SM_1 is 2 dB higher thanSM_6.

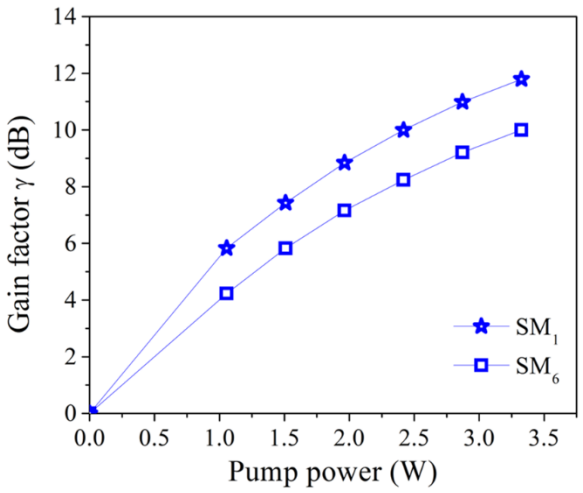

Figure 6-10: Measured gain factor γ_n of individual supermodes SM_nas function of the pump power.

To confirm this measurement, a second CFM analysis was performed (using the far-field imaged on the CDD Figure 6-8(b)) at a fixed pump power of 3.3 W. Results are plotted in Figure 6-11 showing that $\rho^2(SM_1)$> $\rho^2(SM_6)$. This confirms that SM_1 has a higher gain factor compared to SM_6 with $\rho^2(SM_1)$ = 40 % while $\rho^2(SM_6)$ = 25% The corresponding amplified seed profile

recorded at 3.3W pump level with CCD_1 is shown in Figure 6-11. The good radial uniformity is consistent with the dominant SM_1. This procedure can easily be extended to investigate gain dynamics during amplification in most multi-mode fiber amplifiers.

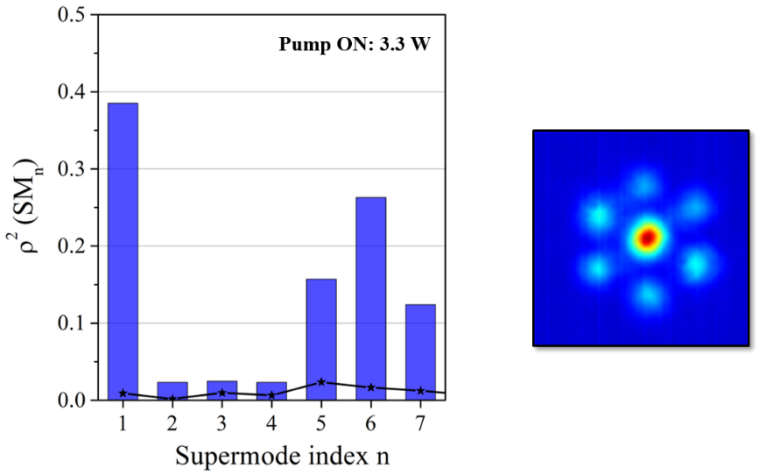

Figure 6-11: Mode analysis of the seed when amplified using 3.3. W of pump power. The ear-field of the beam emerging the MCF and measured with CCD_1 is included.

6.3.2.2 Perturbed MCF

The relative values of $\rho^2(SM_5)$ and $\rho^2(SM_7)$ shown in Figure 6-11 did not change considerably under pump amplification. However, their relatively low MP values (ρ^2 ~10%) did not allow to accurately align the pinhole at the correlation answer and no gain factor could be measured. In this paragraph, the MCF has been intentionally perturbed in order to excite different combinations of supermodes. The goal was to evaluate the influence of the external environment, critical source of fluctuations in multi-mode fiber amplifiers, on the gain distribution and later on the stability of the emission.

The gain factor measurement has been repeated after inducing first localized bending and then transverse stress on the 90 cm long MCF segment. In each case, the supermodes have been

decomposed (pump OFF using the CFM method shown in Figure 6-8(b)) and the beam emerging the MCF was monitored on CCD_1. Results are summarized in Figure 6-12(a) and (b) respectively. The distortions visible on the measured beam profiles indicate a higher supermode mixture guided in the MCF due to the external perturbations. This is verified with the MP measurements showing that $\rho^2(SM_7)$ = 25% is dominant when a coil perturbation is applied to the MCF while ~40% of the remaining power is distributed among SM_1 and SM_6 (Figure 6-12(a)).

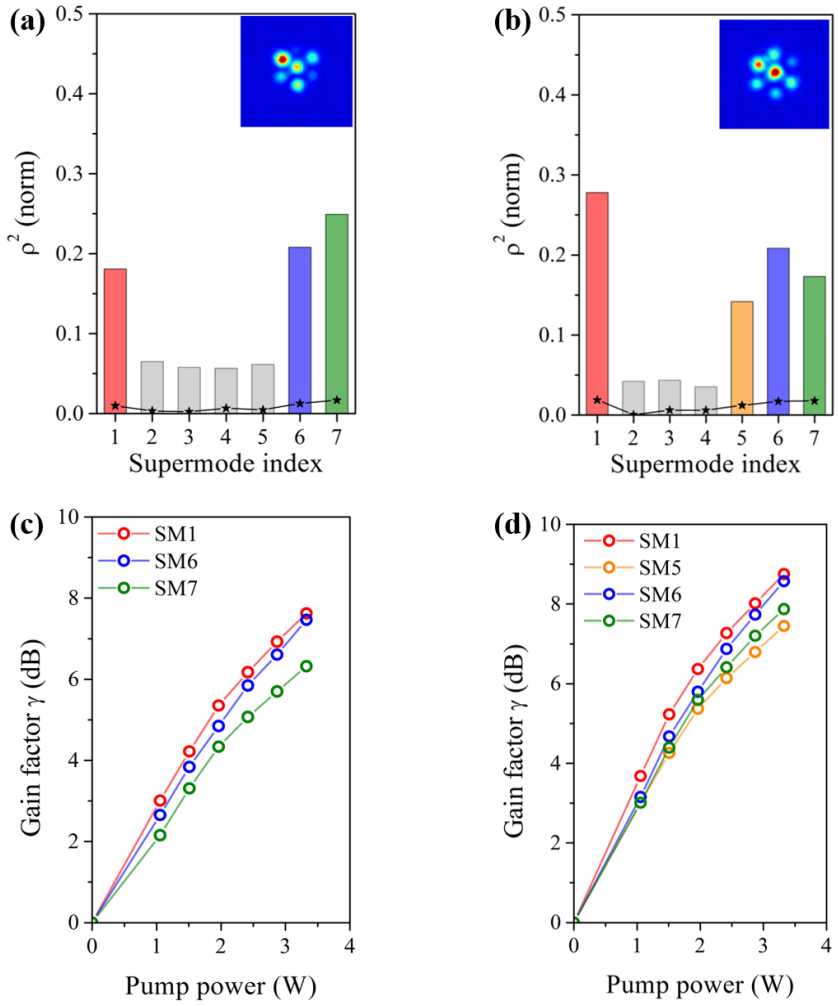

Figure 6-12: (a)&(b): Mode analysis of the seed laser propagating in the MCF (pump OFF) which is first bent and then experiences transverse stress respectively. (c)&(d): Measured gain factor in the excited supermodes as function of pump power corresponding to the cases where the MCF is first bent and then experiences transverse stress.

Further perturbing the MCF applying transverse stress (Figure 6-12(b)) results in a relatively uniform distribution of the power among several supermodes (apparition of SM_5).The overall measurement stability is worth noting even after perturbation. Grey bars indicate supermodes carrying a MP too low to allow gain factor measurement.

In each MCF situation, the gain factor γ_n was measured for the supermodes represented by the colored bars in Figure 6-12(a) and (b) and plotted as function of pump power. Results are shown in Figure 6-12(c) and (d) using a matching color code. According to the measurement, SM_1 has the highest gain factor (γ_1 = 7.6 dB and 8.7 dB) followed by SM_6 (γ_6 = 7.4 dB and 8.5 dB), regardless of the external perturbation applied to the MCF. Furthermore, it can be noted that, as the pump power increases, no gain-crossing was measured between the supermodes. As a result, two main observations can be done:

- The measured amplified mode content significantly differs from the passive mode combination guided in a multi-mode fiber device.
- The gain distribution among the supermodes is not influenced by the external perturbations applied on the MCF ($\gamma_1 > \gamma_6$).

These results indicate that the combination of amplified modes is defined by the gain profile of the MCF. In comparison, the combination of guided modes (passive light propagation) depends on the physical core-cladding boundaries.

In conclusion, using a first-of-a-kind experiment, the gain factor in individual supermodes was measured. From the results, it is clear that, in order to investigate fiber laser dynamics, the mode analysis should be performed not only in an active fiber (taking into account the gain profile), but most importantly during laser emission (or light amplification) since the gain distribution in a multi-mode system might be mode-dependent.

However, to date, even though the number of published studies reporting modal decomposition in specialty fibers keeps increasing, most mode analysis have been performed in passive fibers [87], [89], [92], [116] or in active fiber using passive seeding light sources [202]. The following section provides more details on the current limitation and proposes the first results of supermode analysis during laser emission of a monolithic MCF laser.

6.4 Real-time decomposition of lasing supermodes

The design of active specialty fibers used as gain medium in laser cavities is tailored according to the targeted output performances. One striking example is the use of LMA fiber designs to achieve power scaling [90], [120], [203]. When developing novel specialty fibers, tools to measure individual lasing modes and their dynamics during laser operation could directly contribute to finely tune the fiber design to improve the output performances and uncover the lasing modes dynamics in few-modes fiber lasers.

However, to date, only a few approaches to measure the transverse modes during laser emission were reported. For example, a method using a fiber Bragg grating inscribed in an active few-modes fiber in combination with a spectral grating to disperse the transverse modes has been demonstrated [204]. However, this approach is limited to active fibers guiding only a few non-degenerated modes. In addition, it does not allow for a direct reading of the individual MP values and provides no information regarding the modal phases. A second method required the use of high speed cameras which represent a considerable financial investment [86]. In addition, most of the mode analysis techniques detailed in Section 3.1 cannot be implemented to study lasing modes. For example, S^2 imaging can only measure the modes in laser beams of few tens of nanometers of

bandwidth [77] or emitting narrow line-width and tunable emission [93] and requires a time consuming post-data processing.

The most promising technique is CFM, capable to accurately decompose a wide variety of narrow line-width laser beams including highly multi-mode beams and offering a real-time reading of the MP values ρ_n^2, of the intermodal phases ϕ_n and the ability to reconstruct the total beam in real-time [79]. In the following section, results of the first supermode decomposition during laser emission in a monolithic MCF laser cavity are presented using CFM analysis. This approach can be generalized to evaluate any multi-mode fiber laser beam.

6.4.1 Experimental setup and in-depth laser characterization

A schematic of the complete experiment is presented in Figure 6-13. It can be decomposed in two main sections: the MCF laser and the mode analysis diagnostic. The monolithic fiber laser is similar to the amplifier system previously detailed in Figure 6-8 except that the PC was replaced by a fusion spliced fiber chain made with the MMF delivering the pump light, a fiber Bragg grating (FBG) written in SMF, and the 90 cm long segment of Yb-doped 7-cores fiber. The FBG is highly-reflective (HR FBG with R = 99.7%) at the Bragg wavelength λ = 1029.65 nm across a spectral bandwidth of $\Delta\lambda$=162 pm. Also, a residual pump (RP) filter (long pass at λ = 1 μm) was used to block more than 98% of the residual pump. The cavity was formed between the HR FBG and the flat cleaved MCF. While the HR FBG provides a selective feedback to the MCF center core, and the Fresnel reflection at the MCF flat cleave is uniform among all the cores.

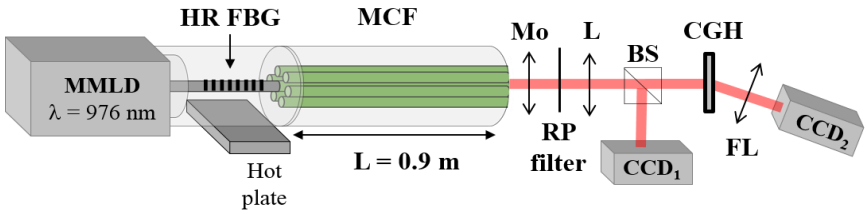

Figure 6-13: Schematic of the monolithic MCF laser formed by a HR FBG in SMF and the flat cleaved MCF facet in a cladding pumped configuration using a MMLD. The CFM diagnostic is identical to Figure 6-8(a) and (b). A residual pump (RP) filter replaced the BP.

Prior to discuss the lasing modes analysis results, the laser cavity is qualitatively described using the passive characterization of the MCF presented in Section 6.1. A zoomed-in section of the passive transmission measurement presented in Figure 6-5(a) is shown in Figure 6-14. After propagation through the 90 cm long segment of MCF fusion spliced with the SMF, the period of the MMI pattern is $\Delta\lambda$ = 1 nm $\pm$ 0.1. At specific wavelength, called Self-Reproduction Wavelength (SRW), light transmission from the MCF into the SMF is maximum. This periodic phenomenon is also known as self-imaging, previously presented in Section 2.3, indicating that, for certain light wavelengths, the initial phase relation between the supermodes is retrieved after propagating along the 90 cm long MCF segment. The periodicity of the SRW, indicated in Figure 6-14, is identical to the MMI period of $\Delta\lambda$ = 1 nm $\pm$ 0.1. In the MCF laser cavity (Figure 6-13), this translates into maximum FBG feedback for lasing wavelength corresponding to SRW. As a result of the MMI in the MCF, tuning the laser wavelength is expected to impact the cavity feedback and thus influence the laser performances. In practice, tuning the MCF laser emission has been achieved by temperature tuning the HR FBG after fixing it on a hot plate.

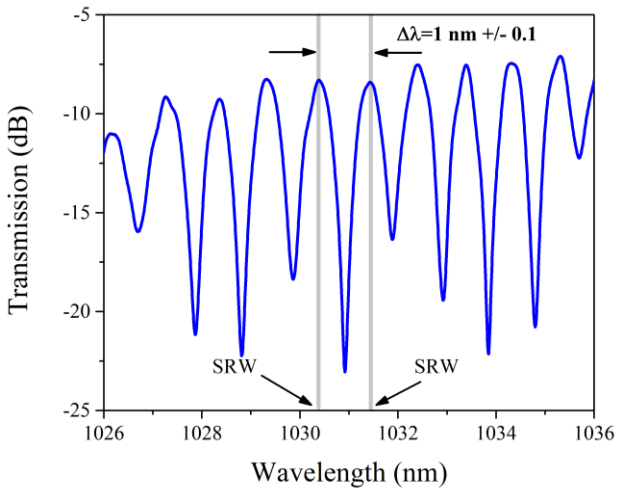

Figure 6-14: Zoom-in from Figure 6-5(a) showing the MMI pattern in the 90 cm long segment of MCF as a function of the light wavelength. Two Self-Reproduction Wavelength (SRW) at which in initial phase relation between the supermodes is reproduced are indicated. This phenomenon is periodic with $\Delta\lambda$ = 1.1 nm.

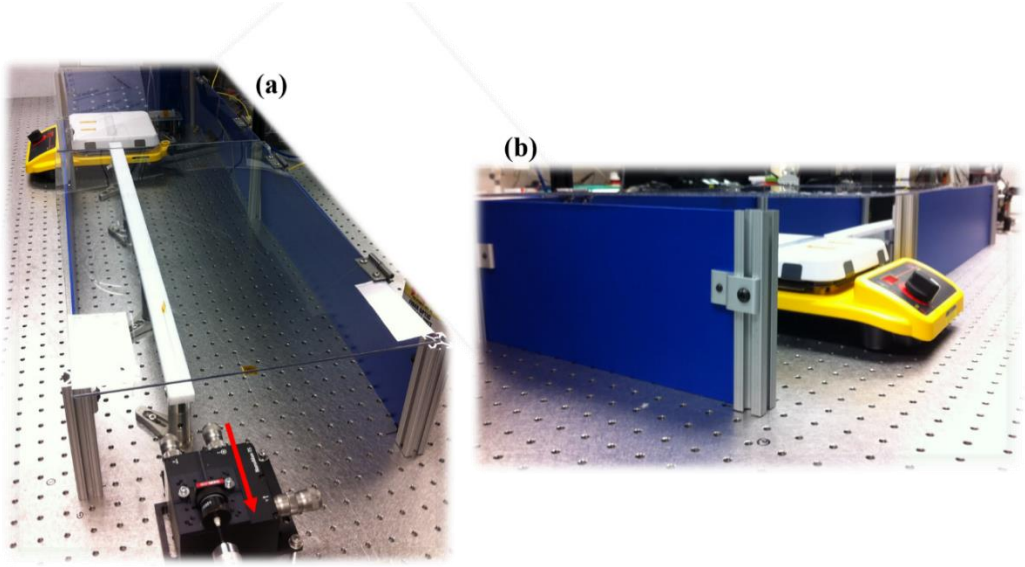

Figure 6-15: (a) Stabilization unit around the MCF laser cavity. The red arrow indicates the direction of the laser emission. (b) Hot plate used for FBG temperature tuning.

In addition, a stabilization unit has been fabricated to isolate the MCF laser from external fluctuations and to ensure stable and reproducible laser performances while tuning the emission wavelength. A laboratory picture of the experiment is presented in Figure 6-15. The MCF is

inserted in a Fused Silica capillary and placed on a thermally isolated holder (white rail in Figure 6-15).

The laser emission wavelength was tuned by temperature tuning the HR FBG from room temperature, up to 220°C. For several tuning conditions, the laser threshold and slope efficiency have been recorded for various pumping levels. The results are plotted in Figure 6-16 in black and blue respectively. The SRW values previously determined from the MCF transmission measurement in Figure 6-14 are indicated using grey lines in Figure 6-16 for visual aid. While tuning the emission wavelength of the MCF laser, the measured values of the laser thresholds and slope efficiencies vary following a quasi-periodic behavior.

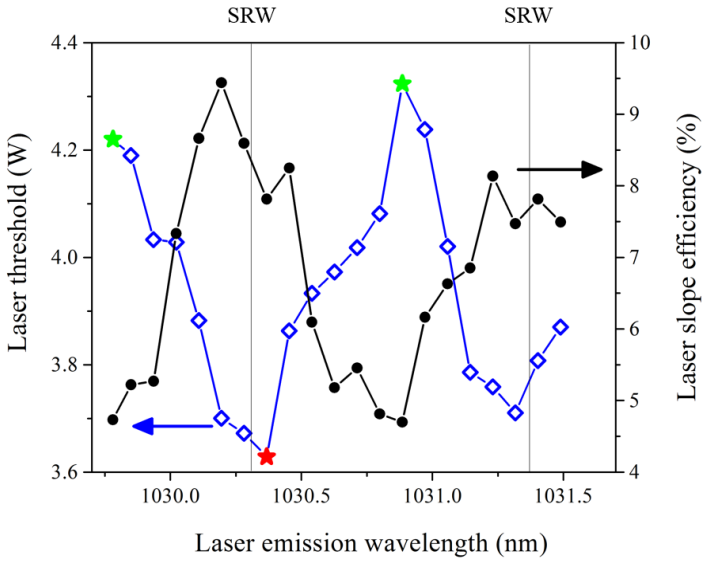

Figure 6-16: Measured MCF laser output performances including lasing threshold (blue) and slope efficiency (black).

The lowest lasing threshold (P_{Pump} = 3.65 W) and slope efficiency (~10%) were achieved when the MCF laser emission was tuned to λ = 1030.37 nm (red markers in Figure 6-16) which corresponds to one of the SRW value previously determined in Figure 6-14. This result is in good agreement with the maximum of transmission in the SMF resulting in an efficient selective FBG

feedback in the MCF center core. On the other hand, within the laser tuning range, two lasing wavelengths corresponding to λ = 1029.70 nm and λ = 1030.87 nm were characterized with the lowest efficiency and highest threshold levels. Indicated using green markers in Figure 6-16, these two lasing wavelengths are located at half the SRW values. At these wavelengths, (transmission minima in Figure 6-14), the cavity feedback is distributed among all the cores at the MCF flat cleave whereas only the center core experiences feedback at the other MCF end which results in lower laser performances. As a result, a periodic behavior of the MCF laser output performances was measured indicating preferred emission wavelengths with low lasing threshold and high slope efficiency reproduced at intervals of $\Delta\lambda$ ~1 nm $\pm$ 0.1 corresponding to the MMI measured in Figure 6-14. It is important to note that the tuning range of laser emission wavelengths presented in Figure 6-16 was limited by the temperature sustained by the HR FBG (maximum around 240°C).

As a result, the ability to reach distinct MCF lasing regimes by simply controlling the wavelength tuning of the laser emission offers a particularly attractive platform to perform decomposition of lasing supermodes.

6.4.2 Lasing modes analysis: results and discussion

The MCF laser beam has been decomposed for different tuning conditions while maintaining a fixed output power above lasing threshold. First, lasing mode analyses results have been compared after tuning the laser at two wavelengths separated by half the MMI period. Results of the distribution of the MP values ρ_n^2 among the 7 supermodes in the MCF laser are summarized in the bar diagram in Figure 6-17 in red and green respectively (corresponding to the colored markers in Figure 6-16). The standard deviation, represented with the black line, shows a good

measurement stability over time. The high efficiency and low lasing threshold laser beam emitting at λ = 1030.37 nm (shown in red in Figure 6-16 and Figure 6-17) contains a significantly higher contribution of SM_1 and SM_6, the two supermodes with non-zero intensity in the center core (see Figure 6-3), than the other supermodes with $\rho^2(SM_1)$ = 22% and $\rho^2(SM_6)$ = 41%. On the other hand, when emitting at a wavelength interval of half the MMI period (λ = 1030.87 nm shown in green), the total MCF laser power is distributed more evenly between all the 7 supermodes, each one being responsible for ~20% of the laser power. More interestingly, the laser beam profiles corresponding to each modal decomposition have been recorded with CCD_1 and are presented in the inset. The differences between the measured laser intensity profiles already indicate that different combinations of modes are simultaneously lasing. The differences between the laser power distributions at SRW (red) and half SRW (green) arise from the different cavity feedbacks.

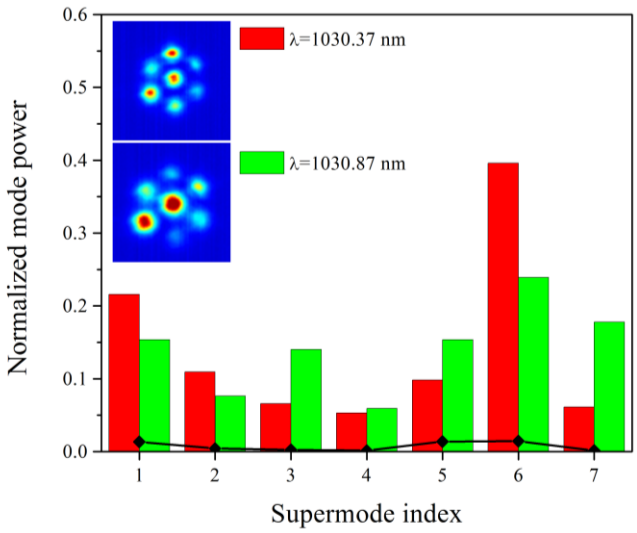

Figure 6-17: Decomposed MCF laser power among the 7 supermodes at two tuning wavelengths: λ = 1030.37 nm (in red), corresponding to a low lasing threshold, and at a highly efficient laser wavelength λ = 1030.87 nm (in green) located at half the MMI period (see Figure 6-16). For each tuning wavelength, the MCF beam profiles recorded with CCD_1.are presented in inset.

To complete this study, a second measurement of the laser emitting at half the SRW was performed after further tuning the FBG temperature. In this case, the decomposition of two MCF laser beams characterized with low efficiency and high threshold (indicated with the two green markers in Figure 6-16) are compared in Figure 6-18. For each tuning condition, the MCF laser beam was recoded with CCD_1 and is presented in inset. Both laser beams present comparable profiles indicating that similar laser power distribution among the supermodes can be expected. This is confirmed from the CFM measurement presenting strong similarities between the two beams, both containing a relatively well distributed MP in all the 7 supermodes.

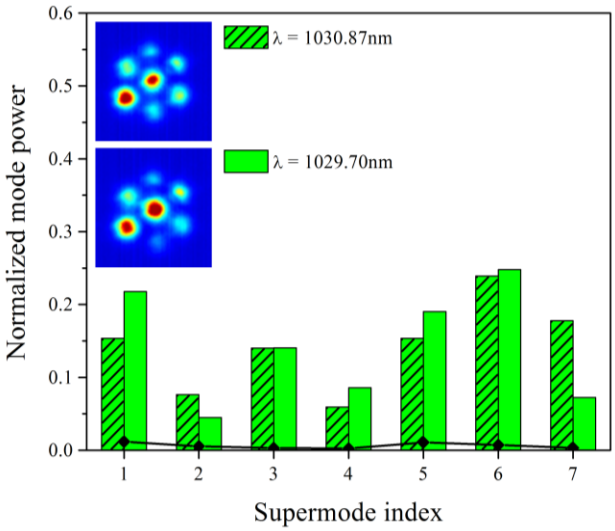

Figure 6-18: Decomposed MCF laser power among the 7 supermodes at two tuning wavelengths located at half the SRW: λ = 1029.70 nm (green) and λ = 1030.37 nm (striped green) corresponding to high lasing threshold and low efficiency lasers (green markers in Figure 6-16). For each tuning wavelength, the MCF beam profiles measured with CCD_1 are presented in inset.

To conclude, an experiment to perform lasing mode decomposition in real time was demonstrated and several regimes of the MCF laser were investigated. This technique shows a high potential to be extended to investigate multi-mode fiber lasers in general. In addition, it offers the possibility to measure the lasing modes while increasing the pump power. This would be of

particular interest to characterize and eventually prevent modal instabilities which are currently limiting the output power level of fiber lasers [121], [123], [150].

6.5 Outlook: temporal effects in monolithic MCF lasers

Pulsed fiber laser sources delivering ultra-short pulses, high peak power in Q-switched or mode-locked regimes delivering pulse durations as short as femtosecond are nowadays common tools in industry and research environments [205]. While several techniques have been successfully employed to generate mode-locking from fiber lasers, they use external devices and sometime free-space equipment such as active amplitude or phase modulators, semiconductor saturable absorbed mirrors (SESAMs), carbons nanotubes, grapheme, etc… which can considerably increase the complexity and the cost of the laser cavity.

Non-linear (NL) effects in optical fibers have been studied for several decades [206]. The long propagation length and small core sizes characteristics of fiber-based systems are favorable to the creation of NL effects such as stimulated Raman Scattering (SRS), Stimulated Brillouin Scattering (SBS), Self-Phase modulation (SPM), Cross-Phase Modulation (XPM) and Four-Wave Mixing (FWM) when using intense light beams. The goal of this section is not to provide an extensive overview of all NL effects in fibers and their applications but rather to focus on a particular phenomenon called Self-Mode Locking (SML). The first demonstration of self-modulation effect in Q-switched fiber laser has been reported in 1993 by Myslinski *et al.* [207] where stable Q-switch operation was obtained as a result of inter-mode beating and SPM. SML has been demonstrated in all-fiber Fabry Perot cavities [208]. More recently, the interest in SML fiber lasers has significantly increased, motivated by the ability to generate stable trains of ultrashort pulses in a monolithically integrated all-fiber system. Luo *et al.* demonstrated a SML

Raman fiber laser [209] and Liu *et al*. presented a SML fiber laser emitting at 2 μm wavelength from a simple linear cavity [210]. Moreover, numerical studies predicted that NL effects occurring in MMFs such as GIMF and MCF offer attractive switching and saturable absorption capabilities to be used in mode-locked fiber lasers [211], [212].

Motivated by the interest in SML fiber lasers, the next section presents the first observation of self-pulsing, pulse breaking and mode-locking in a linear MCF laser cavity.

6.5.1 Presentation of the monolithic MCF laser

The all-fiber MCF laser cavity used in this experiment is schematically presented in Figure 6-19. It uses the same components as the cavity in Figure 6-13 with the addition of a low reflector (LR) FBG written in SMF providing 21 % feedback at λ=1029.95 nm ($\Delta\lambda$ = 0.05 nm). In this configuration, both FBGs are fixed on hot plates in order to temperature tune the laser wavelength across a total bandwidth of 1.4 nm (corresponding to a temperature change from room 23°C to 220°C), resolving over one MMI period ($\Delta\lambda$ = 1 nm $\pm$ 0.1).

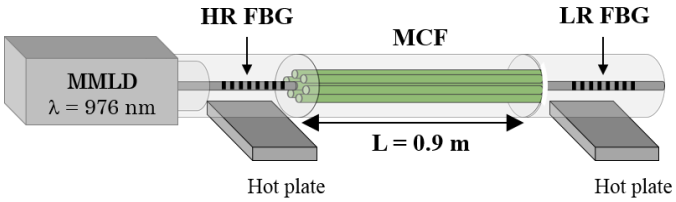

Figure 6-19: Schematic of the monolithic MCF laser with: MMLD: Multi-Mode Laser Diode; HR: High Reflector; LR: Low Reflector FBGs.

The following results are similar to the previous section focused on the study of a MCF laser with HR FBG and flat cleaved output. The reason behind this measurement is due to the fact that, while the MMI period remains constant, repositioning the MCF (for example after splicing with the HR FBG), results in a change in the SRW values. Thus, the lasing threshold of the new

monolithic MCF cavity has been recorded at the SMF output for various tuning conditions. Results are plotted as function of the tuned laser emission wavelength (blue line) and shown in Figure 6-20. The emission spectrum from the MCF laser operating above threshold at λ = 1031.27 nm has been recorded with an OSA. Results are shown in inset of Figure 6-20 resulting a 3 dB bandwidth of 52 pm, dictated by the bandwidth of the LR FBG. For visual comparison, the transmission through the new laser chain has been plotted on the same scale (black line), showing a transverse shift of the SRW values due to the repositioning of the laser chain. For examples, previous MMI maxima at λ = 1030.37 nm has shifted to λ = 1031.27 nm. As expected, results on Figure 6-20 indicate a periodic behavior of the lasing threshold with a direct correspondence between threshold minima and MMI maxima (indicating that, at the interface between MCF and SMFs, the light is mainly in the MCF center core). The higher uniformity of the lasing threshold and the increased modulation depth compared to the results in Figure 6-16 are related to the highly selective feedback imposed by both FBGs.

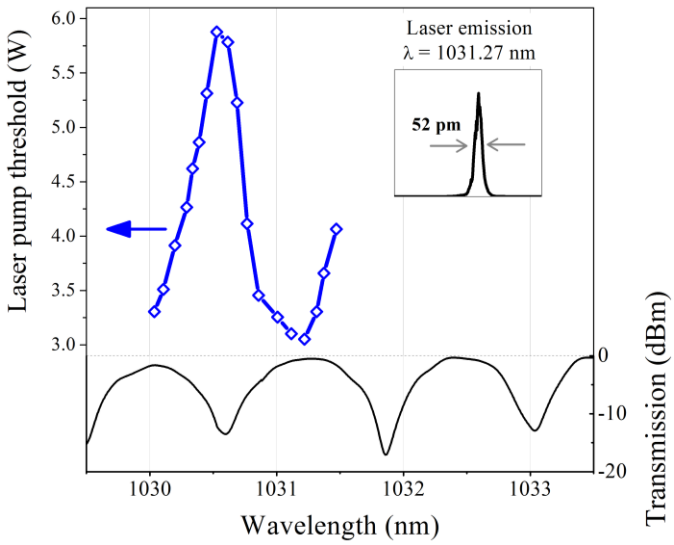

Figure 6-20: Measured laser threshold plotted against the laser emission wavelength (blue line) compared with the MMI pattern (black line). The laser emission spectrum measured at λ = 1031.22 nm is shown in inset with a 3 dB bandwidth of 52 pm.

6.5.2 Towards self-mode locked monolithic MCF laser cavity

The temporal response of the MCF laser has been measured directly from the SMF output using a fast photodiode (PD) as well as a powermeter and an OSA. The Free Spectral Range (FSR) of an optical resonator $\Delta\nu$, is defined by

$$\Delta\nu = \frac{c}{2nL} \quad (52)$$

with L the cavity length, n the refractive index of the propagation medium and c the speed of light. The FSR corresponds to the frequency spacing of the longitudinal modes. The cavity round-trip time τ_c can be defined as $\tau_c = 1/FSR$. The MCF cavity length is approximately 4 meters. Assuming n = 1.45 for the refractive index of Fused Silica, the corresponding cavity roundtrip time is expected to be τ_c ~40 ns. In this section, the MCF laser emission wavelength was fixed to λ = 1031.27 nm corresponding to a MMI maxima.

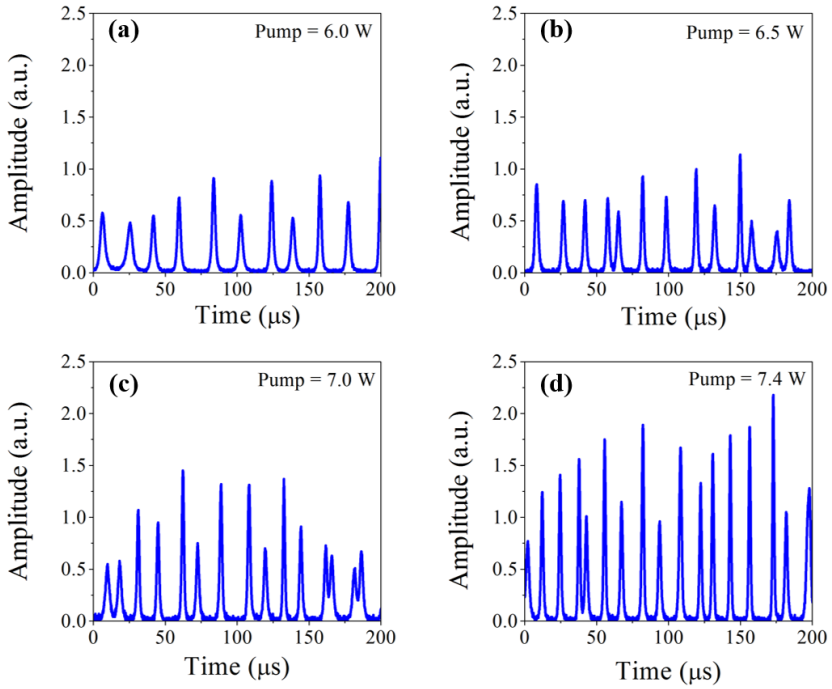

Figure 6-21: (a)-(d) Temporal response measured at the output of the 4 m long MCF laser cavity as the pump power increases from 6 W to 7.4 W.

The PD connected to an oscilloscope were used to record the temporal response from the MCF laser as the pump power was increased. Results are presented in Figure 6-21(a) to (d). While no hint of self-pulsing was measured below lasing threshold (P_{Pump} = 3.05 W), clear pulse trains could be recorded above lasing threshold from 6 W (a) to 7.4 W (d). However, the measured pulse trains was also characterized by a fast jittering (on the order, or less than the μs scale). In order to identify the temporal effect responsible for this behavior, the pulse repetition rate as well as their FWHM were extracted from the measurements Figure 6-21(a) to (d) and results are plotted as function of the pump power and are presented in Figure 6-22(a) and (b) respectively.

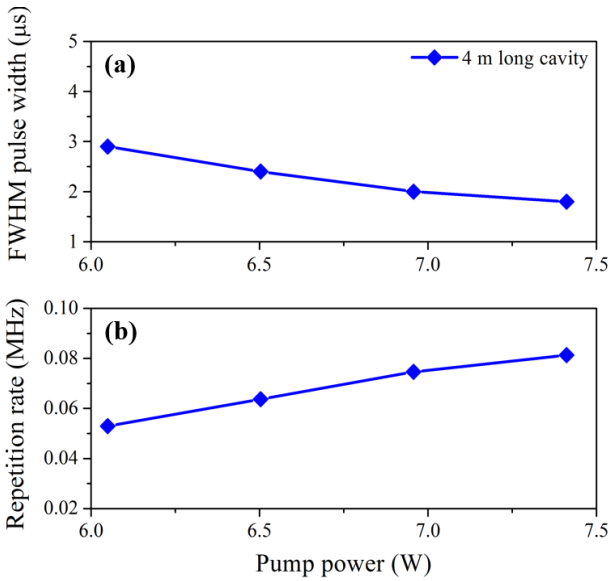

Figure 6-22: Measured FWHM pulse width and repetition rate for various pump powers after the 4m long MCF laser cavity.

As the pump power increased, the pulse FWHM decreased from 2.95 μs to less than 2 μs. On the other hand, the repetition rate, or FSR, increased from 54 kHz to ~80 kHz (corresponding to a cavity round trip time of 12.5 μs and cavity length of 1.3 meter). These observations indicate that a phenomenon of saturable absorption occurred in the laser cavity resulting in the apparition of

unstable Q-switching regimes [210]. However, the high jittering of the pulse train and the mismatch in the measured cavity length indicate non-controlled and unstable pulsed regime.

In order to stabilize and control the self-pulsing, the amount of NL in the laser cavity has been increased using 10 additional meters of SMF fusion spliced between the output end of the MCF and the LR FBG as shown in Figure 6-23. The front end of the laser as well as the MCF position remained unchanged. The total cavity length is now around 14 m corresponding to a cavity round-trip time of τ_c ~135 ns estimated using Equation (52).

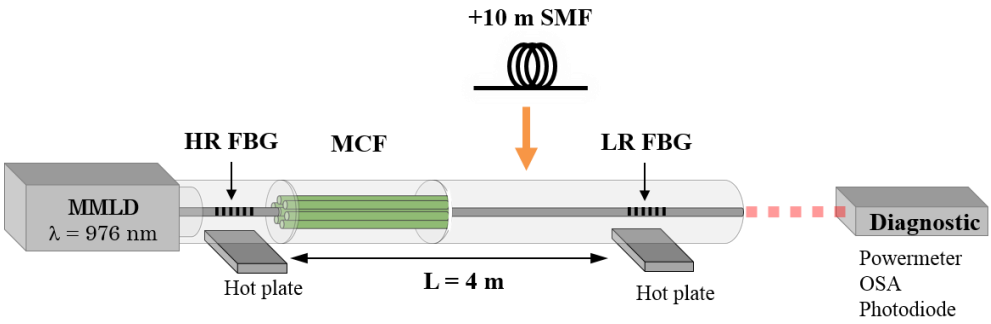

Figure 6-23: Monolithic MCF laser cavity with increased nonlinearities.

The pulse train emerging the 14 m long laser cavity has been measured for various pump powers. Results measured at P_{Pump} = 7.4 W and shown in Figure 6-24(a) can be directly compared to the temporal behavior of measured after the 4 m long cavity in Figure 6-21(d). As the cavity length increases from 4 to 14 m, the initial pulse train tends to look more chaotic. However, after zooming in the temporal response (shown in Figure 6-24(b)), one can see that the initial pulses (τ_c~12.5 μs) break down into shorter pulses separated by 138 ns. According to the definition of the FSR in Equation (52), the corresponding cavity length was calculated to be L = 14.3 meters, which is in good agreement with the experiment. As a result, pulse breaking with durations on the order of the cavity round trip time was measured after increasing the amount of nonlinearities in the MCF laser cavity by increasing to overall length. This pulse-breaking effect has been observed

in similar fiber laser cavities and is characteristic of the regime of unstable Q-switched mode-locking [210]

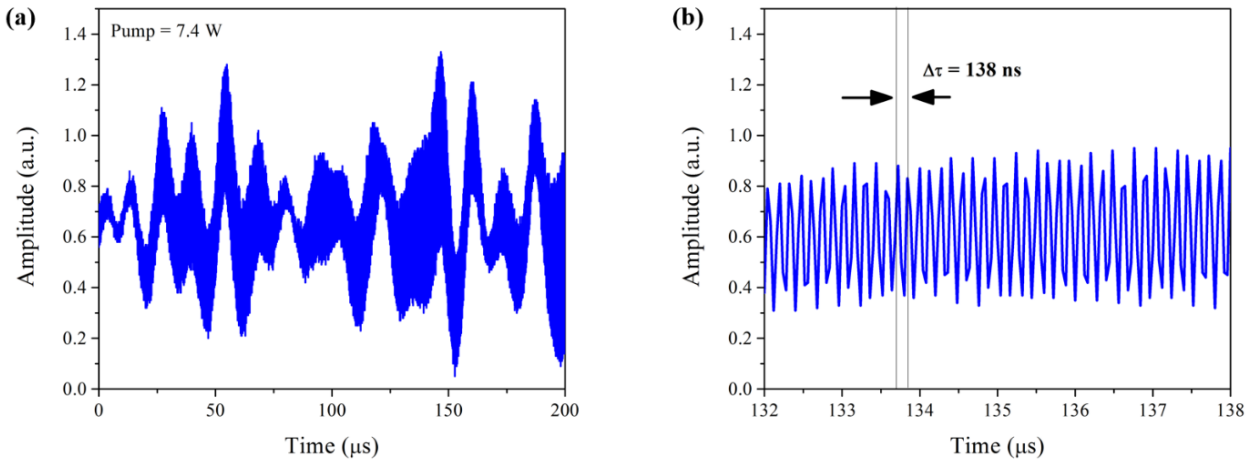

Figure 6-24: (a) Pulse train measured after the 14 m long MCF laser at pump powers of 7.4 W. (b) Zoom-in the pulse train measured in (a) showing the pulse break up and the establishment of unstable Q-switch mode-locking.

The laser spectra emitted from the 4 meters long and 14 meters long MCF cavities were recorded with an OSA, limited by a 20 pm spectral resolution at fixed pump power of 7.4 W. Results are shown in Figure 6-25 in blue and red respectively. Even though the measured linewidth is on the order of the OSA resolution, which does not allow to make any assumption regarding the pulse duration, a small broadening of the peak FWHM could be measured (from 48 to 58 pm width). Similar effect was reported by Liu *et al*. in monolithic fiber laser cavities and is consistent with an increase of the nonlinearities in the laser cavity [210]. Finally, to complete the characterization of the Q-switched mode-locked regime, the laser average output power P_{av} and corresponding pulse energy E_P were calculated according to

$$E_p = \frac{P_{av}}{f_{rep}} \qquad (53)$$

with f_{rep}, the repetition rate. Results presented in Figure 6-26 correspond to the Q-switched mode-locked regime in Figure 6-24 and indicate that pulse energies up to 10 nJ were achieved.

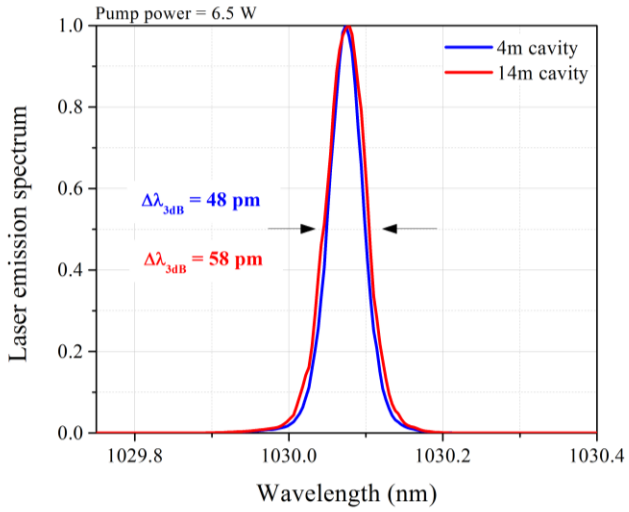

Figure 6-25: Measured laser emission spectrum at fixed pump power for two different cavities lengths showing a hint of spectral broadening.

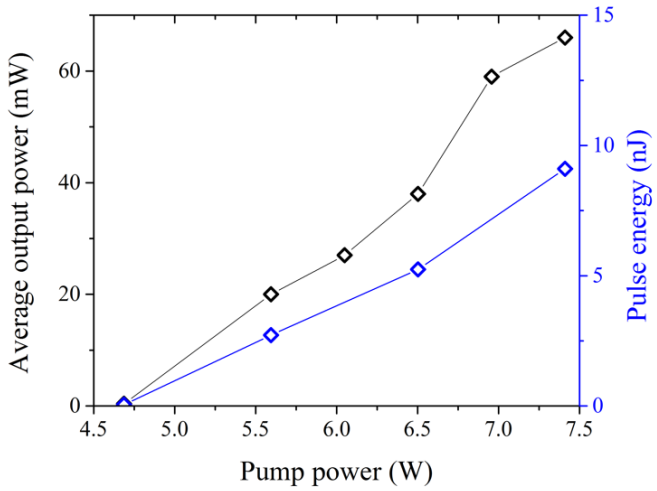

Figure 6-26: Measured average output power and calculated pulse energy from the 14m long laser cavity.

In summary, the first hints towards self-mode-locked operation of a linear MCF laser cavity have been presented. To discuss regarding future outlooks, several steps can be followed in order to generate and characterize a well-established and stable SML regime such as:

- Increasing the fiber laser cavity length, e.g. by increments of 10 meters, and characterize the pulse train.
- Accurately measure the pulse duration using typical autocorrelator experiment.

In addition, it should not be forgotten that results from the temporal characterization of this MCF laser have only been recorded at the MMI maximum. A similar study could be performed at MMI minimum in order to compare and evaluate the influence of the transverse lasing modes on the temporal dynamics of the system. As a result, by wavelength tuning of the laser emission, one could also tune the temporal dynamics emitted by the MCF laser.

6.6 Summary and outlook

In this Chapter, the mechanisms of light propagation, supermodes formation, mode competition, laser dynamics and temporal effects were investigated in a novel specialty fiber design made with 7 single-mode Yb-doped cores.

Due to the small pitch values ($\Lambda = 9.3\ \mu$m), the light coupled in the center core evanescently couples into the neighboring cores leading to the formation of supermodes. Analytical and experimental results demonstrated that, using an input fiber matched to the center core of the MCF, most of the light was distributed among SM_1 and SM_6, the only two supermodes with non-zero intensity in the center core.

Furthermore, three monolithic fiber laser cavities have been fabricated in order to investigate (a) the gain distribution among individual supermodes during light amplification, (b) the dynamics associated with multi-supermode lasing and (c) self-pulsing and Q-switched mode locking effects.

The CFM technique (see Section 3.3) was used to measure mode-resolved gain coefficients using a monolithic MCF amplifier scheme. Results demonstrated a non-uniform distribution of the gain factor among the amplified supermodes where the contribution of SM_1 dominates, followed by SM_6. Furthermore, applying external coil and stress on the MCF, i.e. changing the boundary conditions, did not perturb the relative gain distribution indicating that, in multi-mode doped fibers, the amplified supermode content in the MCF seems to be mainly dictated by the gain profile of the Yb atoms across the 7-cores (not perturbed by external coil and stress). [23]

Then, the first CFM analysis of a multi-mode laser during operation has been demonstrated. Using this technique, the dynamics of the lasing supermode in the MCF could be measured by changing the feedback conditions of the laser cavity via tuning of the laser center wavelength of the laser emission. Two laser regimes were recorded and the fraction of laser light carried by each supermode was measured. Within this study reported in Section 6.4, two main results were reported for the first time with (a) the demonstration of lasing mode decomposition using CFM and (b) the in-depth characterization of lasing dynamics in coupled-cores active MCF [213].

Finally, Section 6.5 provides an outlook on temporal effects in monolithic MCF lasers with the first demonstration of self-pulsing and Q-switched-mode-locking, delivering pulse energies estimated on the order of ~10 nJ at ~ 10 kHz.

To give an outlook, further increasing the amount of non-linearities in the monolithic MCF laser cavity could be an approach employed to obtain controlled and stabilize self-mode-locking. In addition, since this MCF laser was demonstrated to be a few-transverse modes system, it would be of interest to determine the influence of the multi-mode lasing on the temporal effects.

CHAPTER 7: DISSERTATION SUMMARY AND OUTLOOK

The research work presented in this dissertation has directly contributed to several branches of the field of optical fibers, in particular, to specialty designed optical fibers. In this chapter, striking results in the area of fiber design, fiber fabrication, fiber characterization and fiber lasers are summarized and outlook is given.

The driving force behind the development of novel fiber designs, tailored to enable the delivery (or the generation) of specific light properties for targeted applications was presented in details in Chapter 1 and Chapter 2, experimentally and numerically respectively. In Chapter 1, a concrete example of novel fiber design, the ring-PCF, realized in CREOL, was used to illustrate the general steps of (a) fiber creation, (b) fiber design and (c) fiber fabrication, resulting in the introduction of novel micro-structured specialty fibers. Chapter 2 provided the numerical tools used to describe the impact of the fiber design as well as the effect of external perturbations (e.g. coiling, coupling alignment, etc) on the propagating light and on the guided transverse mode.

Delivering specific properties of light using specialty fiber design stands for controlling the guided mode content. Thus, to accurately characterize specialty fiber designs, experimental diagnostics able to access individual guided modes, such as the S^2 imaging technique and the Correlation Filter Method (CFM), were introduced in Chapter 3. In this context, extended mode decomposition capabilities beyond the limits set by the actual mode analysis techniques were reported, enabling to reconstruct the amplitude and phase profiles of individual guided modes, to calculate total vector-beams. In addition, it has been demonstrated that, individual transverse

modes carrying between ~0.01% and ~30% of the light can be resolved with unmatched accuracy when employing S^2 imaging [108][109].

These techniques have been applied in Chapter 4. In Section 4.1, a prototype LCF design was demonstrated to satisfy the single-mode purity and beam quality requirements for fiber laser applications. In addition, it was possible to demonstrate, for the first time, that the LCF operates in the single-mode regime for wavelengths comprised between 1 and 2 μm. [22]. On the other hand, a second mode analysis study, reported in Section 4.2, was conducted to experimentally demonstrate, for the first time, the influence of the inner fiber design as well as the effect of external fluctuations on individual guided modes propagating at λ = 2 μm. To do so, the guided modes in three different LMA fibers designs, a SIF, a PCF and a LCF were resolved and compared [137]–[139]. As a result, tailored PCF and LCF designs delivered pure single-mode beam, outperforming the SIF design. In particular, the LCF delivered λ = 2 μm light beams with > 99.9% single-mode purity within a mode-field area of ~ 1600 μm^2. with. To give an outlook, the methods employed in Chapter 3 and 4 can be further used to perform in-depth characterization of novel specialty fiber designs and characterize specific light properties. .

Chapter 5 and Chapter 6 of this dissertation, were oriented towards the development of monolithic fiber laser systems, often limited by the poor compatibility between conventional fiber devices and specialty fiber designs. In Chapter 5, an all-fiber device, using selected length of multi-mode graded index fiber, was demonstrated to perform as a beam expander. Striking results, including the ability to improve light transmission by a factor of 11 dB between two fibers, a single-mode fiber and a LMA PCF, mismatched by a factor 18, were reported. The MFA devices were furthermore used to assemble the first monolithic fiber lasers employing FBGs in SMF, to provide the cavity feedback, and an active LMA PCF, used as the gain medium. Mode-matched

fiber lasers outperformed the directly-coupled cavities. [170]–[172]. This all-fiber MFA approach offers a simple, robust, cost-effective and scalable alternative towards the systematic integration of specialty fibers in monolithic fiber lasers.

The second type of monolithic fiber laser system studied in Chapter 6 of this dissertation utilized a specialty gain fiber made with 7 single-mode, Yb-doped, cores in which two out of seven supermodes were excited. This multi-supermode MCF laser system was used, for the first time, to investigate novel laser output performances as well as mechanisms related to lasing dynamics, transverse mode competition and temporal effects in details. The CFM mode analysis technique presented in Chapter 3 was employed to demonstrate (a) the first mode-resolved gain analysis in a two-mode MCF amplifier [23] and (b) the dynamics associated with multi-supermode lasing [213]. Both of these approached can be used to investigate any gain competition mechanism of lasing dynamics in few-modes fiber lasers. The outlook on this novel monolithic MCF laser cavity would be to further investigate temporal effects leading, for example, to a novel laser source for self-mode locking.

APPENDIX A:
ANALYTICAL MODEL OF MULTIMODE INTERFERENCE IN OPTICAL FIBERS

The S^2 imaging mode analysis technique is the spatially resolved measurement of the spectral interference in few-modes fibers. According to the The electromagnetic field $E(r,z)$ emerging from an optical fiber is the sum of the individual contributions of the n guided modes

$$E(r,z) = \sum_{n=1}^{n_{max}} \Psi_n(r,z) \quad (54)$$

with $\Psi_n(r,z)$ the complex amplitude of the n^{th} transverse mode expressed as

$$\Psi_n(r,z) = c_n \varphi_n(r) e^{i\beta_n z} \quad (55)$$

with β_n the propagation constant of the n^{th} mode, z the propagation length, $\psi_n(r)$ the mode amplitude and c_n, the field excitation coefficient defined by the overlap integral relation

$$c_n = \frac{\int E(r,z).\varphi_n(r)dr}{\sqrt{\int \varphi_n(r)^2 dr}} \quad (56)$$

When performing S^2 imaging, the light intensity at different locations across the near-field plane is measured using an optical spectrum analyzer. The intensity of the light delivered by the few-mode fiber of length L can be expressed by

$$I(r) = |E(r,L)|^2 = \left| \sum_{n=1}^{n_{max}} \Psi_n(r,L) \right|^2 \quad (57)$$

For simplicity, let's consider a fiber guiding only two transverse modes. It is however important to mention that the following mathematical developpment can be generalized to n guided modes. The total field of the beam emerginf the fiber can be written using the following expression

$$E(r,z) = \left\{ \psi_{0,1}(r) e^{i\beta_1 z} + \psi_{0,2}(r) e^{i(\beta_2)z} \right\} \quad (58)$$

The equation describing the measurable beam intensity is then

$$I(r) = |E_1(r,z) + E_2(r,z)|^2 \quad (59)$$

$$I(r) = I_1(r) + I_2(r) + 2\sqrt{I_1(r)I_2(r)}\,cos(\Delta\phi). \quad (60)$$

Similar to a two beam interference, $\sqrt{I_1 I_2} = C$ represents the fringe contrast and $\Delta\phi$ is the period of the cosine oscillatory function. According to Equation (58), the argument of the cosine function is a function of the light wavelength λ and of the fiber length $z = L$ expressed with

$$\Delta\phi = (\beta_2 - \beta_1)L \quad (61)$$

$$\Delta\phi(\lambda) = \frac{2\pi}{\lambda}(n_{eff,2} - n_{eff,1})L \quad (62)$$

This periodic behavior is called Multi-Mode Interference (MMI). Each combination of two modes interfering will results in a MMI pattern with different periodicity since it depends on the effective mode indices. The MMI can be experimentally measured after recording the intensity of light carrying more than one transverse mode. MMI can be observed after measuring the light intensity after propagating various length of fiber at a fixed wavelength or by measuring the spectrum of light propagating in a fixed fiber length. This last principle is used in S^2 imaging mode analysis technique. As a result, the total intensity profile $I(r)$ of the light emerging a few-modes fiber can be numerically reconstructed. To do so, the MMI periodicity $\Delta\phi$ can be measured using an OSA or a spectrometer. On the other hand, the intensities of each transverse modes I_1 and I_2 can be also recognized as the values of the normalized mode power ρ_1^2 and ρ_2^2 which are extracted from S^2 imaging measurements. As a result, the measured values of $\Delta\phi$ and C can be used to reconstruct the total intensity profile of the two interfering modes (or n interfering modes) and predict or verify the total beam profile measured with a CCD. Two examples are shown in Figure A- 1 illustrating the case of where the FM LP_{01} and the first HOM LP_{11} interfere. In Figure A- 1(a), the mode powers are assumed equal with $I_1 = I_2 = 0.5$ while the value of the intermodal phase $\Delta\phi$ varies. On the other hand, $\Delta\phi$ is fixed to the value of $\pi/2$ in In Figure A- 1(b) while the ration

between I_1 and I_2 is changed. This powerful calculation tool can be used as a reference, in particular when measuring beams made of complex mode mixtures exhibiting a complex intensity profile.

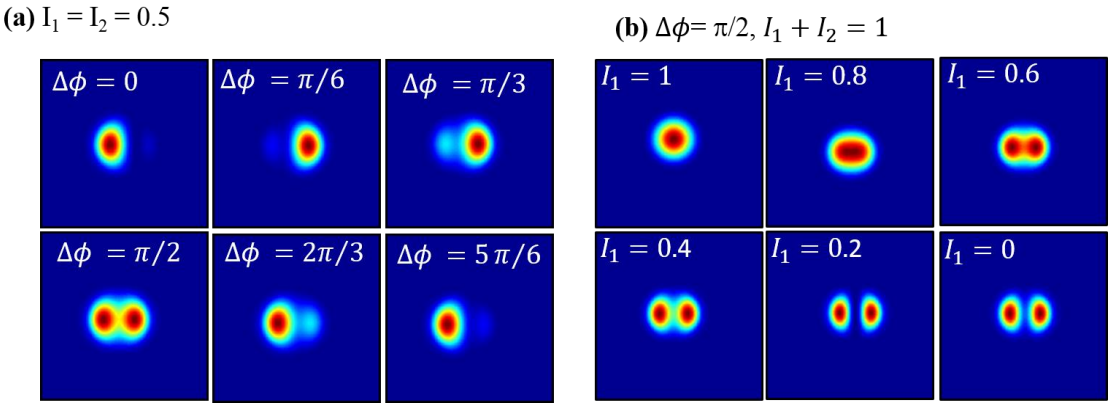

Figure A- 1: Calculated intensity profiles resulting from the interference between LP_{01} and LP_{11} for (a) different intermodal phases and constant mode ration and then for (b) various mode ratio and a fixed intermodal phase of $\pi/2$.

APPENDIX B:
DETAILED PROCEDURE FOR S^2 IMAGING DATA ANALYSIS AND NUMERICAL EVALUATION OF THE MODE POWER COEFFICIENTS

This appendix contains two major sections. First, the steps taken to process the measurement recorded during S^2 imaging and extract individual mode powers, reconstruct the mode intensity and the phase profile are detailed. Then, the numerical methods to evaluate the mode power coefficients will be provided.

- S^2 imaging post-measurement processing

The detailed experiment for S^2 imaging mode analysis was shown in Figure 3-1. Using a probe fiber, the intensity signal at several locations across the near-field are recorded using an OSA. The example of a near field emerging a few-modes fiber is presented in Figure B- 1(a) corresponding to a combination of 60% of LP_{01} and 40% of LP_{11} with $\Delta\phi = \pi/2$. In Figure B-1(b), the typical spectral response measured at two locations across the near field indicated with black and green dots are plotted using black and green lines respectively. It clearly shows that the measured spectral response depends on the probe fiber position in the near field i.e. on the spatial overlap between the modes.

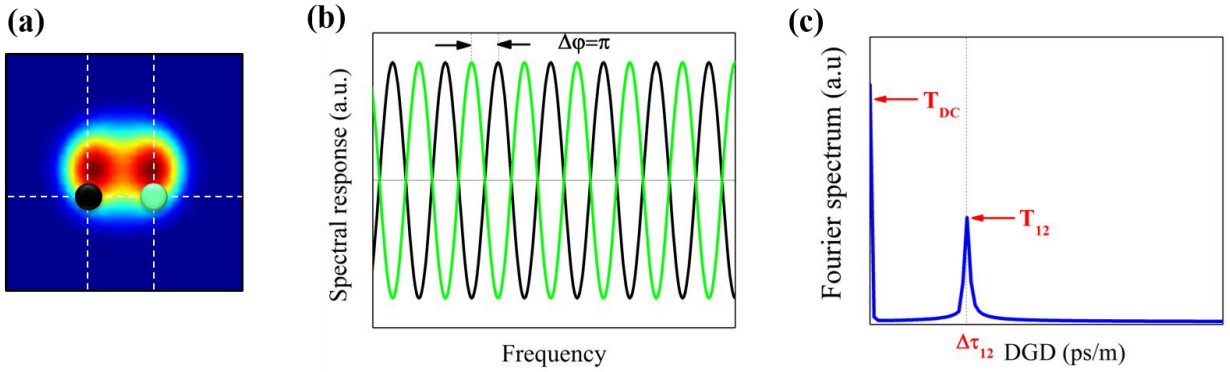

Figure B- 1:calculated intensity profile of a beam comprising 60% of LP_{01} and 40% of LP_{11} with $\Phi = \pi/2$ in (a). In (b), typical spectral response at two out-of-phase locations indicated in (a). Calculated Fourier spectrum $F(\tau)$ indicating T_{DC} and T_{12}, decoupled and used to decouple $LP_{11}$from LP_{01}.

As a result, the spectral response recorded in the center of the image, where only LP_{01} is present is expected to be flat. In addition, the intermodal phase in Figure B- 1(b) shows the expected π phase shift between the two lobes of the HOM LP_{11}. The intermodal phase is recorded for all traces measured across the near field and compared to the same reference.

To evaluate S^2 imaging results, the measured spectra are Fourier transformed. Since periodic functions in the frequency domain (i.e. MMI) result in sharp features in the temporal domain after Fourier processing, guided modes can be decomposed and identified according to their characteristic MMI period. This is schematically represented in Figure B- 1(c). The temporal scale of the Fourier spectra is labeled Differential Group Delay (DGD), expressed in sec/m and is defined as

$$DGD = \frac{\Delta\tau_{12}}{L} \quad (63)$$

where $\Delta\tau_{12}$, indicated in Figure B- 1(c), corresponds to the modal group index of the two modes interfering, previously defined in Equation (27) and L is the length of fiber used in the measurement. Replacing Equation (27) in Equation (63) results in an expression of the DGD in terms of effective index difference $\Delta n_{eff} = n_{eff,1} - n_{eff,2}$ according to

$$DGD = \frac{1}{c}\Delta n_{eff}. \quad (64)$$

Replacing the expression of Δn_{eff} in Equation (62) using the DGD term in Equation (64) results in the MMI periodicity expressed in terms of the DGD according to

$$\Delta\phi = \omega.L.DGD \quad (65)$$

where $\omega = (2\pi c)/\lambda$ is the light frequency. As a result, the measured DGD, corresponding to two-modes interfering in the Fourier domain, is directly proportional to the period of the MMI measured in S^2 imaging. To illustrate the identification process of the two modes responsible for

each Fourier features, two parameters are introduced, labeled T_{DC} and T_{12}. In the Fourier domain, these can be evaluated by recording the Fourier amplitude at the corresponding DGD for each spectral measurement. A parallel can be done with terms of the Equation (60) where T_{DC} corresponds to the DC level of the spectral measurement of MMI such that

$$T_{DC} = I_1 + I_2 \quad (66)$$

and T_{12} is proportional to the contrast C previously defines as

$$T_{12} = C = 2\sqrt{I_1}\sqrt{I_2} \quad (67)$$

Since the values of T_{DC} and T_{12} can be measured from the total Fourier spectra (i.e. the sum of all the Fourier spectral of each recorded spectral trace), Equations (66)and (67) form a system of two equations with two unknown that can be solved to find $I_1 = \rho_1^2$ and $I_2 = \rho_2^2$. However, this approach is limited to two-modes interfering. In many few-modes fibers, several mode are simultaneously guided. Thus, a more complete numerical approach is required to resolve the individual mode powers from S2 imaging and will be discussed in Appendix C.

There are two methods to identify the modes interfering at a Fourier feature T_{nm}. First, one can numerically evaluate the DGD (Equation (64)) at which the two modes interfere using the effective index values $n_{eff,n}$ obtained with a mode solver for the guided modes. Even though this calculation might help to verify the consistency of the results obtained from S2 imaging, its accuracy strongly depends on the accuracy of the mode solver and requires a deep characterization of the fiber prior to a mode analysis measurement. The second approach is to record the amplitude of the Fourier transform T_{nm} at a fixed DGD for each measurement across the fiber near-field. As a result, the amplitude profile of the HOM interfering at the DGD can be reconstructed and the mode can be clearly identified. The mode phase profile can also be reconstructed by measuring

the intermodal phase (see example in Figure B- 1(b)) for each measured spectrum. Examples of mode power evaluation, mode amplitude and phase profile reconstruction are detailed in this dissertation.

- Numerical method for the evaluation of the mode power coefficients

In this appendix, three different numerical approaches are proposed to evaluate the mode powers ρ_n^2 depending on different assumptions on the fiber and on the guided modes. To do so, the general case of n modes interfering is considered. According to Equation (57), the intensity distribution of the field emerging a fiber guiding n transverse modes can be generalized to

$$I(r,\lambda) = T_{DC} + \sum_{a=1}^{N}\sum_{b=1}^{N} \frac{{T_{AC}}^{ab}}{2} cos(\Delta\phi_{ab}(\lambda)) \quad (68)$$

where, according to the examples provided in Appendix B, the Fourier amplitudes T_{DC} and T_{AC}^{ab} are defined by

$$T_{DC} = I_1 + I_2 + \cdots + I_N \quad (69)$$

$${T_{AC}}^{ab} = 2\sqrt{I_a I_b} \quad (70)$$

with $\Delta\phi_{ab}$ already defined in Equation (62) and Equation (65).

- Method 1: This evaluation procedure is best suited when most of the power is guided in the FM LP_{01}.

Under this assumption, Equation (69) becomes

$$T_{DC} \cong I_{FM} = \rho^2(LP_{01}) \quad (71)$$

In other words, $\rho^2(LP_{01})$, the mode power of the FM, can be directly measured as the Fourier amplitude of the DC peak at DGD = 0 ps/m. A consequence of this strict assumption is that no

inter-modal coupling exist between the guided HOM. Thus, all the cross-terms ${T_{AC}}^{ab}$ with $a \neq 1$ are equal to zero (assuming the FM is considered as the mode #1, the first HOM as the mode #2, etc…). In practice, no Fourier feature is expected at the DGD corresponding to two HOMs interfering and evaluated from Equation (64).

Under these assumptions, the measured Fourier amplitudes ${T_{AC}}^{FM,HOM}$ defined by Equation (70) transform in

$${T_{AC}}^{FM,HOM} = 2\sqrt{I_{FM} I_{HOM}} \quad (72)$$

which further leads to

$${T_{AC}}^{FM,HOM} = 2\sqrt{T_{DC} I_{HOM}} \quad (73)$$

As a result, the mode power of individual HOMs can be evaluated from

$$\rho^2(HOM) = \frac{{T_{AC}}^{FM,HOM\,2}}{4T_{DC}} \quad (74)$$

This evaluation technique is particularly suitable to resolve weakly guided HOM content in few-modes fibers. To date, most of the S2 imaging studies reported in the literature employ this approach to evaluate the mode powers. It is commonly known as Multi-Path Interference (MPI) defined as

$$MPI = 10 \times log\{\rho^2(HOM)\} \quad (75)$$

However, as the amount of power carried by the HOMs increases, the initial assumptions are not fulfilled leading to an unappropriated evaluation procedure.

A complete study has been demonstrated to determine the exact working range of this evaluation method as function of the power fraction guided in the HOM.

- Method 2: General case of n modes interfering but where the intermodal coupling remains low.

The general solutions of the system of two equations (69) and (70) can be expressed as

$$I_{1,2}(r) = \frac{1}{2}\left(T_{DC} \pm \sqrt{{T_{DC}}^2 - \sum_{a,a\neq b}^{N} \left({T_{AC}}^{ab}\right)^2} \right) \quad (76)$$

where a and b denote different guided modes. The solution I_1 corresponds to ρ_1^2, the mode power of the mode #1 corresponding to the positive solution. On the other side, I_2 refers to the sum of all the remaining mode powers. Thus, this equation can be solved after several iterations.

- Method 3: general analytical mode evaluation

This approach can be employed regardless of the mode power distribution in the fiber. In the case of three guide modes (or more) labeled 1, 2 and 3, the mode power coefficients are obtained from the following system of n equations corresponding to the n guided modes:

$$\rho_1^2 = \frac{{T_{AC}}^{12}{T_{AC}}^{13}}{{T_{AC}}^{23}} \quad (77)$$

$$\rho_2^2 = \frac{{T_{AC}}^{21}{T_{AC}}^{23}}{{T_{AC}}^{13}} \quad (78)$$

$$\rho_3^2 = \frac{{T_{AC}}^{31}{T_{AC}}^{32}}{{T_{AC}}^{12}} \quad (79)$$

However, for this approach to be applicable, the interference between HOMs must be measurable on the FT which is, in practice. Indeed, the complexity of the Fourier trace increases with increasing inter-modal coupling.

These analytical concepts were inspired from the recent work by Otto *et al*. [113].

APPENDIX C:
COUPLED-CORE THEORY AND LIGHT PROPAGATION IN 7-CORES FIBER

The mathematical development presented in this appendix was used to derivate the Equation (48) used in Section 6.2.

Using a semi-analytical model based on the coupled mode theory [201], the beam propagation equation of the 7-core coupled fiber can be written as

$$\frac{dE_i}{dz} = -i\left(\sum_{j=1}^{7} M_{ij}E_j\right) \quad (80)$$

The eigenvectors E_i of the coupling matrix Equation (80) correspond to the field of each of the 7 transverse supermodes guided in the MCF. The corresponding eigenvalues are the effective propagation constants

$$\mathrm{M_{ii}} = \beta_\mathrm{i} \text{ for } i = 1,\ldots,7 \quad (81)$$

and the core-coupling coefficients defined as

$$\mathrm{M_{i1}} = \mathrm{M_{1i}} = \mathrm{M_{i,i-1}} = \tilde{\mathrm{c}} \text{ for } i=2,\ldots,7 \quad (82)$$

where i = 1 stands for the center core and i = 2,…,7 represent the surrounding cores.

In the present study, the input fiber is assumed to be a single-core, single-mode fiber. In the ideal case, is is assumed to be matched to the center of the MCF. As a result, only the eigenvectors overlapping with the center core (i.e. with non-zero center intensity) are excited and propagate in the MCF. Two eigenvectors propagate in the MCF under this excitation and are defined with

$$\overrightarrow{E_1} = \begin{pmatrix} -1+\sqrt{7} \\ 1 \\ \vdots \end{pmatrix}, \overrightarrow{E_6} = \begin{pmatrix} 1+\sqrt{7} \\ 1 \\ \vdots \end{pmatrix} \quad (83)$$

where the dots indicate that the 5 following values are equal to 1. The fields of the propagating supermodes can be defined as

$$E_i(z) = E_i(0)e^{i\widetilde{\beta_i}z} \quad (84)$$

with L the MCF length and the eigenvalues $\widetilde{\beta_\iota}$, also called effective propagation constants and defined according to Equation (83) as

$$\widetilde{\beta_1} = \beta - (1 - \sqrt{7})\tilde{c} \quad (85)$$

$$\widetilde{\beta_6} = \beta + (1 + \sqrt{7})\tilde{c} \quad (86)$$

The MCF transmission collected using the same single-core, single-mode matched fiber can be calculated according to

$$T = |E_1^*(0)E_1(L) + E_6^*(0)E_6(L)|^2. \quad (87)$$

As a result, the MCF transmitted intensity can be expressed as

$$T(\nu) = 1 - 4P_1P_6\, sin^2(2\sqrt{7}\tilde{c}(\nu)L) \quad (88)$$

with ν the frequency of the propagating light and $\tilde{c}$ the coupling coefficient. Equation (88) is similar to the two-modes interference intensity function previously mentioned (Equation (60)) with $P_1 = \rho_1^2$ and $P_6 = \rho_6^2$, proportional to the mode power in each supermode defined by

$$P_1 = |E_1(0)|^2 = \frac{\left(-1 + \sqrt{7}\right)^2}{6 + \left(-1 + \sqrt{7}\right)^2} \approx 31\% \quad (89)$$

$$P_6 = |E_6(0)|^2 = \frac{\left(1 + \sqrt{7}\right)^2}{6 + \left(1 + \sqrt{7}\right)^2} \approx 69\% \quad (90)$$

The Taylor expansion of the transmission in defined by Equation (88) around the frequency dependent coupling coefficient $\tilde{c}(\nu)$ can be written as

$$T(\nu) = 1 - 4P_1P_6\, sin^2(\phi_0 + 2\pi\tau_0\nu) \quad (91)$$

The phase term ϕ_0 and the delay τ_0 of the transmission Taylor expansion can be expressed by

$$\phi_0 = 2\sqrt{7}\tilde{c}(\nu_0)L - 2\sqrt{7}\tilde{c}_1\nu_0 L \quad (92)$$

$$\tau_0 = \frac{\sqrt{7}}{\pi}\tilde{c}_1 L \qquad (93)$$

with ν_0 = 281.76 THz corresponding to λ_0 = 1064 nm, the wavelength used in the study detailed in Chapter 6. The coefficient $\tilde{c}_1$ corresponding to the modal delay between the two propagating supermodes SM_1 and SM_6 and it can be calculated from the derivative of $\tilde{c}$ with respect to the frequency. The coefficient, $\tilde{c}_1$ can also be identified as the inter-modal delay defined from Equation (27).

LIST OF REFERENCES

[1] CNN, "http://www.cnn.com/interactive/2013/11/tech/cnn10-inventions/," 2014.

[2] A. L. Schawlow and C. H. Townes, "Infrared and optical masers," *Phys. Rev.*, vol. 112, no. 6, pp. 1940–1949, 1958.

[3] T. H. Maiman, "Stimulated optical radiation in Ruby," *Nature*, vol. 187, pp. 493–494, 1960.

[4] K. C. Kao and G. A. Hockham, "Dielectric-fibre surface waveguides for optical frequencies," *Proc. IEE*, vol. 113, no. 7, pp. 1151–1158, 1966.

[5] F. P. Kapron, D. B. Keck, and R. D. Maurer, "Radiation losses in glass optical waveguides," *Appl. Phys. Lett.*, vol. 17, no. 423, pp. 423–425, 1970.

[6] J. B. MacChesney, P. B. O'Connor, and H. M. Presby, "A new technique for the preparation of low-loss and graded-index optical fibers," *Proc. IEEE*, vol. 62, no. 9, pp. 1280–1281, 1974.

[7] R. J. Mears, L. Reekie, I. M. Jauncey, and D. N. Payne, "Low-noise Erbium-doped fibre amplifier operating at 1.54 um," *Electron. Lett.*, vol. 23, no. 19, pp. 1026–1028, 1987.

[8] E. Snitzer, H. Po, F. Hakimi, R. Tumminelli, and B. C. McCollum, "Double clad, offset core Nd fiber laser," in *Proc. Conf. Optical Fiber Sensors*, post–deadline paper PD5–1, 1998.

[9] T. A. Birks, J. C. Knight, and P. S. J. Russell, "Endlessly single-mode photonic crystal fiber," *Opt. Lett.*, vol. 22, no. 13, pp. 961, 1997.

[10] T. Birks, J. Knight, and P. Russell, "Sigle mode optical fiber," US 6,334,019 B1, 2001.

[11] J. C. Knight, J. Broeng, T. A. Birks, and P. S. J. Russell, "Photonic band gap guidance in optical fibers," *Science*, vol. 282, no. 5393, pp. 1476–1478, 1998.

[12] R. F. Cregan, "Single-mode photonic band gap guidance of light in air," *Science*, vol. 285, pp. 1537–1539, 1999.

[13] K. M. Kiang, K. Frampton, T. M. Monro, R. Moore, J. Tucknott, D. W. Hewak, D. J. Richardson, and H. N. Rutt, "Extruded singlemode non-silica glass holey optical fibres," *Electron. Lett.*, vol. 38, no. 12, pp. 546, 2002.

[14] Y. Jeong, A. J. Boyland, J. K. Sahu, S. Chung, J. Nilsson, and D. N. Payne, "Multi-kilowatt single-mode Ytterbium-doped large-core fiber laser," *J Opt. Soc. Korea*, vol. 13, no. 4, pp. 416–422, 2009.

[15] A. Zakery and S. R. Elliott, "Optical properties and applications of chalcogenide glasses: a review," *J. Non. Cryst. Solids*, vol. 330, pp. 1–12, 2003.

[16] Y. W. Lee, S. Sinha, M. J. F. Digonnet, R. L. Byer, and S. Jiang, "20 W single-mode Yb3+ -doped phosphate fiber laser," *Opt. Lett.*, vol. 31, no. 22, pp. 3255–3257, 2006.

[17] P. Hofmann, R. Amezcua-correa, E. Antonio-lopez, D. Ott, M. Segall, I. Divliansky, J. Lumeau, L. Glebova, L. Glebov, N. Peyghambarian, and A. Schülzgen, "Strong Bragg gratings in highly photosensitive photo-thermo-refractive-glass optical fiber," *IEEE Photonics Technol. Lett.*, vol. 25, no. 1, pp. 25–28, 2013.

[18] G. Humbert, J. Knight, G. Bouwmans, P. Russell, D. Williams, P. Roberts, and B. Mangan, "Hollow core photonic crystal fibers for beam delivery," *Opt. Express*, vol. 12, no. 8, pp. 1477–84, 2004.

[19] P. Russell, "Photonic crystal fibers," *Science*, vol. 299, no. 5605, pp. 358–62, 2003.

[20] J. Limpert, O. Schmidt, J. Rothhardt, F. Röser, T. Schreiber, A. Tünnermann, S. Ermeneux, P. Yvernault, and F. Salin, "Extended single-mode photonic crystal fiber lasers," *Opt. Express*, vol. 14, no. 7, pp. 2715–20, 2006.

[21] F. Stutzki, F. Jansen, T. Eidam, A. Steinmetz, C. Jauregui, J. Limpert, and A. Tünnermann, "High average power large-pitch fiber amplifier with robust single-mode operation.," *Opt. Lett.*, vol. 36, no. 5, pp. 689–91, 2011.

[22] C. Jollivet, K. Wei, B. Samson, and A. Schulzgen, "Low-loss, single-mode propagation in large-mode-area leakage channel fiber from 1 to 2 μm," in *OSA Technical Digest CLEO*, CM3I.4, 2013.

[23] C. Jollivet, A. Mafi, D. Flamm, M. Duparré, K. Schuster, S. Grimm, and A. Schülzgen, "Mode-resolved gain analysis of a 7-core fiber laser based on multi-supermode interference," in *Advanced Photonics Congress OSA*, SoW2B.2, 2014.

[24] X. Zhu, A. Schülzgen, L. Li, H. Li, V. L. Temyanko, J. V Moloney, and N. Peyghambarian, "Birefringent in-phase supermode operation of a multicore microstructured fiber laser," *Opt. Express*, vol. 15, no. 16, pp. 10340–5, 2007.

[25] C. Xia, R. Amezcua-correa, N. Bai, E. Antonio-lopez, D. M. Arrioja, A. Schulzgen, M. Richardson, J. Liñares, C. Montero, E. Mateo, X. Zhou, and G. Li, "Hole-assisted few-mode multicore fiber for high-density space-division multiplexing," *IEEE Photonics Technol. Lett.*, vol. 24, no. 21, pp. 1914–1917, 2012.

[26] R. Dorn, S. Quabis, and G. Leuchs, "Sharper focus for a radially polarized light beam," *Phys. Rev. Lett.*, vol. 91, no. 23, p. 233901, 2003.

[27] T. a Nieminen, N. R. Heckenberg, and H. Rubinsztein-Dunlop, "Forces in optical tweezers with radially and azimuthally polarized trapping beams.," *Opt. Lett.*, vol. 33, no. 2, pp. 122–4, 2008.

[28] S. R. Nagel and K. L. Walker, "An overview of the modified chemical vapor deposition (MCVD) process and performances," *IEEE J. Quantum Electron.*, vol. 18, no. 4, pp. 459–476, 1982.

[29] V. V. R. Kumar, A. George, W. Reeves, J. Knight, P. Russell, F. Omenetto, and A. Taylor, "Extruded soft glass photonic crystal fiber for ultrabroad supercontinuum generation," *Opt. Express*, vol. 10, no. 25, pp. 1520–5, 2002.

[30] P. S. J. Russell, "Photonic-crystal fibers," *J. Light. Technol.*, vol. 24, no. 12, pp. 4729–4749, 2006.

[31] B. E. A. Saleh and M. C. Teich, *Fundamentals of photonics*, Wiley 2007.

[32] D. Marcuse, *Theory of dielectric optical waveguides*, Elsevier Sciences & Technology Books 1974.

[33] A. Ghatak and K. Thyagarajan, *Introduction to fiber optics*, Cambridge University Press 1998.

[34] L. F. Stokes, M. Chodorow, and H. J. Shaw, "All-single-mode fiber resonator," *Opt. Lett.*, vol. 7, no. 6, pp. 288–90, 1982.

[35] N. G. R. Broderick, H. L. Offerhaus, D. J. Richardson, R. a. Sammut, J. Caplen, and L. Dong, "Large mode area fibers for high power applications," *Opt. Fiber Technol.*, vol. 5, no. 2, pp. 185–196, 1999.

[36] M.-J. Li, X. Chen, A. Liu, S. Gray, J. Wang, D. T. Walton, and L. A. Zenteno, "Limit of effective area for single-mode operation in step-index large mode area laser fibers," *J. Light. Technol.*, vol. 27, no. 15, pp. 3010–3016, 2009.

[37] W. S. Wong, X. Peng, J. M. McLaughlin, and L. Dong, "Breaking the limit of maximum effective area for robust single-mode propagation in optical fibers," *Opt. Lett.*, vol. 30, no. 21, p. 2855, 2005.

[38] F. Stutzki, F. Jansen, A. Liem, C. Jauregui, J. Limpert, and A. Tünnermann, “26 mJ, 130 W Q-switched fiber-laser system with near-diffraction-limited beam quality.,” *Opt. Lett.*, vol. 37, no. 6, pp. 1073–5, 2012.

[39] L. J. Cooper, P. Wang, R. B. Williams, J. K. Sahu, W. a Clarkson, a M. Scott, and D. Jones, “High-power Yb-doped multicore ribbon fiber laser,” *Opt. Lett.*, vol. 30, no. 21, pp. 2906–8, 2005.

[40] C.-H. Liu, G. Chang, N. Litchinitser, A. Galvanauskas, D. Guertin, N. Jabobson, and K. Tankala, “Effectively single-mode chirally-coupled core fiber,” *Adv. Solid-State Photonics*, no. 1, ME2, 2007.

[41] J. R. Marciante, R. G. Roides, V. V Shkunov, and D. a Rockwell, “Near-diffraction-limited operation of step-index large-mode-area fiber lasers via gain filtering,” *Opt. Lett.*, vol. 35, no. 11, pp. 1828–30, 2010.

[42] L. B. Soldano and E. C. M. Pennings, “Optical multi-mode interference devices based on self-imaging: principles and applications,” *J. Light. Technol.*, vol. 13, no. 4, pp. 615–627, 1995.

[43] A. Mehta, W. Mohammed, and E. G. Johnson, “Multimode interference-based fiber-optic displacement sensor,” *IEEE Photonics Technol. Lett.*, vol. 15, no. 8, pp. 1129–1131, 2003.

[44] P. Wang, M. Ding, L. Bo, C. Guan, Y. Semenova, Q. Wu, G. Farrell, and G. Brambilla, “Fiber-tip high-temperature sensor based on multimode interference,” *Opt. Lett.*, vol. 38, no. 22, pp. 4617–20, 2013.

[45] W. S. Mohammed, A. Mehta, and E. G. Johnson, “Wavelength tunable fiber lens based on multimode interference,” *J. Light. Technol.*, vol. 22, no. 2, pp. 469–477, 2004.

[46] W. S. Mohammed, P. W. E. Smith, and X. Gu, “All-fiber multimode interference bandpass filter,” *Opt. Lett.*, vol. 31, no. 17, pp. 2547–9, 2006.

[47] F. Wang, J. Yang, L. Chen, X. Jiang, and M. Wang, “Optical switch based on multimode interference coupler,” *IEEE Photonics Technol. Lett.*, vol. 18, no. 2, pp. 421–423, 2006.

[48] A. Mafi, P. Hofmann, C. Jollivet, and A. Schülzgen, “Low-loss coupling between two single-mode optical fibers with different mode-field diameters using a graded-index multimode optical fiber,” *Opt. Lett.*, vol. 36, no. 18, pp. 3596–8, 2011.

[49] D. Marcuse, “Loss analysis of single-mode fiber splices,” *Bell Syst. Tech. J.*, vol. 56, no. 5, pp. 703–718, 1977.

[50] D. Flamm, K.-C. Hou, P. Gelszinnis, C. Schulze, S. Schröter, and M. Duparré, "Modal characterization of fiber-to-fiber coupling processes.," *Opt. Lett.*, vol. 38, no. 12, pp. 2128–30, 2013.

[51] D. Marcuse, "Field deformation and loss caused by curvature of optical fibers," *J. Opt. Soc. Am.*, vol. 66, no. 4, pp. 311–320, 1976.

[52] R. T. Schermer, "Mode scalability in bent optical fibers," *Opt. Express*, vol. 15, no. 24, pp. 15674, 2007.

[53] S. J. Garth, "Birefringence in bent single-mode fibers," *J. Light. Technol.*, vol. 6, no. 3, pp. 445–449, 1988.

[54] D. C. Bookbinder, M. Li, and J. Wang, "Bend insensitive optical fibers," US 7,680,381 B1, 2010.

[55] J. M. Fini, "Bend-resistant design of conventional and microstructure fibers with very large mode area," *Opt. Express*, vol. 14, no. 1, pp. 69–81, 2006.

[56] K. S. Lee and T. Erdogan, "Fiber mode conversion with tilted gratings in an optical fiber," *J. Opt. Soc. Am. A*, vol. 18, no. 5, pp. 1176–85, 2001.

[57] S. Suzuki, A. Schülzgen, and N. Peyghambarian, "Single-mode fiber laser based on core-cladding mode conversion," *Opt. Lett.*, vol. 33, no. 4, pp. 351–3, 2008.

[58] S. Ramachandran, Z. Wang, and M. Yan, "Bandwidth control of long-period grating-based mode converters in few-mode fibers," *Opt. Lett.*, vol. 27, no. 9, pp. 698–700, 2002.

[59] X. Zhu, A. Schülzgen, H. Li, H. Wei, J. V Moloney, and N. Peyghambarian, "Coherent beam transformations using multimode waveguides," *Opt. Express*, vol. 18, no. 7, pp. 7506–20, 2010.

[60] S. Ramachandran, P. Kristensen, and M. F. Yan, "Generation and propagation of radially polarized beams in optical fibers," *Opt. Lett.*, vol. 34, no. 16, pp. 2525–7, 2009.

[61] A. L. Bullington, P. H. Pax, A. K. Sridharan, J. E. Heebner, M. J. Messerly, and J. W. Dawson, "Mode conversion in rectangular-core optical fibers.," *Appl. Opt.*, vol. 51, no. 1, pp. 84–8, 2012.

[62] M. SeGall, V. Rotar, J. Lumeau, S. Mokhov, B. Zeldovich, and L. B. Glebov, "Binary volume phase masks in photo-thermo-refractive glass," *Opt. Lett.*, vol. 37, no. 7, pp. 1190–2, 2012.

[63] B. L. Volodin, S. V Dolgy, E. D. Melnik, E. Downs, J. Shaw, and V. S. Ban, "Wavelength stabilization and spectrum narrowing of high-power multimode laser diodes and arrays by use of volume Bragg gratings," *Opt. Lett.*, vol. 29, no. 16, pp. 1891–3, 2004.

[64] O. Andrusyak, V. Smirnov, G. Venus, V. Rotar, and L. Glebov, "Spectral combining and coherent coupling of lasers by volume Bragg gratings," *IEEE J. Sel. Top. Quantum Electron.*, vol. 15, no. 2, pp. 344–353, 2009.

[65] M. SeGall, I. Divliansky, C. Jollivet, A. Schülzgen, and L. Glebov, "Simultaneous laser beam combining and mode conversion using multiplexed volume phase elements," in *Proc. of SPIE*, vol. 8960, p. 89601F, 2014.

[66] V. Arrizón, U. Ruiz, R. Carrada, and L. a González, "Pixelated phase computer holograms for the accurate encoding of scalar complex fields.," *J. Opt. Soc. Am. A*, vol. 24, no. 11, pp. 3500–7, 2007.

[67] M. SeGall, I. Divliansky, C. Jollivet, A. Schülzgen, and L. B. Glebov, "Holographically encoded volume phase masks : A method to extend phase mask capabilities beyond traditional limitations," *Optica*, 2014 (submitted).

[68] A. E. Siegman and E. L. Ginzton, "How to (maybe) measure laser beam quality," in *OSA DPSS*, vol. 17, p. MQ.1, 1998.

[69] S. Wielandy, "Implications of higher-order mode content in large mode area fibers with good beam quality," *Opt. Express*, vol. 15, no. 23, pp. 15402–9, 2007.

[70] D. B. S. Soh, J. Nilsson, S. Baek, C. Codemard, Y. Jeong, and V. Philippov, "Modal power decomposition of beam intensity profiles into linearly polarized modes of multimode optical fibers," *J. Opt. Soc. Am. A*, vol. 21, no. 7, pp. 1241–50, 2004.

[71] F. Gori, M. Santarsiero, R. Borghi, and G. Guattari, "Intensity-based modal analysis of partially coherent beams with Hermite-Gaussian modes.," *Opt. Lett.*, vol. 23, no. 13, pp. 989–91, 1998.

[72] F. Gori, M. Santarsiero, R. Simon, G. Piquero, R. Borghi, and G. Guattari, "Coherent-mode decomposition of partially polarized, partially coherent sources.," *J. Opt. Soc. Am. A.*, vol. 20, no. 1, pp. 78–84, 2003.

[73] O. Shapira, A. Abouraddy, J. Joannopoulos, and Y. Fink, "Complete Modal Decomposition for Optical Waveguides," *Phys. Rev. Lett.*, vol. 94, no. 14, pp. 143902, 2005.

[74] R. W. Gerchberg and W. O. Saxton, "A practical algorithm for the determination of phase from image and diffraction plane pictures," *Optik (Stuttg).*, vol. 35, pp. 227–246, 1972.

[75] W. O. Saxton, *Computer Techniques for Image Processing in Electron Microscopy*, Elsevier Science & Technology books 1978.

[76] N. Andermahr, T. Theeg, and C. Fallnich, "Novel approach for polarization-sensitive measurements of transverse modes in few-mode optical fibers," *Appl. Phys. B*, vol. 91, no. 2, pp. 353–357, 2008.

[77] J. W. Nicholson, a D. Yablon, S. Ramachandran, and S. Ghalmi, "Spatially and spectrally resolved imaging of modal content in large-mode-area fibers," *Opt. Express*, vol. 16, no. 10, pp. 7233–43, 2008.

[78] J. W. Nicholson, A. D. Yablon, J. M. Fini, and M. D. Mermelstein, "Measuring the Modal Content of Large-Mode-Area Fibers," *IEEE J. Sel. Top. Quantum Electron.*, vol. 15, no. 1, pp. 61–70, 2009.

[79] T. Kaiser, D. Flamm, S. Schröter, and M. Duparré, "Complete modal decomposition for optical fibers using CGH-based correlation filters," *Opt. Express*, vol. 17, no. 11, pp. 9347–56, 2009.

[80] M. Duparre, V. Pavelyev, B. Luedge, B. Kley, V. Soifer, and R. Kowarschik, "Generation, superposition and seperation of Gauss-Hermite-modes by means of DOEs," in *Proc. of SPIE*, vol. 3291, pp. 104–114, 1998.

[81] V. A. Soifer and M. A. Golub, *Laser beam mode selection by computer generated holograms*, CRC Press 1994.

[82] Y. Painchaud, M. a Duguay, and F. Ouellette, "Interferometric time measurements of intermodal dispersion in optical fibers by using a CCD photodetector array," *Opt. Lett.*, vol. 17, no. 20, pp. 1423, 1992.

[83] P. Nandi, Z. Chen, A. Witkowska, W. J. Wadsworth, T. A Birks, and J. C. Knight, "Characterization of a photonic crystal fiber mode converter using low coherence interferometry," *Opt. Lett.*, vol. 34, no. 7, pp. 1123–5, 2009.

[84] Y. Z. Ma, Y. Sych, G. Onishchukov, S. Ramachandran, U. Peschel, B. Schmauss, and G. Leuchs, "Fiber-modes and fiber-anisotropy characterization using low-coherence interferometry," *Appl. Phys. B*, vol. 96, no. 2–3, pp. 345–353, 2009.

[85] D. N. Schimpf, R. A. Barankov, and S. Ramachandran, "Cross-correlated (C^2) imaging of fiber and waveguide modes," *Opt. Express*, vol. 19, no. 14, pp. 13008–19, 2011.

[86] F. Stutzki, H.-J. Otto, F. Jansen, C. Gaida, C. Jauregui, J. Limpert, and A. Tünnermann, "High-speed modal decomposition of mode instabilities in high-power fiber lasers," *Opt. Lett.*, vol. 36, no. 23, pp. 4572–4, 2011.

[87] J. Bromage, J. M. Fini, C. Dorrer, and J. D. Zuegel, "Characterization and optimization of Yb-doped photonic-crystal fiber rod amplifiers using spatially resolved spectral interferometry," *Appl. Opt.*, vol. 50, no. 14, pp. 2001–7, 2011.

[88] F. Kong, K. Saitoh, D. Mcclane, T. Hawkins, P. Foy, G. Gu, and L. Dong, "Mode area scaling with all-solid photonic bandgap fibers," *Opt. Express*, vol. 20, no. 24, pp. 26363–72, 2012.

[89] J. M. Fini, J. W. Nicholson, R. S. Windeler, E. M. Monberg, L. Meng, B. Mangan, A. Desantolo, and F. V DiMarcello, "Low-loss hollow-core fibers with improved single-modedness," *Opt. Express*, vol. 21, no. 5, pp. 6233–42, 2013.

[90] X. Ma, C. Zhu, I. Hu, A. Kaplan, and A. Galvanauskas, "Single-mode chirally-coupled-core fibers with larger than 50μm diameter cores," *Opt. Express*, vol. 22, no. 8, pp. 15061–15070, 2014.

[91] J. Kerttula, V. Filippov, V. Ustimchik, Y. Chamorovskiy, and O. G. Okhotnikov, "Mode evolution in long tapered fibers with high tapering ratio," *Opt. Express*, vol. 20, no. 23, pp. 25461–70, 2012.

[92] J. F. Bauters, M. L. Davenport, M. J. R. Heck, J. K. Doylend, A. Chen, A. W. Fang, and J. E. Bowers, "Silicon on ultra-low-loss waveguide photonic integration platform," *Opt. Express*, vol. 21, no. 1, pp. 544–55, 2013.

[93] J. W. Nicholson, L. Meng, J. M. Fini, R. S. Windeler, A. DeSantolo, E. Monberg, F. DiMarcello, Y. Dulashko, M. Hassan, and R. Ortiz, "Measuring higher-order modes in a low-loss, hollow-core, photonic-bandgap fiber," *Opt. Express*, vol. 20, no. 18, pp. 20494–505, 2012.

[94] J. W. Nicholson, J. M. Fini, a M. DeSantolo, X. Liu, K. Feder, P. S. Westbrook, V. R. Supradeepa, E. Monberg, F. DiMarcello, R. Ortiz, C. Headley, and D. J. DiGiovanni, "Scaling the effective area of higher-order-mode erbium-doped fiber amplifiers," *Opt. Express*, vol. 20, no. 22, pp. 24575–84, 2012.

[95] P. Kadwani, C. Jollivet, R. A. Sims, A. Schülzgen, L. Shah, and M. Richardson, "Comparison of higher-order mode suppression and Q-switched laser performance in thulium-doped large mode area and photonic crystal fibers," *Opt. Express*, vol. 20, no. 22, p. 24295, 2012.

[96] G. Gu, F. Kong, T. W. Hawkins, P. Foy, K. Wei, B. Samson, and L. Dong, "Impact of fiber outer boundaries on leaky mode losses in leakage channel fibers," *Opt. Express*, vol. 21, no. 20, pp. 13218–13224, 2013.

[97] J. Jasapara and a D. Yablon, "Spectrogram approach to S^2 fiber mode analysis to distinguish between dispersion and distributed scattering," *Opt. Lett.*, vol. 37, no. 18, pp. 3906–8, 2012.

[98] W. H. Lee, "Sampled fourier transform hologram generated by computer," *Appl. Opt.*, vol. 9, no. 3, pp. 639–43, Mar. 1970.

[99] D. Flamm, O. a Schmidt, C. Schulze, J. Borchardt, T. Kaiser, S. Schröter, and M. Duparré, "Measuring the spatial polarization distribution of multimode beams emerging from passive step-index large-mode-area fibers," *Opt. Lett.*, vol. 35, no. 20, pp. 3429–31, 2010.

[100] C. Schulze, O. Schmidt, D. Flamm, M. Duparré, and S. Schröter, "Modal analysis of beams emerging from a multi-core fiber using computer-generated holograms," in *SPIE vol. 7914*, vol. 7914, no. 0, p. 79142H–79142H–9, 2011.

[101] D. Flamm, D. Naidoo, C. Schulze, A. Forbes, and M. Duparré, "Mode analysis with a spatial light modulator as a correlation filter," *Opt. Lett.*, vol. 37, no. 13, pp. 2478–80, 2012.

[102] C. Schulze, A. Lorenz, D. Flamm, A. Hartung, S. Schroter, H. Bartelt, and D. Michael, "Mode resolved bend loss in few-mode optical fibers," *Opt. Express*, vol. 21, no. 3, pp. 75–83, 2013.

[103] A. Dudley, I. Litvin, and A. Forbes, "Quantitative measurement of the orbital angular momentum density of light," *Appl. Opt.*, vol. 51, no. 7, pp. 823–33, 2012.

[104] D. Flamm, C. Schulze, R. Brüning, O. a Schmidt, T. Kaiser, S. Schröter, and M. Duparré, "Fast M^2 measurement for fiber beams based on modal analysis," *Appl. Opt.*, vol. 51, no. 7, pp. 987–93, 2012.

[105] C. Schulze, D. Naidoo, D. Flamm, O. a Schmidt, A. Forbes, and M. Duparré, "Wavefront reconstruction by modal decomposition," *Opt. Express*, vol. 20, no. 18, pp. 19714–25, 2012.

[106] S. Shwartz, M. Golub, and S. Ruschin, "Diffractive optical elements for mode-division multiplexing of temporal signals with the aid of Laguerre-Gaussian modes," *Appl. Opt.*, vol. 52, no. 12, pp. 2659–69, 2013.

[107] D. Flamm, C. Schulze, D. Naidoo, S. Schröter, A. Forbes, and M. Duparré, "All-digital holographic tool for mode excitation and analysis in optical fibers," *J. Light. Technol.*, vol. 31, no. 7, pp. 1023–1032, 2013.

[108] C. Jollivet, D. Flamm, M. Duparre, and A. Schulzgen, "Detailed characterization of optical fibers by combining S^2 imaging with correlation filter mode analysis," *IEEE J. Light. Technol.*, vol. 32, no. 6, pp. 1068–1074, 2014.

[109] C. Jollivet, D. Flamm, M. Duparré, and A. Schülzgen, "New experimental tool for enhanced fiber mode analysis," in *Frintiers in Optics*, vol. 2, no. c, p. FW1B, 2013.

[110] A. D. Yablon, “Multi-wavelength optical fiber refractive index profiling by spatially resolved Fourier transform spectroscopy,” *J. Light. Technol.*, vol. 28, no. 4, pp. 360–364, 2010.

[111] B. W. Morrissey and C. J. Powell, “Interpolation of refractive index data,” *Appl. Opt.*, vol. 12, no. 7, pp. 1588–1591, 1973.

[112] D. M. Nguyen, S. Blin, T. N. Nguyen, S. D. Le, L. Provino, M. Thual, and T. Chartier, “Modal decomposition technique for multimode fibers,” *Appl. Opt.*, vol. 51, no. 4, pp. 450–6, 2012.

[113] H. Otto, F. Jansen, F. Stutzki, C. Jauregui, J. Limpert, and A. Tünnermann, “Improved Modal Reconstruction for Spatially and Spectrally Resolved Imaging,” *J. Light. Technol.*, vol. 31, no. 8, pp. 1295–1299, 2013.

[114] L. Dong, H. A. Mckay, A. Marcinkevicius, L. Fu, J. Li, B. K. Thomas, and M. E. Fermann, “Extending effective area of fundamental mode in optical fibers,” *J. Light. Technol.*, vol. 27, no. 11, pp. 1565–1570, 2009.

[115] K. Saitoh, S. Varshney, K. Sasaki, L. Rosa, M. Pal, M. C. Paul, D. Ghosh, S. K. Bhadra, and M. Koshiba, “Limitation on effective area of bent large-mode-area leakage channel fibers,” *J. Light. Technol.*, vol. 29, no. 17, pp. 2609–2615, 2011.

[116] R. A. Barankov, K. Wei, B. Samson, and S. Ramachandran, “Resonant bend loss in leakage channel fibers,” *Opt. Lett.*, vol. 37, no. 15, pp. 3147–9, 2012.

[117] L. Dong, H. A. McKay, L. Fu, M. Ohta, A. Marcinkevicius, S. Suzuki, and M. E. Fermann, “Ytterbium-doped all glass leakage channel fibers with highly fluorine-doped silica pump cladding,” *Opt. Express*, vol. 17, no. 11, p. 8962, 2009.

[118] O. Schmidt, J. Rothhardt, F. Röser, S. Linke, T. Schreiber, K. Rademaker, J. Limpert, S. Ermeneux, P. Yvernault, F. Salin, and A. Tünnermann, “Millijoule pulse energy Q-switched short-length fiber laser,” *Opt. Lett.*, vol. 32, no. 11, pp. 1551–3, 2007.

[119] F. Stutzki, F. Jansen, C. Jauregui, J. Limpert, and A. Tünnermann, “Non-hexagonal large-pitch fibers for enhanced mode discrimination.,” *Opt. Express*, vol. 19, no. 13, pp. 12081–6, 2011.

[120] F. Jansen, F. Stutzki, C. Jauregui, J. Limpert, and A. Tünnermann, “High-power very large mode-area thulium-doped fiber laser,” *Opt. Lett.*, vol. 37, no. 21, pp. 4546–8, 2012.

[121] H.-J. Otto, F. Stutzki, F. Jansen, T. Eidam, C. Jauregui, J. Limpert, and A. Tünnermann, “Temporal dynamics of mode instabilities in high-power fiber lasers and amplifiers,” *Opt. Express*, vol. 20, no. 14, pp. 15710–22, 2012.

[122] B. Ward, C. Robin, and I. Dajani, "Origin of thermal modal instabilities in large mode area fiber amplifiers," *Opt. Express*, vol. 20, no. 10, pp. 11407–22, 2012.

[123] C. Jauregui, T. Eidam, H.-J. Otto, F. Stutzki, F. Jansen, J. Limpert, and A. Tünnermann, "Temperature-induced index gratings and their impact on mode instabilities in high-power fiber laser systems," *Opt. Express*, vol. 20, no. 1, pp. 440–51, 2012.

[124] C. Jauregui, H. Otto, F. Stutzki, F. Jansen, J. Limpert, and A. Tünnermann, "Passive mitigation strategies for mode instabilities in high-power fiber laser systems," *Opt. Express*, vol. 21, no. 16, pp. 19375–19386, 2013.

[125] H. Otto, A. Klenke, C. Jauregui, F. Stutzki, J. Limpert, and A. Tünnermann, "Scaling the mode instability threshold with multicore fibers," vol. 39, no. 9, pp. 2680–2683, 2014.

[126] M. Laurila, M. M. Jørgensen, K. R. Hansen, T. T. Alkeskjold, J. Broeng, and J. Lægsgaard, "Distributed mode filtering rod fiber amplifier delivering 292W with improved mode stability," *Opt. Express*, vol. 20, no. 5, pp. 5742–53, 2012.

[127] S. Saitoh, K. Saitoh, M. Kashiwagi, S. Matsuo, and L. Dong, "Design optimization of large-mode-area all-solid photonic bandgap fibers for high-power laser applications," *J. Light. Technol.*, vol. 32, no. 3, pp. 440–449, 2014.

[128] P. Sprangle, A. Ting, J. Peñano, R. Fischer, and B. Hafizi, "Incoherent combining and atmospheric propagation of high-power fiber lasers for directed-energy applications," *IEEE J. Quantum Electron.*, vol. 45, no. 2, pp. 138–148, 2009.

[129] G. J. Koch, J. Y. Beyon, B. W. Barnes, M. Petros, Y. J., F. Amzajerdian, M. J. Kavaya, and U. N. Singh, "High-energy 2 μm Doppler lidar for wind measurements," *Opt. Eng.*, vol. 46, no. 11, p. 116201, 2007.

[130] J.-P. Cariou, B. Augere, and M. Valla, "Laser source requirements for coherent lidars based on fiber technology," *Comptes Rendus Phys.*, vol. 7, no. 2, pp. 213–223, 2006.

[131] N. M. Fried, R. L. Blackmon, and P. B. Irby, "A review of Thulium fiber laser ablation of kidney stones," in *proc. of SPIE*, vol. 791402–791402–10, 2011.

[132] D. Creeden, P. a Ketteridge, P. a Budni, S. D. Setzler, Y. E. Young, J. C. McCarthy, K. Zawilski, P. G. Schunemann, T. M. Pollak, E. P. Chicklis, and M. Jiang, "Mid-infrared ZnGeP2 parametric oscillator directly pumped by a pulsed 2 μm Tm-doped fiber laser," *Opt. Lett.*, vol. 33, no. 4, pp. 315–7, 2008.

[133] P. F. Moulton, G. A. Rines, E. V Slobodtchikov, K. F. Wall, G. Frith, B. Samson, and A. L. G. Carter, "Tm-doped fiber lasers : fundamentals and power scaling," *IEEE J. Sel. Top. Quantum Electron.*, vol. 15, no. 1, pp. 85–92, 2009.

[134] T. S. McComb, R. A. Sims, C. C. C. Willis, P. Kadwani, V. Sudesh, L. Shah, and M. Richardson, "High-power widely tunable thulium fiber lasers," *Appl. Opt.*, vol. 49, no. 32, pp. 6236–42, 2010.

[135] N. Modsching, P. Kadwani, R. A. Sims, L. Leick, J. Broeng, L. Shah, and M. Richardson, "Lasing in thulium-doped polarizing photonic crystal fiber," *Opt. Lett.*, vol. 36, no. 19, pp. 3873–5, 2011.

[136] C. Gaida, P. Kadwani, L. Leick, J. Broeng, L. Shah, and M. Richardson, "CW-lasing and amplification in Tm(3+)-doped photonic crystal fiber rod," *Opt. Lett.*, vol. 37, no. 21, pp. 4513–5, 2012.

[137] C. Jollivet, C. Loussert, T. T. Alkeskjold, L. Leick, R. A. Sims, P. Kadwani, L. Shah, M. C. Richardson, R. A. Correa, and A. Schülzgen, "Modal analysis of large-mode-area photonic crystal fiber for high power 2 μm fiber lasers," in *Lasers, sources and related photonics devices, FILAS*, pp. 17–19, 2012.

[138] C. Jollivet, T. T. Alkeskjold, L. Leick, P. Kadwani, R. a. Sims, L. Shah, M. C. Richardson, R. Amezcua Correa, and A. Schülzgen, "Modal properties of photonic crystal fiber for high-power 2 μm fiber laser systems," in *Proc. of SPIE*, vol. 8381, p. 838105, 2012.

[139] C. Jollivet, B. Samson, L. Leick, L. Shah, M. Richardson, and A. Schülzgen, "Comparative study of light propagation and single-mode operation in large-mode area fibers designed for 2μm laser applications," *Opt. Eng.*, 2014 (submitted).

[140] E. Coscelli, C. Molardi, M. Masruri, A. Cucinotta, and S. Selleri, "Thermally resilient Tm-doped large mode area photonic crystal fiber with symmetry-free cladding," *Opt. Express*, vol. 22, no. 8, p. 9707, 2014.

[141] S. K. Sheem, "Optical fiber interferometers with [3×3] directional couplers: Analysis," *J. Appl. Phys.*, vol. 52, no. 6, p. 3865, 1981.

[142] T. Bricheno and V. Baker, "All-fibre polarization splitter/combiner," *Electron. Lett.*, vol. 21, no. 6, pp. 251–252, 1985.

[143] E. H. Turner and R. H. Stolen, "Fiber Faraday circulator or isolator," *Opt. Lett.*, vol. 6, no. 7, pp. 322–3, 1981.

[144] D. J. DiGiovanni and A. J. Stentz, "Tapered fiber bundles for coupling light into and out of cladding-pumped fiber devices," US 5,864,644 A, 1999.

[145] K. O. Hill and G. Meltz, "Fiber Bragg grating technology fundamentals and overview," *J. Light. Technol.*, vol. 15, no. 8, pp. 1263–1276, 1997.

[146] J. Canning, N. Groothoff, K. Cook, C. Martelli, A. Pohl, J. Holdsworth, S. Bandyopadhyay, and M. Stevenson, "Gratings in structured optical fibres," *Laser Chem.*, vol. 2008, pp. 1–19, 2008.

[147] K. Stepien, M. Slowikowski, T. Tenderenda, M. Murawski, M. Szymanski, L. Szostkiewicz, M. Becker, M. Rothhardt, H. Bartelt, P. Mergo, L. R. Jaroszewics, and T. Nasilowski, "Fiber Bragg gratings in hole-assisted multicore fiber for space division multiplexing," *Opt. Lett.*, vol. 39, no. 12, pp. 3571–3574, 2014.

[148] B. H. Lee, J. B. Eom, J. Kim, D. S. Moon, U.-C. Paek, and G.-H. Yang, "Photonic crystal fiber coupler," *Opt. Lett.*, vol. 27, no. 10, pp. 812–4, 2002.

[149] K. Lai, S. G. Leon-Saval, A. Witkowska, W. J. Wadsworth, and T. A. Birks, "Wavelength-independent all-fiber mode converters," *Opt. Lett.*, vol. 32, no. 4, pp. 328–30, 2007.

[150] C. Jauregui, J. Limpert, and A. Tünnermann, "High-power fibre lasers," *Nat. Photonics*, vol. 7, no. 11, pp. 861–867, 2013.

[151] D. J. Richardson, J. Nilsson, and W. a. Clarkson, "High power fiber lasers: current status and future perspectives," *J. Opt. Soc. Am. B*, vol. 27, no. 11, p. B63, 2010.

[152] Y. Jeong, J. Sahu, D. Payne, and J. Nilsson, "Ytterbium-doped large-core fiber laser with 1.36 kW continuous-wave output power," *Opt. Express*, vol. 12, no. 25, pp. 6088–92, 2004.

[153] T. Eidam, S. Hanf, E. Seise, T. V Andersen, T. Gabler, C. Wirth, T. Schreiber, J. Limpert, and A. Tünnermann, "Femtosecond fiber CPA system emitting 830 W average output power," *Opt. Lett.*, vol. 35, no. 2, pp. 94–6, 2010.

[154] P. Yan, S. Yin, J. He, C. Fu, Y. Wang, and M. Gong, "1.1-kW Ytterbium monolithic fiber laser with assembled end-pump scheme to couple high brightness single emitters," *IEEE Photonics Technol. Lett.*, vol. 23, no. 11, pp. 697–699, 2011.

[155] C. Liu, A. Galvanauskas, V. Khitrov, B. Samson, U. Manyam, K. Tankala, D. Machewirth, and S. Heinemann, "High-power single-polarization and single-transverse-mode fiber laser with an all-fiber cavity and fiber-grating stabilized spectrum," *Opt. Lett.*, vol. 31, no. 1, pp. 17–19, 2006.

[156] A. K. Sridharan, P. Pax, M. J. Messerly, and J. W. Dawson, "High-gain photonic crystal fiber regenerative amplifier," *Opt. Lett.*, vol. 34, no. 5, pp. 608–10, 2009.

[157] O. Schmidt, C. Wirth, I. Tsybin, T. Schreiber, R. Eberhardt, J. Limpert, and A. Tünnermann, "Average power of 1 .1 kW from spectrally combined, fiber-amplified, nanosecond-pulsed sources," *Opt. Lett.*, vol. 34, no. 10, pp. 1567–1569, 2009.

[158] S. Klingebiel, F. Röser, B. Ortaç, J. Limpert, and A. Tünnermann, "Spectral beam combining of Yb-doped fiber lasers with high efficiency," *J. Opt. Soc. Am. B*, vol. 24, no. 8, pp. 1716, 2007.

[159] P. J. Bennett, T. M. Monro, and D. J. Richardson, "Toward practical holey fiber technology: fabrication, splicing, modeling, and characterization," *Opt. Lett.*, vol. 24, no. 17, pp. 1203–5, 1999.

[160] B. Bourliaguet, C. Paré, F. Emond, A. Croteau, A. Proulx, and R. Vallée, "Microstructured fiber splicing," *Opt. Express*, vol. 11, no. 25, pp. 3412–7, 2003.

[161] L. Xiao, M. S. Demokan, W. Jin, Y. Wang, and C. Zhao, "Fusion splicing photonic crystal fibers and conventional single-mode fibers : microhole collapse ffect," *J. Light. Technol.*, vol. 25, no. 11, pp. 3563–3574, 2007.

[162] L. R. Jaroszewicz, M. Murawski, T. Nasilowski, K. Stasiewicz, P. Marc, M. Szymanski, P. Mergo, W. Urbanczyk, F. Berghmans, and H. Thienpont, "Low-loss patch cords by effective splicing of various photonic crystal fibers with standard single mode fiber," *J. Light. Technol.*, vol. 29, no. 19, pp. 2940–2946, 2011.

[163] J. H. Chong, M. K. Rao, Y. Zhu, and P. Shum, "An effective splicing method on photonic crystal fiber using CO_2 laser," *IEEE Photonics Technol. Lett.*, vol. 15, no. 7, pp. 942–944, 2003.

[164] J. Liu, T.-H. Cheng, Y.-K. Yeo, Y. Wang, L. Xue, Z. Xu, and D. Wang, "Light beam coupling between standard single mode fibers and highly nonlinear photonic crystal fibers based on the fused biconical tapering technique," *Opt. Express*, vol. 17, no. 5, pp. 3115–23, 2009.

[165] Z. Chen, X. Xi, W. Zhang, J. Hou, and Z. Jiang, "Low-loss fusion splicing photonic crystal fibers and double cladding fibers by controlled hole collapse and tapering," *J. Light. Technol.*, vol. 29, no. 24, pp. 3744–3747, 2011.

[166] T. Zhu, F. Xiao, L. Xu, M. Liu, M. Deng, and K. S. Chiang, "Pressure-assisted low-loss fusion splicing between photonic crystal fiber and single-mode fiber," *Opt. Express*, vol. 20, no. 22, pp. 24465–71, 2012.

[167] A. D. Yablon and R. T. Bise, "Low-loss high-strength microstructured fiber fusion splices using GRIN fiber lenses," *IEEE Photonics Technol. Lett.*, vol. 17, no. 1, pp. 118–120, 2005.

[168] B. G. Ward, D. L. Sipes, Jr., and J. D. Tafoya, "A monolithic pump signal multiplexer for air-clad photonic crystal fiber amplifiers," in *SPIE*, vol. 7580, p. 75801C–8, 2010.

[169] P. Hofmann, A. Mafi, C. Jollivet, T. Tiess, N. Peyghambarian, and A. Schülzgen, "Detailed investigation of mode-field adapters utilizing multimode-interference in graded index fibers," *J. Light. Technol.*, vol. 30, no. 14, pp. 2289–2298, 2012.

[170] C. Jollivet, J. Guer, P. Hofmann, and A. Schulzgen, "Monolithic fiber lasers combining active PCF with Bragg gratings in conventional single-mode fibers," *IEEE J. Sel. Top. Quantum Electron.*, vol. 20, no. 5, 2014.

[171] C. Jollivet, J. Guer, P. Hofmann, A. Mafi, and A. Schülzgen, "All-fiber mode-field adapter for low coupling loss between step-index and large-mode area fibers," in *Advanced solid-state lasers congress technical digest OSA*, JTh2A.02, 2013.

[172] C. Jollivet, J. Guer, P. Hofmann, and A. Schülzgen, "Monolithic integration of active LMA PCF and standard fiber Bragg gratings into all-fiber lasers," in *Advanced Photonics Congress OSA*, JM5A.11, 2014.

[173] A. F. Gmitro and D. Aziz, "Confocal microscopy through a fiber-optic imaging bundle," *Opt. Lett.*, vol. 18, no. 8, pp. 565–567, 1993.

[174] A. F. Rouse and A. F. Gmitro, "Multispectral imaging with a confocal microendoscope," *Opt. Lett.*, vol. 25, no. 23, pp. 1708–10, 2000.

[175] S. Zheng, G. Ren, Z. Lin, and S. Jian, "Mode-coupling analysis and trench design for multicore fiber," *Appl. Opt.*, vol. 52, no. 19, pp. 4541–4548, 2013.

[176] H. Takahashi, T. Tsuritani, E. L. T. de Gabory, T. Ito, W. R. Peng, K. Igarashi, K. Takeshima, Y. Kawaguchi, I. Morita, Y. Tsuchida, Y. Mimura, K. Maeda, T. Saito, K. Watanabe, K. Imamura, R. Sugizaki, and M. Suzuki, "First demonstration of MC-EDFA-repeatered SDM transmission of 40 x 128-Gbit/s PDM-QPSK signals per core over 6,160-km 7-core MCF," *Opt. Express*, vol. 21, no. 1, pp. 789–95, 2013.

[177] D. J. Richardson, J. M. Fini, and L. E. Nelson, "Space-division multiplexing in optical fibres," *Nat. Photonics*, vol. 7, no. April, pp. 354–362, 2013.

[178] K. S. Abedin, T. F. Taunay, M. Fishteyn, D. J. Digiovanni, V. R. Supradeepa, J. M. Fini, M. F. Yan, B. Zhu, E. M. Monberg, and F. V Dimarcello, "Cladding-pumped erbium-doped multicore fiber amplifier," *Opt. Express*, vol. 20, no. 18, pp. 20191–20200, 2012.

[179] N. Bai, E. Ip, Y.-K. Huang, E. Mateo, F. Yaman, M.-J. Li, S. Bickham, S. Ten, J. Liñares, C. Montero, V. Moreno, X. Prieto, V. Tse, K. Man Chung, A. P. T. Lau, H.-Y. Tam, C. Lu, Y. Luo, G.-D. Peng, G. Li, and T. Wang, "Mode-division multiplexed transmission with inline few-mode fiber amplifier," *Opt. Express*, vol. 20, no. 3, pp. 2668–80, 2012.

[180] A. Castillo-Guzman, J. E. Antonio-Lopez, R. Selvas-Aguilar, D. a May-Arrioja, J. Estudillo-Ayala, and P. LiKamWa, "Widely tunable erbium-doped fiber laser based on multimode interference effect," *Opt. Express*, vol. 18, no. 2, pp. 591–7, 2010.

[181] X. Zhu, A. Sch, H. Li, L. Li, V. L. Temyanko, J. V Moloney, and N. Peyghambarian, "High-Power Fiber Lasers and Amplifiers Based on Multimode Interference," *IEEE J. Sel. Top. Quantum Electron.*, vol. 15, no. 1, pp. 71–78, 2009.

[182] C. Xia, N. Bai, I. Ozdur, X. Zhou, and G. Li, "Supermodes for optical transmission," *Opt. Express*, vol. 19, no. 17, pp. 16653–64, 2011.

[183] A. Van Newkirk, E. Antonio-lopez, G. Salceda-delgado, R. Amezcua-correa, and A. Schülzgen, "Optimization of multicore fiber for high temperature sensing," *Opt. Lett.*, 2014.

[184] C. Guan and L. Y. J. Shi, "Supermode analysis of multicore photonic crystal fibers," *Opt. Commun.*, vol. 283, no. 13, pp. 2686–2689, 2010.

[185] E. J. Bochove, P. K. Cheo, and G. G. King, "Self-organization in a multicore fiber laser array," *Opt. Lett.*, vol. 28, no. 14, pp. 1200–2, 2003.

[186] P. K. Cheo, A. Liu, and G. G. King, "A high-brightness laser beam from a phase-locked multicore Yb-doped fiber laser array," *IEEE Photonics Technol. Lett.*, vol. 13, no. 5, pp. 439–441, 2001.

[187] L. Li, a. Schülzgen, H. Li, V. L. Temyanko, J. V. Moloney, and N. Peyghambarian, "Phase-locked multicore all-fiber lasers: modeling and experimental investigation," *J. Opt. Soc. Am. B*, vol. 24, no. 8, pp. 1721, 2007.

[188] L. Michaille, C. R. Bennett, D. M. Taylor, T. J. Shepherd, J. Broeng, H. R. Simonsen, and A. Petersson, "Phase locking and supermode selection in multicore photonic crystal fiber lasers with a large doped area," *Opt. Lett.*, vol. 30, no. 13, pp. 1668–70, 2005.

[189] M. Wrage, P. Glas, D. Fischer, M. Leitner, D. V Vysotsky, and a P. Napartovich, "Phase locking in a multicore fiber laser by means of a Talbot resonator.," *Opt. Lett.*, vol. 25, no. 19, pp. 1436–8, 2000.

[190] M. Wrage, P. Glas, and M. Leitner, "Combined phase locking and beam shaping of a multicore fiber laser by structured mirrors.," *Opt. Lett.*, vol. 26, no. 13, pp. 980–2, 2001.

[191] M. Wrage, P. Glas, D. Fischer, M. Leitner, N. N. Elkin, D. V. Vysotsky, a. P. Napartovich, and V. N. Troshchieva, "Phase-locking of a multicore fiber laser by wave propagation through an annular waveguide," *Opt. Commun.*, vol. 205, no. 4–6, pp. 367–375, 2002.

[192] L. Li, A. Schülzgen, S. Chen, V. L. Temyanko, J. V Moloney, and N. Peyghambarian, "Phase locking and in-phase supermode selection in monolithic multicore fiber lasers," *Opt. Lett.*, vol. 31, no. 17, pp. 2577–9, 2006.

[193] C. J. Corcoran and F. Durville, "Experimental demonstration of a phase-locked laser array using a self-Fourier cavity," *Appl. Phys. Lett.*, vol. 86, no. 20, p. 201118, 2005.

[194] X. Zhu, a Schülzgen, H. Li, L. Li, Q. Wang, S. Suzuki, V. L. Temyanko, J. V Moloney, and N. Peyghambarian, "Single-transverse-mode output from a fiber laser based on multimode interference.," *Opt. Lett.*, vol. 33, no. 9, pp. 908–10, 2008.

[195] M. Paurisse, M. Hanna, F. Druon, P. Georges, C. Bellanger, A. Brignon, and J. P. Huignard, "Phase and amplitude control of a multimode LMA fiber beam by use of digital holography," *Opt. Express*, vol. 17, no. 15, pp. 13000–8, 2009.

[196] Y. Huo and P. K. Cheo, "Analysis of transverse mode competition and selection in multicore fiber lasers," *J. Opt. Soc. Am. B*, vol. 22, no. 11, p. 2345, 2005.

[197] A S. Kurkov, S. A. Babin, I. A. Lobach, and S. I. Kablukov, "Mechanism of mode coupling in multicore fiber lasers," *Opt. Lett.*, vol. 33, no. 1, pp. 61–3, 2008.

[198] J. K. Butler, D. E. Ackley, and D. Botez, "Coupled-mode analysis of phase-locked injection laser arrays," *Appl. Phys. Lett.*, vol. 44, no. 3, pp. 293, 1984.

[199] E. Kapon, J. Katz, and A. Yariv, "Supermode analysis of phase-locked arrays of semiconductor lasers," *Opt. Lett.*, vol. 10, no. 4, pp. 125–127, 1984.

[200] A. Benoit, R. Dauliat, K. Schuster, S. Grimm, R. Jamier, F. Salin, and P. Roy, "Optical fiber microstructuration for strengthening single-mode laser operation in high power regime," *Opt. Eng.*, vol. 53, no. 7, pp. 071817, 2014.

[201] A. W. Snyder, "Coupled-mode theory for optical fibers," *J. Opt. Soc. Am.*, vol. 62, no. 11, pp. 1267, 1972.

[202] M. Laurila, T. T. Alkeskjold, J. Laegsgaard, and J. Broeng, "Modal analysis of a large-mode area photonic crystal fiber amplifier using spectral-resolved imaging," *Opt. Eng.*, vol. 50, no. 11, pp. 111604, 2011.

[203] J. Limpert, N. Deguil-Robin, I. Manek-Hönninger, F. Salin, F. Röser, A. Liem, T. Schreiber, S. Nolte, H. Zellmer, A. Tünnermann, J. Broeng, A. Petersson, and C. Jakobsen, "High-power rod-type photonic crystal fiber laser," *Opt. Express*, vol. 13, no. 4, pp. 1055–8, 2005.

[204] F. Stutzki, C. Jauregui, C. Voigtländer, J. Thomas, S. Nolte, J. Limpert, and A. Tünnermann, "Real-time monitoring of the modal content of monolithic large-mode-area fiber lasers," in *OSA/OFC/NFOEC*, pp. 10–12, 2010.

[205] M. E. Fermann and I. Hartl, “Ultrafast fibre lasers,” *Nat. Photonics*, pp. 1–7, 2013.

[206] G. P. Agrawal, *Nonlinear fiber optics (4th edition*), Elsevier 2007.

[207] P. Myslinski, J. Chrostowski, J. a Koningstein, and J. R. Simpson, “Self-mode locking in a Q-switched erbium-doped fiber laser,” *Appl. Opt.*, vol. 32, no. 3, pp. 286–90, 1993.

[208] X. Feng, B. Chen, J. Chen, L. Wang, L. Liang, and Z. Lin, “Study of self mode-locking in Q-Switched and in all-fiber fabry-perot cavity Ytterbium-doped fiber laser,” in *Proc. of SPIE*, vol. 5623, pp. 88–95, 2005.

[209] Z. Q. Luo, C. C. Ye, H. Y. Fu, H. H. Cheng, J. Z. Wang, and Z. P. Cai, “Raman fiber laser harmonically mode-locked by exploiting the intermodal beating of CW multimode pump source,” *Opt. Express*, vol. 20, no. 18, pp. 19905–11, 2012.

[210] C. Liu, Z. Luo, Y. Huang, B. Qu, H. Cheng, Y. Wang, D. Wu, H. Xu, and Z. Cai, “Self-mode-locked 2 μm Tm-doped double-clad fiber laser with a simple linear cavity,” *Appl. Opt.*, vol. 53, no. 5, pp. 892–897, 2014.

[211] E. Nazemosadat and A. Mafi, “Nonlinear multimodal interference and saturable absorption using a short graded-index multimode optical fiber,” *J. Opt. Soc. Am. B*, vol. 30, no. 5, pp. 1357–1367, 2013.

[212] E. Nazemosadat and A. Mafi, “Nonlinear switching in multicore versus multimode waveguide junctions for mode-locked laser applications,” *Opt. Express*, vol. 21, no. 25, pp. 30739–30745, 2013.

[213] C. Jollivet, D. Flamm, M. Duparré, K. Schuster, S. Grimm, and A. Schülzgen, “Supermode decomposition during operation of a 7-core fiber laser,” in *Advanced Photonics Congress OSA*, JM5A.12, 2014.